SCUOLA DI DOTTORATO
UNIVERSITÀ DEGLI STUDI DI MILANO-BICOCCA

Department of Earth and Environmental Sciences

Ph.D. program: **Chemical, Geological and Environmental Sciences**
Cycle: **XXXIV**

Curriculum in: **Geological Sciences**

Alpine rock glaciers: surface dynamics and role in stream hydrology

Surname: **Bearzot** Name: **Francesca**

Registration number: **848251**

Tutor: **Prof. Paolo Frattini**

Supervisor: **Prof.ssa Micol Rossini**

Coordinator: **Prof. Marco Giovanni Malusà**

ACADEMIC YEAR: 2020/2021

CONTENTS

LIST OF FIGURES

LIST OF TABLES

ABBREVIATIONS

ARPA VdA	Environmental Protection Agency of Valle d'Aosta
a.s.l.	above sea level
BCF	Bulk Creep Factor
BH	Borehole
BST	Bottom Temperature of Snow cover
CPs	Check Points
DoD	Difference of Digital Surface Model
DSM	Digital Surface Model
EC	Electrical Conductivity
ECDF	Empirical Cumulative Distribution Function
ECV	Essential Climate Variables
ERT	Electrical Resistivity Tomography
GCOS	Global Climate Observing System
GCPs	Ground Control Points
GIS	Geographical Information System
GNSS	Global Navigation Satellite Systems
GFI	Ground Freezing Index
GRS-LW	Geophysical survey on the white lobe
GRS-LB	Geophysical survey on the black lobe
GST	Ground Surface Temperature
GTI	Ground Thawing Index
IF	Injection point of Fluorescein
IPA	International Permafrost Association
IT	Injection point of Tynopal
LIA	Little Ice Age
LOD	Level of Detection
M3C2	Multiscale Model-to-Model Cloud Comparison
MAAT	Mean Annual Air Temperature
MAGST	Mean Annual Ground Surface Temperature
Nz	Vertical component of the local surface changes
PERMOS	Swiss Permafrost Monitoring Network
ppb	parts per billion
Reg	Registration error
RGs	Rock Glacier (White and Black lobes)
RMSE	Root Mean Square Error
SfM-MVS	Structure from Motion multi-view stereophotogrammetry
SWE	Snow Water Equivalent
T_{air}	Air temperature
UAV	Unmanned Aerial Vehicle
WEqT	Winter Equilibrium Temperature

ABSTRACT

Since the 1990s, a significant acceleration of rock glacier flow rates and of destabilizing phenomena have been documented in the European Alps in relation to constantly rising temperatures, soil warming and ice loss. Changing climatic conditions and in particular the increase in air temperature strongly influence the thermal state of permafrost. Recent studies showed that ground surface temperature (GST), together with the rock glacier external (i.e. topographical conditions) and internal (i.e. internal structure and composition) characteristics, controls the deformation of perennially frozen ground and the associated rock glacier flow velocities.

Studies of time series of kinematic data showed a correlation between rock glacier flow rates and air temperatures at seasonal, inter-annual and decadal time scales, while short-term velocity variations seem to be influenced more by the hydrology of the rock glaciers. Rock glaciers contain hydrologically valuable ice volumes, which, under future climate warming, could affect the hydrology of the territory, increasing the flow of rivers and streams in high mountain areas. These observations raise several questions about the fundamental mechanisms that control the dynamics of rock glaciers and their coupling with the ongoing climate warming.

The thesis, composed by three main studies, examines the influence of air and ground temperatures forcing and the processes controlling the evolution of rock glacier dynamics at multi spatio-temporal scales by means of process-based modelling, data collection and analysis, and remote sensing techniques. For this purpose, high spatial resolution RGB data collected with drone platforms and direct in-situ measurements, related to thermal state of permafrost and hydrology, were conducted.

The first study is aimed at investigating the spatial and temporal flow patterns of perennially frozen ground in the Gran Sometta rock glacier on interannual and

multiannual time scales through repeated drone surveys (2016-2019), Global Navigation Satellite System (GNSS) campaigns (2012-2020), two geophysical prospections in 2015 and data on ground surface temperature (2014-2020). First, the focus was set on assessing the accuracy of the Digital Surface Models (DSMs) and on evaluating systematic errors (dome and bowl deformations) that may affect the drone-SfM derived data. Since the analysis on the drone-SfM products gave high accurate results (dome/bowl size between -2.77 cm and 4.12 cm), the dense point clouds, the orthoimages and the DSMs were then processed to derive 2D and 3D surface velocity fields using a feature-tracking algorithm and the Multiscale Model to Model Cloud Comparison algorithm. The comparison between the horizontal surface velocities detected by the feature-tracking algorithm and horizontal velocities from GNSS measurements provided high correlation with an $R^2 = 0.99$ and a Root Mean Square Error (RMSE) lower than 0.07 m/y. The range of flow velocity of the rock glacier increased from 0.17-1.1 m/y in 2013 to values of 0.23-1.9 m/y in 2020. Subsequently, the relationship between horizontal surface velocities, extent of frozen ground at depth and thermal state of permafrost were investigated. The results showed that the heterogeneous distribution of frozen ground occurrence at depth, its structure and the thermal ground regime are key factors explaining the Gran Sometta flow pattern. Annual warmer surface conditions promote an acceleration of the creep rates within the rock glacier permafrost whereas ground surface cooling favour a deceleration phase. The subsurface ice is close to melting conditions and the investigated permafrost appears to be in imbalance with the current climatic conditions.

The second study investigates the morphological modifications and kinematics of the Plator rock glacier using an image correlation algorithm on orthoimages between 2012 and 2020. Then the creep rates were evaluated as a function of the rock glacier geometry and material properties using the Bulk

Creep Factor (BCF). The results showed that the variability in the horizontal surface velocities can be explained by the rheological properties (BCF) but a unique relation with the surface slope angle, which in turn is not directly related to BCFs, cannot be found. The creeping process increases with the BCFs, reaching large (BCF < 20) and discontinuous values typical of rock glaciers experiencing destabilization behaviour. Given the fast-moving phase, the advancement of both the front line and the front toe of the rock glacier, the formation of recent fissures, and the contrasting spatial distribution in the BCFs, the investigated rock glacier could be considered as destabilised rock glacier.

The third study quantifies the Gran Sometta rock glacier contribution on the catchment runoff and investigates the rock glacier groundwater circulation. Salt injections on the mainstream of the investigated area, and two artificial dye tracers (Tynopal and Fluorescein) inputs on the rock glacier surface were performed. This information was then integrated with electrical conductivity (EC) measurements and water temperature, covering a period between June and October in 2019, 2020 and 2021. The analysis highlights the hydrological relevance of the rock glacier as a complex geomorphological feature with important water storage capabilities. Despite covering only 34% of the total catchment, the relative contribution of the rock glacier increased towards the end of summer season and the beginning of autumn with highest influence (65%) on the mainstream in September-October. The EC contribution of the rock glacier is lowest in early summer (48%) and successively increases towards early autumn (63%). The low temperature of the water discharge of the rock glacier suggests that the water flow is in direct contact with ground ice or permafrost and has the ability to lower the average stream water temperature, by ca. 2.8 °C.

Throughout this dissertation, drone-based data demonstrated to be a valuable approach to detect the spatial information of rock glacier flow patterns such as

displacement maps, vertical changes and geomorphologic information. Combining this information with data on the internal structure and hydrogeology of rock glaciers is of fundamental importance for a correct understanding of the flow mechanism of such landforms.

1 INTRODUCTION

1.1 Motivation and importance of the research field

Mountain permafrost is mainly characterized by rough terrain in a complex topography with spatially variable microclimatic conditions and ground properties (Haeberli et al., 2010). Heat transfer occurs between atmosphere and ground, which is strongly influenced by the timing and thickness of snow cover and by surface and subsurface properties such as terrain roughness, porosity, water and ice contents and the thermal conductivity of materials (Cicoira et al., 2019; Hausmann et al., 2012; Martin and Whalley, 1987). Changes in high-mountain permafrost in steep terrains can influence the frequency and magnitude of natural hazards with consequences at the local and regional scale. Although many studies address these issues, our knowledge of the models and the fundamental mechanisms linking climate forcing to permafrost creep is still a source of debate.

Permafrost is considered one of the Essential Climate Variables (ECV) by the Global Climate Observing System (GCOS) and rock glacier kinematics has recently been included as an associated parameter by the International Permafrost Association (IPA). Rock glaciers and their dynamics have received increasing attention in recent years in the study of the impact of global warming on permafrost in high mountain environments (Eriksen et al., 2018; Hartl et al., 2016) and represent key features to understand the response of mountain cryosphere to climate change (Marcer et al., 2021; Wirz et al., 2016b).

A significant increase in rock glacier flow rates and the onset of destabilizing phenomena of some of them have been recorded since the 1990s, in parallel with rising air temperature, soil warming and ice loss (Jones et al., 2018; Kellerer-Pirklbauer et al.; 2018; Wirz et al., 2016). Their current thermal and dynamic

behaviour provide information about present and past environmental conditions of mountain permafrost (Kofler et al., 2020; Cremonese et al., 2011; Boeckli et al., 2012). Since the morphology of active rock glaciers reflects both their current dynamic state and their dynamic history (Kääb et al., 2007; Haeberli et al., 2006; Frauenfelder and Kääb, 2000), age dating techniques and displacement mapping are useful aspects for making paleoclimatic considerations and landscape evolution during the late-glacial and the Holocene (Frauenfelder et al., 2001; Humlum, 1998; Clark et al., 1996), as rock glaciers preserve significant climate archives (Scapozza et al., 2017; Krainer et al. 2015; Thies et al., 2013; Haeberli et al., 1999; Humlum, 1998).

In addition to the increasing movement of rock glaciers, the expected effects of the future decline of the mountain cryosphere pose far-reaching challenges for effective freshwater resource management. Rock glaciers are persistent mountain reservoirs, significant in a warming world (Rangecroft et al., 2015; Jones et al., 2018, 2019), suggesting that these landforms represent long-term water storage in high mountain systems (Bosson and Lambiel, 2016; Millar et al., 2013). Although nowadays the ice thaw contributes to a minor fraction (<5%) of the total discharge from rock glaciers (Wagner et al., 2020; Krainer et al., 2015), this ice represents an important water reservoir in the long term (Jones et al., 2018), especially under uncertain climate predictions. Recent studies show that the thawing rock glaciers often export solute-enriched waters, which can modify the inorganic chemistry of the entire river network, affecting biological communities and with strongly consequences also on ecological and water management issues (Brighenti et al., 2021; Scapozza et al., 2017; Thies et al., 2013). The high storage capacity of rock glaciers impacts on water resources in Alpine catchment could also potentially regulate the risk of natural hazards, such as floods and debris flows.

Given the worldwide abundance of rock glaciers in mountain settings, understanding the interaction between rock glaciers dynamics, internal and superficial deformations, thermal state of permafrost and hydrology (e.g., quantification of discharge rates, effect of trace elements enrichment in waters influenced by rock glaciers) bears an enormous scientific and applied value at the global scale.

1.2 Drone surveys for rock glacier monitoring

Drone surveys are increasingly used for geomorphological monitoring and mapping due to the large availability of automated close-range photogrammetry techniques and user-friendly software (Colomina and Molina, 2014). The use of drone photogrammetry has multiple advantages, such as (i) low cost, (ii) ability of platforms to perform autonomous missions, and (iii) possibility of flying at low altitudes and over complex and/or difficult-to-access terrain.

For mapping applications, the most used drones are rotary-wings (i.e., multirotor) or fixed-wings platforms (Nex and Remondino, 2014), equipped with a RGB digital camera. In the field, drone platforms collect multiple images, which are successively processed in commercial photogrammetric software packages (such as Agisoft Metashape) that implement a Structure-from-Motion (SfM) workflow (Smith et al., 2016; Westoby et al., 2012). The SfM approach is a set of different algorithms that, matching the same features in digital images, can reconstruct the 3D geometry of the terrain from images taken from different angles and viewpoints (Fonstad et al., 2013; Westoby et al., 2012).

Drone platforms, together with photogrammetric techniques, generate very high-resolution datasets with centimetre to decimetre accuracy, such as point clouds, Digital Surface Models (DSMs) and orthorectified images (orthoimages). The accuracy of these products is influenced by various factors related to the camera (Clapuyt et al., 2016), the flight parameters (Rock et al., 2011) and the

number and the spatial distribution of the Ground Control Points (GCPs) required for georeferencing the acquired images (Kääb et al., 2014).

Regular monitoring achieved by repeated drone flights is widely adopted in the study of glacial and periglacial processes (Vivero and Lambiel, 2019; Piermattei et al., 2016; Rossini et al., 2018). Products derived by multi-temporal drone surveys are firstly computed with SfM workflow to generate high resolution datasets and successively processed using image correlation analysis (e.g., CIAS software), feature tracking algorithm (e.g., IMCORR module within SAGA-GIS) and operations on dense point clouds (e.g., Multiscale Model-to-Model Cloud Comparison plugin into CloudCompare) to obtain 2D and 3D motion field of rock glaciers creep (Fey and Krainer, 2020; Hendrickx et al., 2019; Vivero and Lambiel, 2019; Zahs et al., 2019; Dall'Asta et al., 2017; Fey et al., 2015; Kaufmann and Ladstädter, 2003). The quantification of surface displacements and elevation changes, the identification of destabilisation features and the investigation of the destabilisation phase of rock glaciers are therefore made possible exploiting the use of drone combined with the availability of advances photogrammetry techniques and software.

Under warming conditions, deformation and potentially destabilization of rock glaciers are expected to increase, potentially triggering natural hazardous phenomena. Fine resolution datasets of the kinematics of rock glaciers are therefore required to monitor the rate of permafrost deformation and be able to make future predictions about its behaviour.

1.3 Permafrost and rock glacier creep

Permafrost is thermally defined as ground material where temperature remains at or below 0 °C for at least two consecutive years (Biskaborn et al., 2019). The thermal state of permafrost is sensitive to changing climatic conditions such as increasing air temperature and changing snow regimes. As a result of global

warming, permafrost is currently experiencing warming and thawing (Biskaborn et al., 2019; Chadburn et al., 2017; Harris et al., 2003). Such changes would have consequences for ecosystems, hydrological systems, infrastructure integrity and human activities in high mountain environments (Cicoira et al., 2019; Duvillard et al., 2019; Jones et al., 2019; Jones et al., 2018; Haeberli et al., 2017). Permafrost degradation also involves the release of carbon, previously locked in frozen organic matter, and successively decomposed into carbon dioxide and methane, greatly affecting the Earth's climate system (Schuur et al., 2015; Anthony et al., 2012; Schuur et al., 2008).

As a consequence of the amplification of the atmospheric warming with elevation, major changes in both the extent and the dynamics of mountain permafrost are increasingly occurring (Haeberli and Beniston, 1998). In most cases, permafrost is invisible on the surface and its occurrence can be detected through geomorphological evidence such as rock glaciers, which are the visible expression of the creep of the mountain permafrost.

Rock glaciers can be found in cold mountain regions (Jones et al., 2019) and they are lobate or tongue-shaped landforms, consisting of an unconsolidated coarse debris layer (called *active layer*) covering ice supersaturated debris or pure ice (Berthling, 2011; Haeberli et al., 2006). This active layer (few metres thick) insulates the underlying permafrost body, which constitutes the main layer of the rock glacier. Permafrost body has a smaller proportion of coarse debris per volume than the active layer, a volumetric ice contents generally between 40% - 90% (Krainer et al., 2015; Hausmann et al., 2012, Haeberli et al., 2006; Arenson et al., 2002) and its thermal regime is mainly controlled by heat conduction (Cicoira et al., 2019). Due to the slow propagation of annual thermal anomalies into the permafrost layers up to 10-30 m depth, ground surface temperature (GST) reflects the variations of the temperature of the upper permafrost layers with a delay of several months (Staub et al., 2016; Delaloye et al., 2010; Haeberli

et al., 2006). Ground temperature, together with the rock glacier external (i.e., topographical conditions) and internal (i.e., internal structure and composition) characteristics, controls therefore the deformation of perennially frozen ground and the associated rock glacier flow velocities (Haberkorn et al., 2021; Arenson et al., 2002). Indeed, the increased rock glacier morphodynamics has been explained by rising air and ground temperatures, heat conduction mechanisms, meltwater advection (Staub et al., 2016; Wirz et al., 2016; Delaloye et al., 2010; Ikeda et al., 2008), liquid water content and ice content variations (Cicoira et al., 2019; Buchli et al., 2018; Kenner et al., 2017).

A significant increase in flow velocities of rock glaciers has been documented since the 1990s by several studies (Marcer et al., 2021; Hartl et al., 2016; Kellerer-Pirklbauer et al., 2012). Normally rock glaciers move at rates between a few centimetres to a few meters per year, but some recent studies showed that some rock glaciers are experiencing destabilisation processes, occasionally resulting in landslide-like events with displacements of up to several tens of meters per year (Kofler et al., 2021; Vivero and Lambiel, 2019; Bodin et al., 2017; Scotti et al., 2017). It follows that the response of rock glacier morphodynamics to atmospheric warming and climate change is of a great scientific interest for both climate change forecasts and landscape evolution models.

1.4 Hydrology of active rock glaciers

In literature, several terminologies are used to describe the status of rock glaciers. Some inventories distinguish between *active rock glaciers* (containing ice and displaying movement), *inactive rock glaciers* (containing ice and no longer displaying movement) and ice-free rock glaciers (Haeberli, 1985; Barsch, 1996) whereas others refer only to the presence (*intact rock glaciers*) or absence (*relict* or *fossil rock glaciers*) of frozen material (Scotti et al., 2013). However,

the term *intact rock glaciers* is commonly used to indicate both *active* and *inactive rock glaciers.* Intact rock glaciers contain a significant volumes of ice (Jones et al., 2018). Due to the presence of the active layer and its insulating effect, rock glaciers have a retarded melting effect of ice and ground perennially frozen layers, suggesting that these landforms may prolong long-term water storage in high mountain systems (Jones et al., 2018; Bosson and Lambiel, 2016; Corte, 1976).

Although meltwater is an important component of intact rock glaciers, causing the development of drainage networks, there is not much detail information about how the hydrological regime of active rock glaciers affects the flow of rivers and streams in high mountain areas. In intact rock glaciers, the released water derives from snowpack melting, glacier ice melting and perennially frozen ground melting, with contributions from rainfall and groundwater (Krainer and Mostler, 2002). Commonly, highest discharge rates occur during snowmelt in spring/early summer and gradually decrease through summer and autumn, while the lowest flow rates are recorded in the winter season (Krainer et al., 2007; Krainer and Mostler, 2002). Discharge rate is usually characterised by diurnal and seasonal variations, with peak associated with snowmelt and rainfall events (Krainer and Mostler, 2002) and the temperature of water draining from active rock glaciers has been reported to be around the freezing point (Millar et al., 2013; Krainer et al., 2007). This suggests that the water flows is in direct contact with permafrost and has the ability to lower the average stream water temperature (Jones et al., 2018).

Runoff of active rock glaciers is complex and determined by the interaction of several parameters, particularly by local weather conditions, properties of debris layers (such as thermal conditions, thickness, and grain size), physical mechanism controlling the flow of water through the rock glacier and presence/absence of frozen body (Jones et al., 2018; Krainer and Mostler, 2002).

Hydrographs of active rock glacier show that as long as the rock glacier is covered by snow, a major part of the meltwater derives from snowmelt. Studies reported an increased in electrical conductivity (EC) in the rock glaciers spring in the period from May to October (Krainer et al., 2007; Krainer and Mostler, 2002) due to increasing seasonal contributions of weathering fluxes from groundwater and ice melt (Williams et al., 2006).

To recognize the effect of global warming on the hydrological cycle in alpine regions, shallow groundwater systems need to be better understood in the light of climate change. Understanding the hydrology of rock glaciers and their catchments, which is still a largely unexplored field of research, are increasingly relevant to a better comprehension of the significance of this little-known freshwater resource (Jones et al., 2019, Wagner et al., 2019). More research is necessary to estimate rock glaciers distribution and their ice content, in order to quantify their total contribution to alpine streamflow under warming climates.

1.5 Research questions and thesis outline

The aim of this thesis is to study the processes governing the rock glacier dynamics and its temporal and spatial variations in a context of climate warming. The thesis seeks to answer three questions:

- How perennially frozen debris, ground surface temperatures and meteorological conditions affect the rock glacier dynamics?

  This investigation is addressed in chapter 2.
- Is it possible to detect rock glacier destabilization using only drone-based data?

  This investigation is addressed in chapter 3.
- What is the role of unfrozen water discharging from rock glaciers in the catchment runoff?

  This investigation is addressed in chapter 4.

The thesis is structured as a collection of three scientific papers, each presented in a specific chapter with its own abstract, introduction, study site, material and methods, results, discussion, conclusions and references. The activities were carried out in two field sites: the Gran Sometta rock glacier (Valle d'Aosta, Italy) and the Plator rock glacier (Lombardia, Italy).

Chapter 1 is a general introduction, in which the framework of the Ph.D. project and the overall and specific objectives are presented.

In chapter 2, the activities addressing the first objective of the Ph.D. research are presented. The study focused on four main activities: firstly, analyse the 3D surface variations and displacement velocity variability of a rock glacier between 2012 to 2020; secondly, validate the movement rate obtained by a feature-tracking algorithm against GNSS (Global Navigation Satellite Systems) measurements; thirdly, understand how the extent of frozen material at depth affects the horizontal surface velocity; fourthly, investigate the link between Ground Surface Temperature (GST) and rock glacier dynamics.

In chapter 3, the second objective of this Ph.D. research is presented. In this study, the spatial and temporal distribution of rock glacier displacements was evaluated and interpreted as a function of the Bulk Creep Factor (BCF) and rock glacier topography. Based on the BCF and remote sensing observations (from drone-derived data) on creep velocities and surface slope angle, the rock glacier areas currently experiencing destabilization or set in conditions unfavourable to permafrost occurrence were defined.

In chapter 4, the outcomes of the activities addressing the third objective of this thesis are presented. This study explored the hydrological significance of an active rock glacier. A conceptual model related to the water circulation of a rock glacier and the rock glacier contributions downstream of the system were analysed. To do this, flow rate quantifications, tracers' inputs and hydrological activities were performed.

Chapter 5 concludes this thesis by summarising the main findings of this research and proposing suggestions for future work.

All the analyses presented in this thesis are based on a collaboration between the University of Milano-Bicocca (Department of Earth and Environmental Sciences) and ARPA VdA (Climate Change Unit). This Ph.D. project is funded by the Italian MIUR project Dipartimenti di Eccellenza 2018-2022 and is supported by the GEMMA (Geo Environmental Measuring and Monitoring from multiple plAtforms) laboratory of the University of Milano-Bicocca.

2 KINEMATICS OF AN ALPINE ROCK GLACIER FROM MULTI-TEMPORAL UAV SURVEYS AND GNSS DATA

The content of this chapter is published in Geomorphology as: Bearzot F., Garzonio R., Di Mauro B., Colombo R., Cremonese E., Crosta G.B., Delaloye R., Hauck C., Morra Di Cella U., Pogliotti P., Frattini P., Rossini M., 2022. "Kinematics of an Alpine rock glacier from multi-temporal UAV surveys and GNSS data". Geomorphology, 2022. Doi: 10.1016/j.geomorph.2022.108116.

Abstract

The quantification of rock glacier dynamics has gained increasing importance in recent years. In this study, the spatial and temporal flow patterns of perennially frozen debris in the active Gran Sometta rock glacier (Western Italian Alps) were investigated with repeated Unmanned Aerial Vehicle (UAV) surveys (2016-2019), Global Navigation Satellite System (GNSS) campaigns (2012-2020), geophysical prospections (2015) and ground surface temperature data (2014-2020).

UAV data were used to generate maps of changes and elevation differences of the rock glacier surface by 3D point cloud comparison to evaluate surface lowering and accumulation processes. Horizontal velocities were quantified by an automatic image correlation technique and the results were then compared with horizontal surface velocities from GNSS measurements on selected points. The horizontal velocities estimated with the automatic method agree well with the GNSS velocities with an $R^2 = 0.99$ and a RMSE lower than 0.07 m/y.

Point cloud comparisons show surface lowering in the orographic left-hand side of the terminal part and in the central body of the rock glacier. The upper part exhibits almost absence of subsidence and any movement. This is explained by the lack of permafrost in this sector due to its overriding by the development

of a small glacier during the Little Ice Age. As a result of the downslope movement, zones of surface rising occurred at the advancing front and at the moving ridge and furrow complexes. Surface velocity decreases from the orographic left to the right-hand side of the rock glacier tongue, where a thaw subsidence of up to 0.05 m/y was also observed. According to the GNSS measurements, the range of flow velocity of the rock glacier increased from 0.17-1.1 m/y in 2013 to 0.21-1.45 m/y in 2015 and then decreased until 2018 when the smallest surface velocity is detected. Since 2018, the creep velocities gradually started to increase again reaching values of 0.23 m/y up to a maximum of 1.9 m/y in the orographic left-hand side of the rock glacier tongue. This agrees with observations from other rock glaciers in the European Alps in recent decades.

The complex Gran Sometta rock glacier dynamics can be explained by the heterogeneous distribution of permafrost and related subsurface perennially frozen ground which is thick enough (about 20-30 metres) for permafrost creep to occur. Creep rates of the rock glacier permafrost depend also on the ground thermal regime: annual warmer surface conditions promote an acceleration of the creep rates within the rock glacier permafrost, whereas ground surface cooling causes a slight deceleration.

2.1 Introduction

Active rock glaciers are widely recognized as creep phenomena of mountain permafrost (Haeberli et al., 2006; Barsch, 1992; Wahrhaftig and Cox, 1959). They consist of a mixture of rock/debris and ice, and represent key features to understand the response of mountain cryosphere to climate change (Hartl et al., 2016; Wirz et al., 2016b).

Changing climatic conditions and in particular the increase of air temperature strongly influence the thermal state of permafrost (Etzelmüller et al., 2020; Biskaborn et al., 2019). Recent studies showed that ground temperature, together

with the rock glacier external (i.e. topographical conditions) and internal (i.e. internal structure and composition) characteristics, controls the deformation of perennially frozen ground and the associated rock glacier flow velocities (Haberkorn et al., 2021). In particular, annual variations in rock glacier surface velocities have been related to ground surface temperature (GST) variations that reflect, with a delay of several months, the variations of the temperature of the upper permafrost layers due to the slow propagation of annual surface thermal anomalies deeper into the permafrost layers up to 10-30 m depth (Staub et al., 2016; Delaloye et al., 2010).

During the last decades flow velocities were measured on many rock glaciers in the Alps (Bodin et al., 2018; Kellerer-Pirklbauer et al., 2017; Delaloye et al., 2010; Delaloye et al., 2008). Monitoring changes of rock glacier surface velocity and geometry may provide insights on ongoing processes such as ice melt at the permafrost table or base, deformation of the permafrost body and displacement at shear horizons where 50-95% of the total deformation occurs (Cicoira et al., 2021; Kenner et al., 2019; Cicoira et al., 2019; Delaloye et al., 2010). The rock glacier movement can span from few centimetres to several metres per year, depending on creep characteristics, such as the occurrence and depth of shear horizon, influence of liquid water (Cicoira et al., 2019; Ikeda et al., 2008), topographical factors (e.g. slope angle) (Cicoira et al., 2021; Marcer et al., 2019; Delaloye et al., 2013) and ground thermal regime (Staub et al., 2016; Buchli et al., 2013). Changes in rock glacier dynamics are reflected in thickness variations (Cusicanqui et al., 2021), called “negative surface changes” and “positive surface changes” through the text. Negative surface changes refer to surface lowering and mass loss processes whereas positive surface changes depend on accumulation processes and mass gain due to the rock glacier advancement.

Rock glacier surface geometry changes over time were quantified using tachymetric surveying techniques (e.g., triangulation) and differential GPS

(Krainer and Mostler, 2006; Lambiel and Delaloye, 2004). More recently, the detection and evaluation of three-dimensional deformations, the generation of velocity fields and the high-resolution reconstruction of rock glacier surface have been made possible by remote sensing techniques (i.e. Unmanned Aerial Vehicle –UAV- surveys, terrestrial and airborne laser scanning) combined with computer-based data processing (Kaufmann et al., 2018; Kummert and Delaloye, 2018; Bauer and Paar, 2003). Structure-from-Motion (SfM) photogrammetry is a valuable tool for geomorphological research applications (Hendrickx et al., 2019; Westoby et al., 2012) allowing the creation of high-density point clouds, high-resolution orthophoto mosaics and Digital Surface Models (DSMs) starting from extensive datasets of overlapping images.

Digital image correlation of multi-temporal UAV images recently allowed for the quantification displacement fields over several landforms, including glaciers, landslides, and rock glaciers (Fey and Krainer, 2020; Rossini et al. 2018; Dall'Asta et al., 2017; Wigmore et al., 2017; Lucieer et al., 2014). Other authors suggested the use of a 3D approach to detect multi-directional surface changes in high mountain areas with complex topography (Zahs et al., 2019; Fey et al., 2015; Kaufmann and Ladstädter, 2003).

In this study, the morphological and dynamic changes of the Gran Sometta rock glacier (south-western Italian Alps, Cervinia, Aosta Valley) are analysed and the rock glacier response to the interannual variability of GST and meteorological data is discussed. Data collected on the same rock glacier have also been used in the methodological work by Dall'Asta et al. (2017) which focused on the comparison of the performances of two automatic procedures applied to both orthophotos and DSMs with the manual identification of corresponding features on orthophotos in estimating surface displacements. Here, the temporal evolution of the Gran Sometta surface displacements and 3D change between 2016 and 2019 is characterized and discussed in relation to the rock

glacier internal structure, surface morphology and GST data. To achieve these goals, multi-temporal high-resolution UAV surveys were performed from 2016 to 2019 and two Electrical Resistivity Tomography (ERT) profiles were performed to identify the internal structure and potential frozen ground inside the main body of the rock glacier in 2015. In addition to UAV surveys, GNSS campaigns were performed from 2012 to 2020. In particular, the specific aims of this study are: (i) to analyse the 3D surface variations and displacement velocities of the rock glacier and their variability between 2012 and 2020, (ii) to validate the movement rate obtained by a feature-tracking algorithm against repeated GNSS measurements, (iii) to understand how the extent of frozen ground at depth across longitudinal ERT profiles affects the horizontal surface velocity and (iv) to investigate the link between GST data and rock glacier dynamics.

2.2 Study site

2.2.1 Gran Sometta rock glacier

The study area is located on the south-western side of the central Alps at the head of the Valtournenche Valley (Aosta Valley, Italy) (Fig. 1a). Two lobes, at an elevation ranging from 2630 to 2770 m a.s.l, compose the main body of the rock glacier. It is approximately 400 m long, between 150 and 300 m wide with a thickness of 20-30 m (estimated from the height of rock glacier front). On the orographic left-hand side of the main body of the rock glacier tongue, a third lobe (Fig. 1c), 215 m wide and 192 m long, has a front located at about 2700 m a.s.l.

The surface of the rock glacier appears as a debris mass consisting of pebbles and angular blocks, in most places lacking any finer-grained matrix. The body is characterized by longitudinal ridges in the extensive central part and a complex of transverse ridges and furrows in the compressive terminal part of the tongue. The debris originates from the rock walls of the Gran Sometta peak, mainly

composed by green schists with prasinites, with bands of dolomite and marbles (Dall'Asta et al., 2017). Soil is absent or only very thin and the matrix is clearly subordinate and sandy-gravelly in nature.

The study of morphological and dynamic changes was conducted on four main sectors of the rock glacier body (i.e. external lobe, black lobe, white lobe, and upper part, Fig. 1c) based on (i) geomorphological characteristics, (ii) debris cover layer and (iii) previous information on the spatial distribution of displacements.

The external lobe (sector I) extends from about 2700 m a.s.l. (front lobe) up to approximately 2750 m a.s.l. The black lobe (sector II) goes from the ski slope at 2630 m a.s.l. to 2750 m a.s.l., while the white lobe (sector III) ranges in elevation from 2630 to 2715 m a.s.l. The upstream part (sector IV), with elevation ranging from 2715 to 2750 m a.s.l., was the part affected by the Little Ice Age (LIA) glacier. In the orographic upper left part of the main tongue, a push-moraine developed whose current deformation mode is partly a back-creeping process towards the thalweg where the small LIA glacier tongue was developing. This is creating most of the elongated features visible in this part of the rock glacier.

According to the IPA Action Group Rock glacier inventories and kinematics (IPA, 2020), the Gran Sometta rock glacier can be classified as "glacier forefield-connected", that is a rock glacier where the interaction glacier-rock glacier is pervasive but limited to a glacier advance phases such as in the LIA, as reported by the same document. For the sake of simplicity, the Gran Sometta rock glacier will be referred to as "rock glacier" through the text.

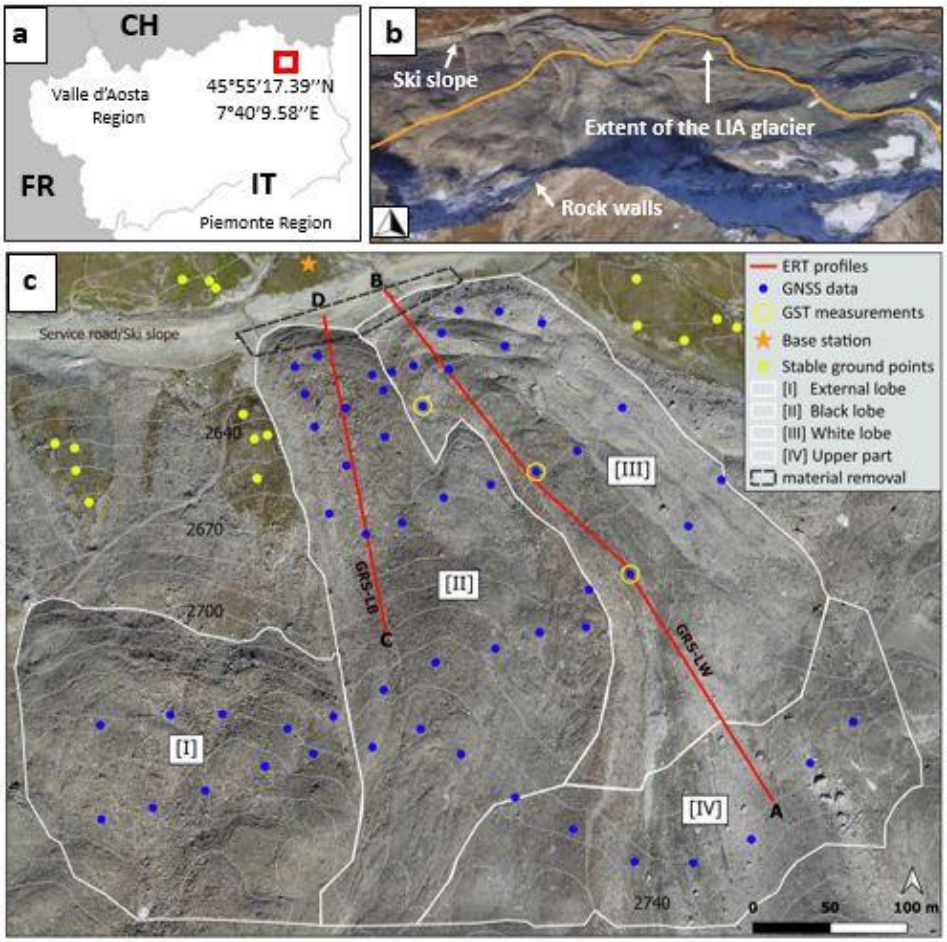

Figure 1. Overview map of the study site. (a) Location of the study site in SW eastern Italian Alps. The coordinates of the rock glacier site are given in the WGS 84 coordinate system; (b) approximate extent of the LIA glacier at Gran Sometta; (c) detailed view of the rock glacier with sector subdivision, locations of the GNSS/RTK base station, ERT profiles, GNSS measurement points, GST measurements, 16 stable ground points, and artificial reworked area. The orthophoto was taken on August 2016.

2.2.2 Little Ice Age in the Alps and in the Cervinia basin

During the Little Ice Age (LIA, 15th – 19th century), small glaciers (< 1 km^2) were situated over the Alpine permafrost area. Glacier advancements later led to changes in the landscape, visible today with distinct moraine structures (Kneisel and Kääb, 2007; Reynard et al., 2003). The areas temporarily covered by the ice masses were thermally isolated and possibly warmed up while the conditions for perennially frozen sediments and ground ice preservation and formation were

favoured at the front and outside these small glaciers, typically on push-moraines (Delaloye and Lambiel, 2008). Push-moraines are glaciotectonized frozen sediments, evidence of geometrical deformation due to glacier dynamics, and represent the morphological expression of permafrost deformation (Reynard et al., 2003; Bennet, 2001; Haeberli, 1979). The retreat of these small glaciers in favourable permafrost conditions has uncovered forefields, some of which containing thick coarse deposits of glacial and periglacial origin, where permafrost can aggrade and/or creep occur. Commonly, the central part of most LIA Alpine glacier forefields is today either permafrost-free or occupied by degrading debris-covered glaciers or buried ice patches (Delaloye and Lambiel, 2008).

The extent of the LIA glacier at Gran Sometta is shown in Fig. 1b and can only be approximated because there was neither any terminal moraine deposit (common for cold margins of such small glaciers pasting on formerly frozen debris) or because of debris reworking (principally by creep processes). This approximate extent represents the area where geomorphological evidences (e.g. push-moraines and fluted moraines, ground surface texture, absence of debris sorting, bedrock outcrops and surface morphology smoothness) of a glacier cover are visible both on site and remotely.

2.3 Data and methods

2.3.1 Multi-temporal UAV data

Four UAV surveys of the rock glacier body were conducted from 2016 to 2019 in the absence of snow cover.

The flight of the first campaign (i.e., 2016) was conducted by a senseFly eBee RTK fixed-wing equipped with a SONY DSC-WX220 digital camera (RGB), 4896×3264 pixels resolution and optical sensor size 1/2,3". Mission was planned by using senseFly Emotion 3. Photos were shot from 140 m above ground level,

at a 10-12 m s^{-1} mean flight speed and with 60% and 70% of longitudinal and lateral overlap, respectively. The subsequent surveys were carried out with two different DJI Phantom 4 multicopters: a Phantom 4 Pro (on 2017 and 2018) and a Phantom 4 RTK (on 2019). The first one carries a DJI FC6310 camera with an 8.8 mm nominal focal length, and a 1" CMOS 20-megapixel sensor with 2.41 x 2.41 µm nominal pixel size. The resolution is 5472 x 3648 pixels corresponding to 13.2 x 8.8 mm. The RTK version is equipped with a DJI FC6310R camera which has a glass lens rather than the plastic one fitted on the Phantom 4 Pro. Drone Harmony and DJI GS were used to plan and execute missions.

Further details about the UAV campaigns are reported in Table 1.

Date	Coverage area (km^2)	Ground resolution (cm/px)	Flying altitude (m above ground level)	Camera model	UAV	Number of images
24/08/2016	0.553	4.0	140	Sony DSC-WX220 (18,2 Mpx)	SenseFly eBee RTK	169
26/08/2017	0.407	1.8	70	FC6310	DJI Phantom 4 Pro	993
23/08/2018	0.418	2.4	90	FC6310	DJI Phantom 4 Pro	632
21/08/2019	0.366	2.1	80	FC6310R	DJI Phantom 4 RTK	392

Table 1. Details of the four UAV surveys performed between 2016 until 2019.

2.3.2 GNSS data

Several photogrammetric markers have been evenly located on the whole study area and their coordinates were measured during each drone acquisition. Markers coordinates were acquired by differential GNSS receivers (GEOMAX Zenith 20 and Zenith 35 Pro), in which a Real-Time Kinematic (RTK) measurement technique was applied. Two GNSS devices were used simultaneously: a master and a rover. The master station was installed on a rock outcrop on the front of the rock glacier (Fig. 1c). Its position was previously

determined with an ad hoc acquisition, which was used as a static reference point for all the RTK surveys. The rover was used to measure the centre points of each marker with a fixed solution. According to GNSS/RTK measurements, the average accuracy of the topographic surveys was 1.8 cm for planimetric coordinates and 2.0 cm for elevation. Approximately 60% of the Ground Control Points (GCPs) were used for orthophoto and DSM generation and the remaining 40% (Check Points – CPs) was used for the validation of the generated models. The GCPs used were 11 for the 2016 and 2017 surveys and 12 for the 2018 and 2019, while the CPs were 6 (2016), 8 (2017 and 2018) and 7 (2019).

The monitoring activity also includes GNSS campaigns. For the black and white lobes, the time series run annually from 2012 to 2020, whereas for the external lobe data acquisition covers the years 2015-2020. GNSS provides highly accurate surface displacement measurements but limited to selected points. Here, 54 points (Fig. 1c) were used to extract annual surface velocity of the rock glacier and used for the validation of the results derived from photogrammetry. The control points were measured with a GNSS receiver Leica Viva GS10/15 in RTK mode (the base station was installed on the same rock outcrop on the front of the rock glacier, Fig. 1c), with an expected precision of 1 cm horizontally and 2 cm in elevation.

2.3.3 Geophysical surveys

On 22 and 23 July 2015, two ERT profiles were performed to characterize the internal structure and identify potential frozen ground inside the main body of the rock glacier. The two profiles were conducted along the flow line direction of the black and white lobes, respectively (see Fig. 1c). For both profiles, a Syscal (Iris Instruments, France) was used and the Wenner-Schlumberger configuration was adopted. The profile on the white lobe (GRS-LW) was 470 m long with 48 electrodes at 10 m spacing, whereas the profile on the black lobe (GRS-LB)

consisted of 48 electrodes with 5 m spacing resulting in 235 m profile length. The measured apparent resistivity data sets were filtered according to Mollaret et al. (2019) and inverted to give the 2-dimensional distribution of specific resistivity using the inversion software Resdinv (Loke, 2020).

2.3.4 Ground surface temperature and meteorological data

Ground surface temperature (GST) is the surface or near-surface temperature of the ground, measured within the uppermost centimetres of it (PermaNET, 2011), and corresponds to the temperature at the top of the active layer. GST measurements were recorded every two hours using autonomous miniature temperature data loggers (UTL-1 and more recently UTL-3, Geotest AG, Switzerland) from 2014 to 2020. Three MTD's are placed on the rock glacier surface (Fig. 1c) to monitor the GST in the near sub-surface at depths of one to 10 centimetres, in order to avoid direct radiation influence. Based on the GST measurements, we calculated the mean annual ground surface temperature (MAGST), the ground freezing index (GFI), the ground thawing index (GTI) and the winter equilibrium temperature, WEqT. The MAGST represents a "thermal memory" of the ground of 12-month running mean from August to August and allows identifying periods of cooling or warming of the ground surface. The GFI (and GTI) index is the sum of all daily mean values < 0°C (>0°C) considering the period November-May (June-October) and indicates how cold (or warm) a year was at the ground surface. The WEqT is assessed through the bottom temperature of the winter snow cover (BTS), which measures the temperature at the snow-ground interface (PermaNET, 2011). Therefore, the WEqT is strongly dependent on the snow cover condition (height and duration) and is a valuable indicator of permafrost occurrence. WEqT is the equilibrium value, as a function of the heat flux coming up from the ground, which is reached when the GST

stabilises following a sufficient snow cover for insulation from atmospheric variations (PermaNET, 2011).

Additionally, gridded data of air temperature (T_{air}) and Snow Water Equivalent (SWE) were generated by the hydrological model GEOtop (Endrizzi et al., 2014) for the study area and solves the energy balance at single grid level (50 m resolution) at hourly step, starting from spatialized meteorological data. T_{air} refers to the daily mean temperature calculated on the rock glacier polygon and by selecting the period from the maximum yearly SWE to the end of the snow season we identified the snowmelt period.

2.3.5 Digital Surface Models, orthophoto generation and point cloud comparison

The Structure from Motion (SfM) technique (Westoby et al., 2012) was used to generate the orthophotos and DSMs using the commercial software Agisoft Metashape, v. 1.5.5. The first step of processing was the selection of images with enough quality and overlap. These photographs were aligned using an image feature recognition algorithm to produce a sparse 3D point cloud by matching coincident features. Secondly, GCPs were manually identified in each photograph and edited when required to georeference the sparse cloud. The coordinates of the GCPs were imported to optimize the spatial accuracy of the 3D point cloud. Thirdly, a multi-view stereo image-matching algorithm was applied to increase the density of the sparse point cloud and to convert it into DSMs and orthomosaics by interpolation. The final products were extracted with a resolution of 5 cm/px. The accuracy of the DSMs and the orthophotos was estimated computing the Root Mean Square Error (RMSE), the mean error and standard deviation of error of the GCPs and the CPs. Successively, we estimated the three-dimensional change of the surface displacements of the rock glacier comparing pairs of point clouds. Overall, we made three models that simulate the

surface changes over time. Following Zahs et al. (2019), we quantified changes between each available dataset and the most recent one, for year 2019. The algorithm used was the Multiscale Model to Model Cloud Comparison (M3C2 plug-in) implemented in the open-source software CloudCompare (version v2.11 alpha). M3C2 operates directly on point clouds, computes the local distance between two point clouds along the normal surface direction, which tracks 3D variations in surface orientation. In addition, it estimates for each distance measurement a confidence interval depending on point cloud roughness and registration error (Lague et al., 2013). In our case, the reference cloud is the last cloud acquired in order of time, and the compared cloud changes according to the time interval considered. All clouds were subsampled at 0.05 m minimum point spacing for definition of the core points. The normal and projection scale were selected considering the surface roughness and the point cloud density and change for each compared dataset. The multi-scale estimation was applied into the normal scale parameter in which the minimum normal scale should be at least 20 times higher than the surface roughness at this scale, based on recommendations given in Lague et al. (2013). The projection scale was set to 1, for the 2018-2019 and 2017-2019 comparisons, and to 1.5 for the 2016-2019 interval. The maximum depth was set at 12 m since we do not expect that magnitude of the surface change can exceed this threshold for any time interval. We used the CPs RMSE of the different surveys to compute the registration error (*reg*) of the clouds by the following formula:

$$reg = \sqrt{(RMSE_x)^2 + (RMSE_{2019})^2} \quad (1)$$

where the x indicates the year used for the comparison with the year 2019.

Using the reg and considering the local point cloud roughness $\sigma_1(d)$ and $\sigma_2(d)$ measured along the normal directions, we calculated the $LOD_{95\%}$ (Level of Detection at 95%) as:

$$LOD_{95\%} = \pm 1.96 \left(\sqrt{((\sigma_1(d)^2/n_1)) + ((\sigma_2(d)^2/n_2))}\right) + reg \quad (2)$$

where n_1 and n_2 are the point clouds. Surface changes are considered statistically significant when exceeding the $LOD_{95\%}$ value (Lague et al. 2013).

The M3C2 plug-in generates a distance map that provides an accurate orthogonal distance measurement between two point clouds. From the output table of the M3C2 distance values, the empirical cumulative distribution function (ECDF) was plotted for the annual estimates of the rock glacier surface changes. In addition, the plug-in generates several other products such as the change significant map (indicates whether the distance probably correspond to a real change or not) and the xyz component of the local surface normal vectors. The predominance of one of these components, horizontal or vertical, indicates the preferential orientation of the surface changes (Lague et al.,2013).

The horizontal ground displacements of the rock glacier were estimated using the feature-tracking algorithm IMCORR (Fey and Krainer, 2020; Vivero and Lambiel, 2019; Fey et al., 2015), implemented in the SAGA GIS open source software (v. 2.3.2). The algorithm is based on finding similar features in two images acquired on the same area at different times. The estimation of the displacement vectors is based on the chosen size of the search window, identified in the least recent image, and searched it in the most recent one. The vector between the centre of the search window of the first image and the peak of the maximum correlation in the second image defines length and direction of displacement features (Fahnestock et al., 1992). Having very variable displacement values, ranging from 0.1 to 2.0 m/y, several interactions of the

algorithm were computed to obtain a set of coherent vector fields. This was achieved by varying the dimensions of the search and the reference sizes, imposing a search size of 256 (128) pixels, a reference size of 64 (32) pixels for high (low) displacement values and a grid interval of 3 or 4. Finally, the movement rates obtained by the feature-tracking algorithm were compared, point by point, against 54 GNSS points distributed on the rock glacier.

2.3.6 Evaluation of systematic errors

The geometric accuracy of the UAV-derived products was further evaluated using 16 stable ground points (outside the study landform, Fig. 1c). These were identified on orthophotos, adopting a constant scale in order to recognise the chosen point (pixel) with the same detail over the years. Horizontal displacements on stable points were calculated as the difference between the coordinates of the points in each available year and the most recent one, namely 2016-2019, 2017-2019 and 2018-2019. The presence of systematic errors in the UAV data was first evaluated computing the mean and standard deviation of the horizontal and vertical error in correspondence of the stable ground points. The image coregistration uncertainties were also estimated based on differences in elevation between the DSMs of the years 2016, 2017 and 2018 and the reference year (DSM of the year 2019) for four profiles located on the stable terrain outside the rock glacier (Cusicanqui et al., 2021). These profiles were selected after detailed visual inspection of the orthoimages in areas where no significant geomorphological changes occurred in the investigated period.

Then, the presence of "doming" (convex deformation – dome) and "bowling" (concave deformation – bowl) effects in the UAV-SfM derived products was evaluated following the methods proposed by Sanz-Ablanedo et al. (2020). This was performed quantifying vertical errors at CPs, whose coordinates were measured using a fixed GNSS/RTK technique during each UAV overpass. Such

coordinates have an accuracy of 1.2 cm and 2.0 cm for planimetric and elevation coordinates, respectively. The Z errors on CPs were fitted with a second-degree polynomial surface by using the minimum curvature algorithm implemented in the Spline with Barriers tool in ArcMap. After interpolating the error in the Z component, dome and bowl size were calculated as the value of the surface at the centre of the test area minus the average value of the surface calculated at the four corners (Sanz-Ablanedo et al., 2020).

2.4 Results

2.4.1 Frozen and unfrozen ground conditions

Fig. 2a shows the inverted ERT results for the white lobe (sector III), GRS-LW. The specific resistivity distribution shows two high-resistive bodies in the central (~30m thickness) and downslope (~20 m thickness) part of the rock glacier. Below these anomalies, which are interpreted as substantial frozen ground occurrences, the resistivity values decrease again suggesting unfrozen ground conditions. The high-resistive, frozen part is overlaid by a less resistive surface layer representing the active layer. Resistivity values < 5 kohm-m at depth, between 0 and 120 m horizontal distance, indicate the unfrozen conditions in the upper part of the rock glacier caused by the LIA glacier overriding.

Along the longitudinal profile on the black lobe (sector II) a continuous layer (20 m thick) with high resistivity values is present along the whole profile length (Fig. 2b). The GRS-LB profile is shorter and has a smaller penetration depth than GRS-LW due to the smaller electrode spacing (5 m instead of 10 m for the white lobe). Maximum resistivity values are slightly larger and more homogeneous for the black lobe (~100 kohm-m) indicating a potentially slightly higher ice content.

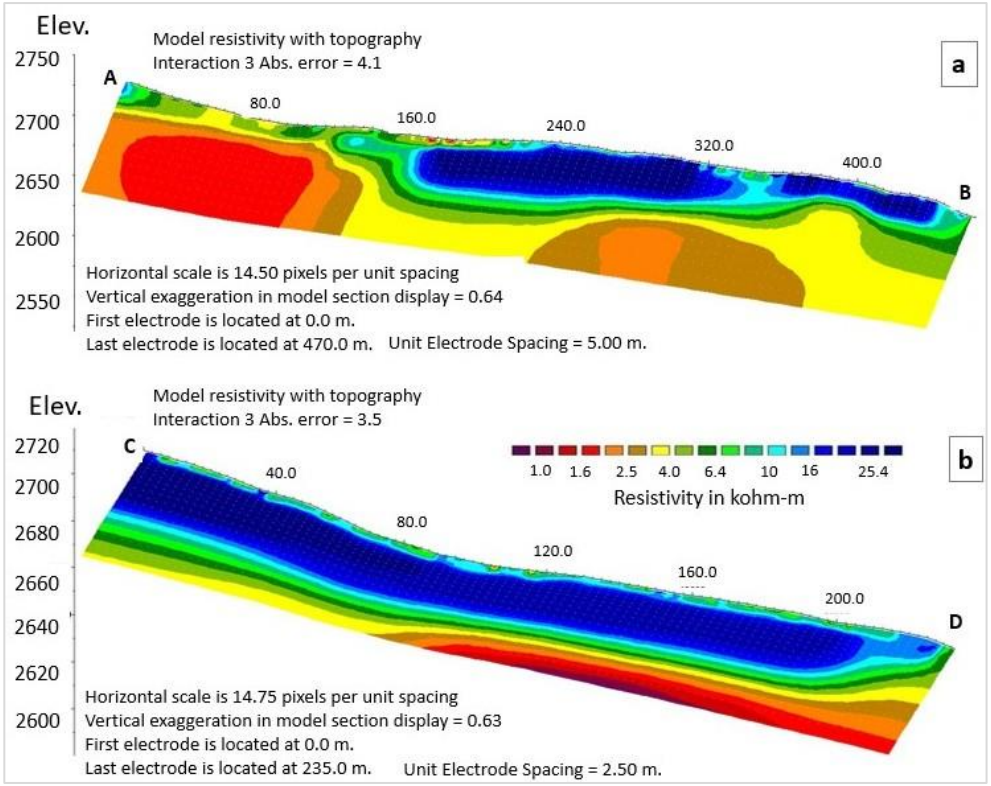

Figure 2. (a) Inverted specific resistivity distribution for profile GRS-LW from 22.7.2015 with an electrode spacing of 10 m; (b) Inverted specific resistivity distribution for profile GRS-LB from 23.7.2015 with an electrode spacing of 5 m.

2.4.2 Accuracy of point clouds and orthophotos

The accuracy of point clouds and orthophotos is assessed by computing the RMSE, mean error and standard deviation of both GCPs, used for model generation, and CPs, used for the assessment of model accuracy (Table 2). The GCP RMSE is less than 4.18 cm for all years whereas the RMSE of CPs are 5.24 cm (2016), 4.68 cm (2017), 9.34 cm (2018) and 3.51 cm (2019). The mean horizontal and vertical error were also very low, with values lower than 1 cm in most of the cases.

In Table 2, we present the values of reg (eq. 1) and $LOD_{95\%}$ (eq. 2) for each pair of data investigated in the 3D change analysis. The highest reg value (9.98 cm) is associated with the 2018-2019 comparison while, in contrast, the lowest

value (5.85 cm) occurs for the 2017-2019 interval, obtained by combining the lowest RMSE values. Since the reg is a prerequisite for the estimation of the level of detection, its value has implications in determining the $LOD_{95\%}$. The minimum $LOD_{95\%}$ (i.e., 14 cm) is found for the 2017-2019 interval in which the point clouds used are the densest, about 35M and 24M points for 2017 and 2019, respectively. On the other hand, the highest threshold value, 22 cm was again associated with the 2018-2019 interval. The cloud densities refer only to the rock glacier outline (Fig. 1c). In the end, reg and $LOD_{95\%}$ values are comparable for all the time intervals investigated (2018-2019, 2017-2019 and 2016-2019).

year	**GCP**					
	RMSE xy (cm)	**RMSE z (cm)**	**Total RMSE (cm)**	**ME | STDEV x (cm)**	**ME | STDEV y (cm)**	**ME | STDEV z (cm)**
2016	3.36	2.49	4.18	0.31 | 1.95	-0.72 | 2.81	0.27 | 2.60
2017	2.46	2.87	3.78	-0.56 | 1.60	0.23 | 1.93	-0.34 | 2.98
2018	2.48	3.07	3.94	0.03 | 1.50	-0.002 | 2.11	-0.08 | 3.20
2019	2.26	1.45	2.69	-0.27 | 1.90	0.11 | 1.37	-0.07 | 1.51
	CP					
	RMSE xy (cm)	**RMSE z (cm)**	**Total RMSE (cm)**	**ME | STDEV x (cm)**	**ME | STDEV y (cm)**	**ME | STDEV z (cm)**
2016	3.31	4.06	5.24	0.06 | 2.62	0.03 | 2.51	-1.16 | 4.26
2017	2.26	4.10	4.68	0.84 | 1.71	-0.40 | 1.38	-0.68 | 4.33
2018	2.72	8.94	9.34	-0.03 | 1.32	-0.09 | 2.60	3.79 | 8.65
2019	1.76	3.04	3.51	-0.15 | 1.56	0.11 | 1.08	0.33 | 3.26

	Time interval	**Registration error (cm)**	**$LOD_{95\%}$ (cm)**
Rock glacier (I + II + III + IV)	2016-2019	6.31	16
	2017-2019	5.85	14
	2018-2019	9.98	22

Table 2. Root mean square error (RMSE), mean error (ME) and standard deviation (STDEV) for both GCP and CP. Registration error and level of detection threshold for each time interval investigated.

The mean and standard deviation of the errors computed on stable points for pairs of acquisitions are reported in Table 3.

Time interval	ME | STDEV x (cm)	ME | STDEV y (cm)	ME | STDEV z (cm)
2016-2019	-2.10 | 5.80	3.90 | 5.50	-6.40 | 7.20
2017-2019	-0.60 | 6.51	2.18 | 5.24	-10.30 | 12.33
2018-2019	-1.12 | 4.55	2.81 | 5.11	-6.68 | 9.51

Table 3. Mean (ME) and standard deviations (STDEV) of the horizontal and vertical error for stable ground points.

The mean horizontal and vertical errors over the three time intervals are within the order of -2.10 and 3.90 cm (stdev ranges 4.55-6.51) and between -10.30 and -6.40 cm (stdev ranges 7.20-12.33), respectively.

The uncertainty of image coregistration was also quantified on four profiles located on the stable terrain outside the rock glacier (Fig. 3). The mean differences between each DSM (2016, 2017, 2018) and the reference DSM (2019) range between -0.32 m and 0.05 m. The lowest differences in elevation are found between the DSMs of the years 2016 and 2018 (especially for the P1, P3 and P4 profiles), while the DSM differences are slightly higher for the year 2017, particularly in the P1 profile. We should consider that, although these profiles are located on areas considered stable, the microtopography of the zone could have been altered by weathering or snow cover during the investigated period.

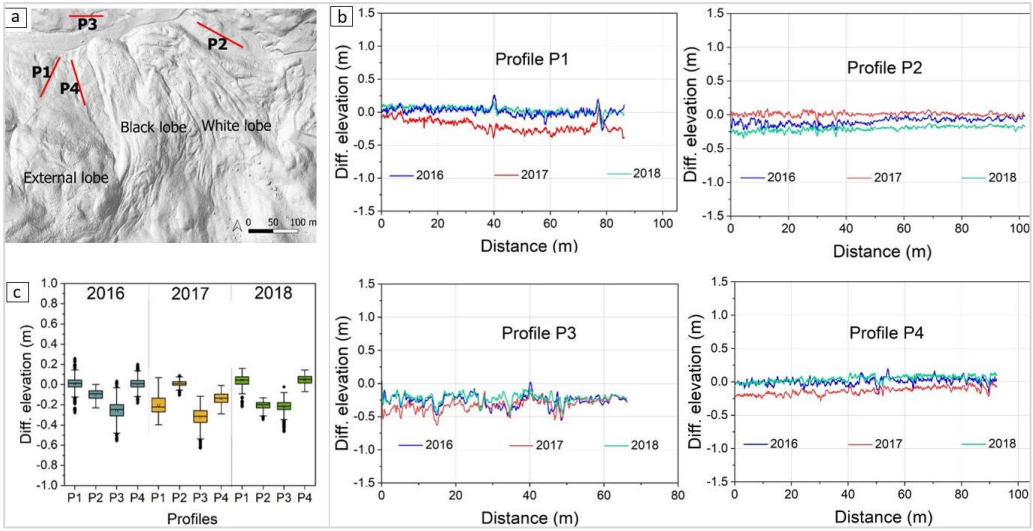

Figure 3. (a) Hillshade of the reference DSM acquired in 2019 and location of four profiles in stable terrain used for the assessment of the coregistration accuracy; (b) Differences in elevation between the DSMs of the years 2016, 2017 and 2018 and the reference year (DSM of the year 2019) for each profile; (c) Boxplot of Z values for P1, P2, P3 and P4 for the time interval investigated.

Convex (dome) and concave (bowl) deformations are evaluated to exclude systematic vertical errors, which could affect the UAV-SfM derived products. The dome/bowl deformations are shown in Fig. 4 and the estimated dome/bowl sizes are reported below, in Table 4.

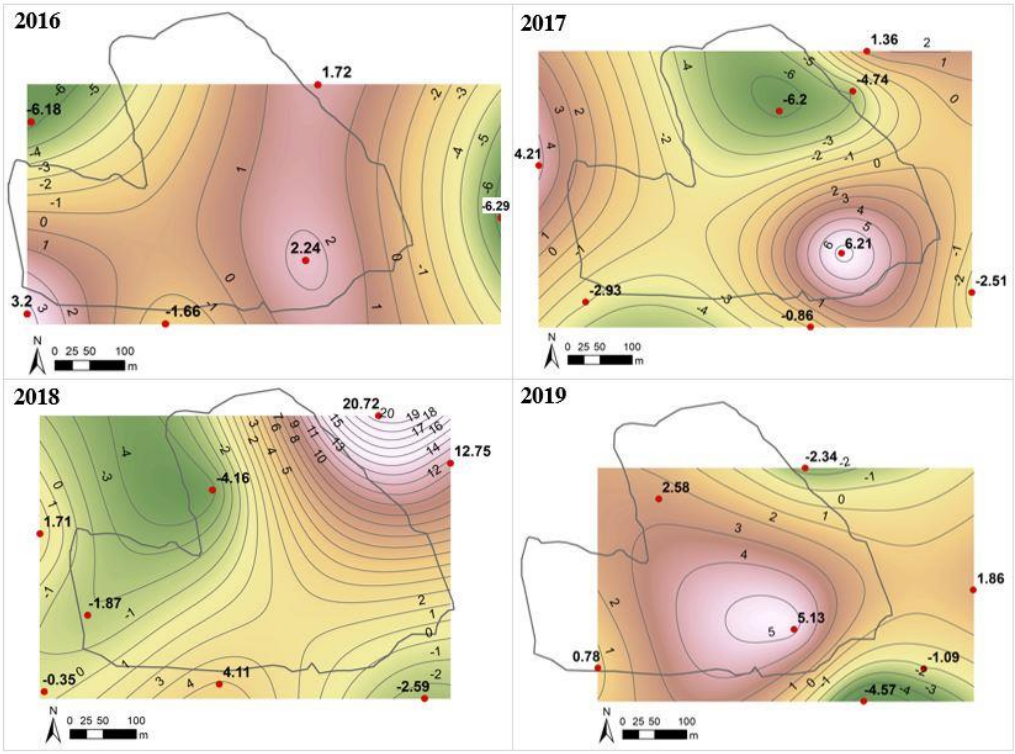

Figure 4. Graphical representation of dome/bowl errors in 2016, 2017, 2018 and 2019 with rock glacier outline in black line. Contour values and scale expressed in centimetres.

Year	Dome/bowl size (cm)
2016	4.12
2017	-2.00
2018	-2.77
2019	4.00

Table 4. Dome/bowl size [cm] for the years 2016, 2017, 2018 and 2019.

2.4.3 3D surface changes

The description of the surface changes of the Gran Sometta rock glacier is based on the products derived from dense cloud-to-cloud comparison.

As shown in Table 5, for the three intervals (2018-2019, 2017-2019 and 2016-2019) the significative surface change areas (i.e. areas statistically significant at 95% confidence) increase as the time interval increases, spanning from 14% to 44% of the rock glacier area.

The statistically significant surface changes are mostly negative, between 65 and 68%. Only for the 2018-2019 comparison there is a predominance of positive (52%) over negative (48%) changes.

Time interval	Areas of significant surface changes (%)	Mean significant surface change (m)	Areas of positive surface changes (%)	Areas of negative surface changes (%)	Mean positive surface changes (m)	Mean negative surface changes (m)
2016-2019	44	-0.03	35	65	0.73	-0.44
2017-2019	36	-0.11	32	68	0.47	-0.38
2018-2019	14	0.07	52	48	0.48	-0.39

Table 5. Percentage of areas and absolute mean significant surface changes reported for the investigated time intervals. These variations were divided into positive and negative significant areas (with associated percentages and absolute mean values) for material gain and material loss, respectively.

In Fig. 5, we present the rock glacier areas characterized by significant changes between 2016 and 2019, generated by comparing point clouds via the M3C2 plug-in.

Positive and mostly negative distinct longitudinal and transverse distance changes occur on the main part of the rock glacier as a result of advancing ridges and furrows. The alternating spatial pattern of mass gains and losses mostly indicates a downslope propagation of material from the upper zones of the rock glacier. Accumulation processes are less frequent and occur mostly in the frontal lobes and less in the ridge and furrow systems. The upper part (sector IV) of the rock glacier shows non-significant variations in accordance with the almost stable behaviour of the sector over time (i.e., minimal displacements, and negligible morphological changes).

Considering the 2016-2019 range, the areas with significant changes cover 45% of the external lobe, 31% of the black lobe, 23% of the white lobe and only 1% in the upper part where there is no subsurface ice. Negative changes dominate in all sectors with the exception of the lowest parts of the external and black lobes where continued advance of the creeping frozen ground is documented.

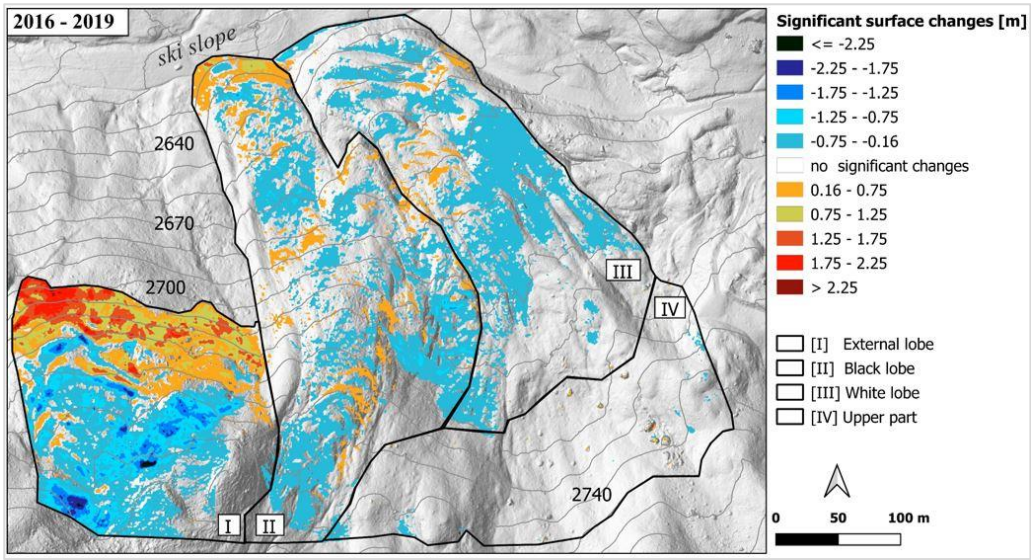

Figure 5. Rock glacier areas characterized by significant changes between 2016 and 2019, generated by 3D point cloud comparison with the M3C2 plug-in.

At the front of the external lobe (sector I), the positive surface change values are above 0.75 m, with the largest variations in the westernmost part. The upstream negative changes reached values greater than -0.75 m. Less intense surface changes characterise the black (sector II) and white (sector III) lobes. Alternate positive and negative changes up to 0.75 m occur in the furrow and ridge areas (especially in the upper part of sector II). Considering only the statistically significant surface changes in the period 2016-2019, the negative changes correspond almost to the totality (89%) of the changes estimated on the white lobe, to the 68% on the black lobe and 51% of the external lobe. The upper part (sector IV) is not considered since the percentage of significant areas is lower than 1%.

Differences between rock glacier sectors are further analysed on an annual basis using the empirical cumulative distribution function - ECDF (Fig. 6), by subtracting products derived from the M3C2 distance map. The line referring to the zero of M3C2 distance on the x-axis (unrealistic condition in which no change

occurs) intercepting the ECDF curves defines the percentage of area points subject to real negative vertical changes (negative M3C2 values). The remaining percentage corresponds to the positive vertical changes, the intensity of which is represented by the part of ECDF curves to the right of the straight line.

The external lobe (Fig. 6a) is subject to slightly positive changes in the 2016-2017 and 2018-2019 periods whereas a net predominant negative surface change (~ 70% of the area) occurs in 2017-2018. A similar tendency is observed for the black lobe (Fig. 6b) where major negative changes occur again in 2017-2018, with changes affecting 80% of the area. Similar trends are observed in the 2016-2017 and 2018-2019 periods, with a slight predominance of positive changes (~ 51%). Considering the white lobe (Fig. 6c), negative changes predominate in all years, above 60% for the 2016-2017 and 2018-2019 periods and about 55% in 2017-2019.

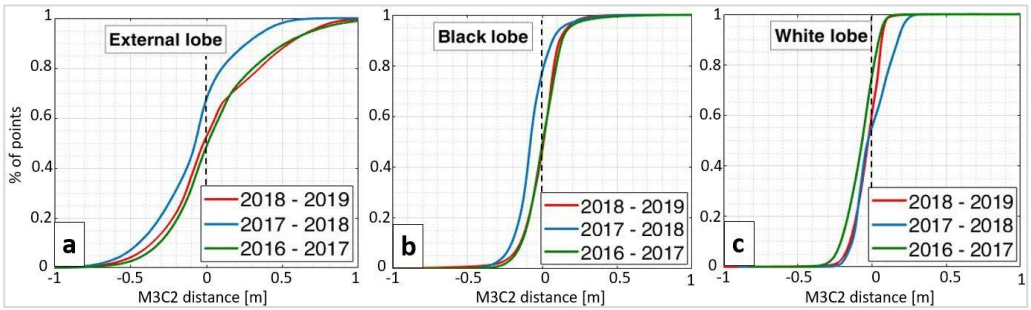

Figure 6. Annual empirical cumulative distribution functions (ECDF) for the three main sectors of the rock glacier (see Fig. 1c), elaborated from the M3C2 distance products: (a) external lobe; (b) black lobe; (c) white lobe.

2.4.4 Analysis of displacement vectors

The horizontal surface velocities were computed using the automatic IMCORR feature-tracking algorithm. These results were then compared against repeated GNSS measurements, considered here as a reference.

The velocity patterns generated with the image correlation algorithm and referring to the period 2016-2019 are represented in Fig. 7a together with the

displacements detected by the GNSS measurements. Maximum displacements in the westernmost part of the external lobe (exceeding 6 m) and minimum in the upper part (sector IV) with displacements less than 0.3 m. The black lobe (sector II) is characterized by greater displacements (maximum values in the central-low part) compared to the adjacent white lobe (sector III), which has average displacements of less than 1.5 m.

A further evaluation of the surface displacement field was performed based on repeated GNSS campaigns performed on 54 points distributed over the rock glacier (Fig. 1c). The interannual surface velocity (Fig. 7b) was estimated between 2012 and 2020 for the black (sector II) and white (sector III) lobes and from 2015 to 2020 for the external lobe (sector I). An increase in interannual surface velocity of the rock glacier between 2013 and 2015 can be observed, from a maximum of around 1.1 m/y for the black lobe in 2013 to an average value of more than 1.4 m/y in 2015. Between 2015 and 2018, the velocity decreased compared to the surface velocities recorded in the period 2013-2015. From 2018,

flow velocity increased again until 2020 with maximum values of 0.4 m/y (white lobe), 1.3 m/y (black lobe) and 1.9 m/y (external lobe).

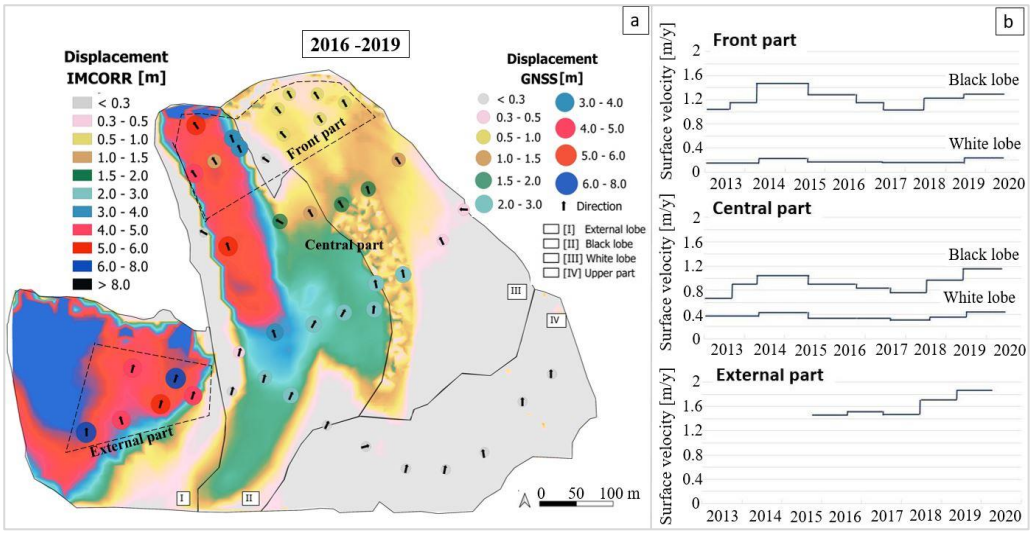

Figure 7. (a) Horizontal displacement magnitudes derived from IMCORR image correlation algorithm and GNSS measurements within the period 2016-2019. (b) Annual horizontal surface velocities of different sectors of the rock glacier computed as the mean of the GNSS measurements in each sector shown in (a).

The horizontal displacements measured at the marker points by GNSS were compared to the horizontal displacements derived by IMCORR image correlation algorithm from UAV data (Fig. 8). The results from the image correlation algorithm are well related to GNSS measurements with an $R^2 = 0.99$ and RMSE = 0.05-0.07 m/y.

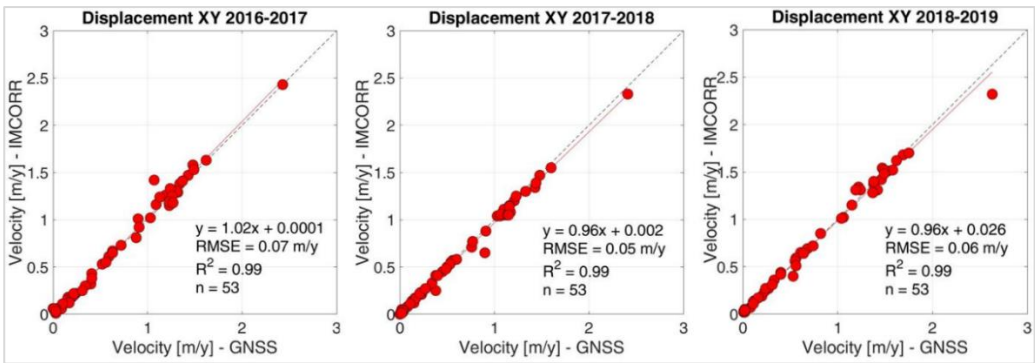

Figure 8. Scatterplots between displacements obtained by image correlation algorithm and GNSS measurements.

2.4.5 Surface elevation changes

Two approaches are adopted to map and quantify the surface elevation changes of the rock glacier, i.e. the classic difference of DSMs (DoD) and the Nz component, which is one of the products (together with Nx and Ny components) resulting from the decomposition of the M3C2 distance map.

The DoD and Nz maps provide the spatial distribution of topographic vertical changes through time. Decreases and increases in elevation are shown as negative and positive values, respectively. DoD shows a mean ± standard deviation equal of -0.05 ± 0.4 m while for the Nz component is -0.07 ± 0.3 m. The spatial patterns observed in the DoD map are similar to those described in the Nz map even if in the first case more features are highlighted by more pronounced vertical changes. This difference is due to the M3C2 algorithm that tracks 3D variations in surface orientation with respect to the changes in the z direction only computed by classic DoD approach. This is observed both in the white lobe and in the black lobe, at around 2680 m. a.s.l. Here, less changes in elevation are mapped indicating that the z-component is not the main one in that sector for the period 2016-2019 where instead horizontal ones predominate. Fig. 9 shows the comparison between maps of DoD and Nz component in the 2016-2019 period.

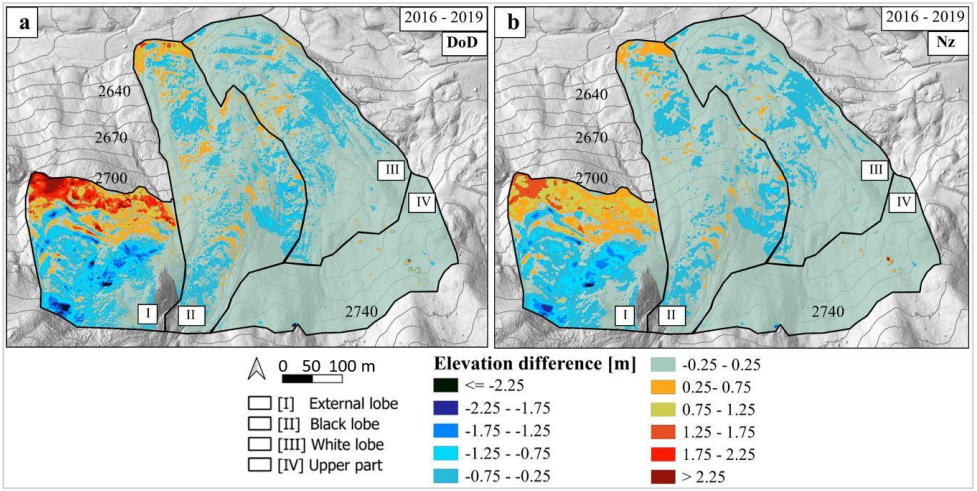

Figure 9. (a) Vertical differences obtained through DSM differencing (DoD) and (b) dense point cloud comparison, considering the vertical component of the normal surface in the reference point cloud (Nz). The time investigated covers the period from August 2016 to August 2019. The hillshade refers to the year 2016.

2.4.6 Interannual variability of GST measurements and meteorological data

Parameters derived from GST measurements (Fig. 1c for locations) as the MAGST, the GFI, the GTI and the WEqT as well as the duration of snowmelt period and mean air temperature (mean T_{air}) are shown in Table 6.

MAGST varies between 0.70 °C and 2.04 °C, with values higher than 1.6 °C in years when an increase in horizontal surface velocity is observed, 2014-2015, 2018-2019 and 2019-2020. While the GTI does not exhibit a clear relation with the rock glacier kinematics, GFI conditions above -0.6 °C are associated to an increase in surface velocities whereas colder GFI results in a decrease in surface displacements as between 2015 and 2018. The WEqT varies between -1.18 °C and -1.96 °C with values higher than -1.4 °C in years with increased surface velocities and values lower than -1.7 °C in years characterized by a deceleration (2015-2016, 2016-2017 and 2017-2018). Thus, changes in surface displacement rates in the period 2014-2020 can be interpreted to be caused by variations in

GST-based parameters, while the snowmelt period and T_{air} do not seem to directly affect rock glacier creep rate.

Year	MAGST [°C]	GFI [°C]	GTI [°C]	WEqT [°C]	Mean T_{air} [°C]	Snowmelt period [start-end]
2014-2015 (*)	2.04	-0.34	2.12 (2015)	-1.24 (2015)	6.23 (2015)	22 April – 16 June (2015)
2015-2016	0.70	-1.07	1.90 (2016)	-1.96 (2016)	6.29 (2016)	12 May – 26 June (2016)
2016-2017	1.36	-0.76	2.07 (2017)	-1.83 (2017)	6.15 (2017)	13 April – 17 June (2017)
2017-2018	0.80	-1.12	2.22 (2018)	-1.77 (2018)	6.88 (2018)	24 April – 28 June (2018)
2018-2019	1.68	-0.52	2.10 (2019)	-1.18 (2019)	6.79 (2019)	24 May – 30 June (2019)
2019-2020 (*)	1.91	-0.30	/	-1.40 (2020)	/	19 April – 26 June (2020)

Table 6. MAGST (Mean Annual Surface Temperature); GFI (Ground Freezing Index); GTI (Ground Thawing Index); WEqT (Winter Equilibrium Temperature); mean air temperature (mean T_{air}) from June to September; duration of snowmelt period [start of snowmelt and snow free date]. Period from 2014 to 2020. The asterisk (*) indicates the years of largest rock glacier creep velocity.

2.5 Discussion

The multi-temporal kinematic of the Gran Sometta rock glacier surface was analysed through four UAV campaigns (2016–2019) and annual GNSS surveys from 2012 to 2020 and discussed hereafter considering the ERT tomograms and GST data.

2.5.1 Accuracy of UAV products and error analysis

Precise and well-distributed GCPs are key for obtaining accurate UAV products, since they provide constraints within the bundle adjustment (Sanz-Ablanedo et al., 2020; James and Robson, 2014). In the Gran Sometta, the use of numerous and well-distributed GCPs whose coordinates were measured with high precision (i.e., with a fixed GNSS/RTK technique maintaining fixed the GPS base station on known position at the rock glacier front for all the flights),

allowed to improve camera self-calibration and reduce the magnitude of systematic errors.

The mean horizontal and vertical errors computed on stable features over the three time intervals investigated (2016-2019, 2017-2019 and 2018-2019) vary between 2.10 and 3.90 cm (stdev ranges 4.55-6.51) and between -10.30 and -6.40 cm (stdev ranges 7.20-12.33), respectively. The biggest errors are found on the vertical component. These results are in line with previous studies following similar methodologies as the one in our study, such as, for example Bodin et al. (2018) on the Laurichard rock glacier. Their mean vertical differences between successive pairs of DSMs in stable points around the rock glacier are 3 cm (in 2005-2006 and 2012-2013 time intervals) and 18 cm (in 2013-2015). In a stable area presumed unchanged, Durik et al. (2014) estimated a standard deviation of vertical error (± 15 cm between 2006 and 2012) comparable to those found in our case.

We would like to point out that although these errors were calculated for features that were considered stable, the microtopography of the considered features could have been altered by weathering or snow cover during the investigated period. For this reason, we found that the average vertical and horizontal errors may not be exactly 0 m. This uncertainty is reduced when CP are considered for the assessment of the accuracy of the UAV products because the CP coordinates were measured simultaneously to each UAV survey with fixed GNSS/RTK technique.

The presence of systematic vertical errors may result in deformations in the UAV-derived products, as bowling or doming effects (Sanz-Ablanedo et al., 2020). Dome/bowl deformations sizes observed in our dataset are comparable to those found by Sanz-Ablanedo et al., (2020) that detected dome size of 0.02 m using all GCPs. Our dome/bowl size are small to those found by James and

Robson (2014) with domed deformation of about 0.2 m over horizontal distances of around 100 m, in absence of control measurements.

2.5.2 Level of detection assessment and 3D geomorphological activity quantification

In this study, beside the difference between DSMs, a point cloud-based distance calculation algorithm is applied, and 3D surface changes are quantified on pairs of UAV acquisitions. Moreover, the ability of the 3D change analysis to reliably quantify topographic changes is assessed by statistically evaluating the confidence interval of the estimated distance, also referred to as the level of detection (LOD) at 95%, for each of the multi-temporal pair of acquisitions. We compared our $LOD_{95\%}$ values with those found by Zahs et al. (2019) and Bollmann et al. (2012) on other rock glaciers. For an annual interval, the $LOD_{95\%}$ of surface changes quantified by Zahs et al. (2019) is 9 cm and more than 30 cm in Bollmann et al. (2012), while in our case the $LOD_{95\%}$ value is 22 cm. However, it should be noted that both Zahs et al. (2019) and Bollmann et al. (2012) used multi-temporal Airborne Laser Scanning (ALS) point clouds in their studies. Furthermore, Zahs et al. (2019) missed an independent evaluation of the geometric accuracy of the ALS products, hampering a proper comparison with the results obtained in this work.

For the 2018-2019, 2017-2019 and 2016-2019 intervals the areas of the rock glacier with significative surface change increase with the time interval, spanning from 14% in one year, to 36% in two years and to 44% in three years.

Surface elevation changes estimated with DoD and through the decomposition of the M3C2 distance map to obtain its vertical component (Nz) show similar spatial patterns (see Figs. 9a and 9b) even if in the latter case few features with less pronounced vertical changes are highlighted. A clear example concerns the white and black lobes in which it is possible to highlight a portion where fewer

vertical changes are detected. This indicates that in this area and for the time interval under consideration, the z component of the displacements is secondary to the predominant horizontal one. This depends on the M3C2 algorithm which computes the local distance between two point clouds along the normal surface direction which tracks 3D variations in surface orientation (Lague et al., 2013) and not only with respect to the z direction as in the classic DoD approach. Moreover, compared to DoD, the M3C2 algorithm operates directly on point clouds without meshing or gridding, and thus, reduces the uncertainty related to missing data and interpolation errors. These errors can be particularly relevant in landscapes characterized by rough morphology, such as rock glaciers, since the DSM decreases information density proportionally to surface steepness (Zahs et al., 2019). To confirm this, the overall greatest difference between the methods is found in the sector with the highest slope gradient, i.e. in the external lobe (~ 27°), and less pronounced changes in the white lobe, which is characterized by a 20° slope gradient. Furthermore, we recorded the maximum velocities in the steeper sector (external lobe), while in the white lobe, with the lowest average slope, we observed the smallest velocity range. Spatial patterns of rock glacier properties and dynamics can be explained by several factors (Cicoira et al., 2021; Müller et al., 2016; Bodin et al., 2018). Combining a model for calculating rock glaciers thickness with an empirical model of ice-rich debris creep, Cicoira et al. (2021) derived a Bulk Creep Coefficient (BCF) which allows to explain the contribution of material properties and geometry to surface velocities. For dynamically non-destabilized rock glaciers, Cicoira et al. (2021) shows that the geometry seems to demonstrate spatial variability of flow rates with almost constant rheological properties of the debris. Müller et al. (2016) analysed two rock glaciers in the Swiss Alps and observed that the steeper rock glacier showed flow velocities (0.75-1.55 m/y) higher than the gentler rock glacier (0.06-0.13 m/y). Analysing the entire profile of the Laurichard rock glacier, in the French

Alps, Bodin et al. (2018) did not find a clear control of slope on surface velocity but, considering only a limited sector of it, they detected a significant relationship between rock glacier velocity and slope gradient higher than 20°.

2.5.3 Interannual velocity variations

Time series of rock glacier movement in the European Alps indicate an acceleration in permafrost creep in recent decades in relation to an increase in permafrost temperatures and water content (Kenner et al., 2019). Although changes in ice properties due to permafrost degradation appear to significantly influence rock glacier kinematics, the factor that may trigger rock glacier destabilisation remains a source of debate (Vivero & Lambiel, 2019).

Annual surveys conducted at several rock glaciers in the European Alps suggest an increase in mean surface velocity of +52% during the 2010-2014 period with most of them reaching maxima in 2014 (PERMOS, 2016; Delaloye et al., 2013). A new maximum velocity peak was reached in 2015, followed by a progressive decrease of the creep velocities until 2017-2018, with an average reduction of surface velocities of -28% in the Swiss Alps (PERMOS, 2019). A new gradual increase in surface movement rates is observed since 2018. Considering the period 2012-2020, the interannual flow velocity of the Gran Sometta rock glacier shows a trend similar to the one descried by PERMOS. The maximum surface velocity was reached in 2015, followed by a decrease until 2017-2018 in which the minimum average values of 0.2 m/y for the white lobe, 0.75 m/y for black lobe and 1.5 m/y for the external lobe were detected. A gradual increase in horizontal surface velocity has been observed since 2018 with peak values of 0.4 m/y, 1.2 m/y and 1.9 m/y for the white, black, and external lobes respectively, in 2020.

In this study, different methods for the estimation of rock glacier velocities were applied. Displacement vectors from GNSS measurements provide accurate

information but are limited to 54 points on the rock glacier surface. On the other hand, the displacement vectors derived from UAV surveys allowed a better characterization of the spatial variability of rock glacier displacements. The image correlation algorithm allows the generation of velocity maps on a regular spatial grid, allowing the identification of areas moving at different velocities. The results from the image correlation algorithm are well related to GNSS measurements with R^2 equal to 0.99 and RMSE between 0.05 m/y and 0.07 m/y.

2.5.4 ERT interpretation and permafrost characteristics

Several studies highlighted that the spatial patterns of rock glacier dynamics are largely controlled by the internal structure and by the thickness, ice content and temperature of the frozen body (Cicoira et al., 2021; Fey et al., 2020; Cicoira et al. 2019; Kenner et al., 2019). The viscous flow patterns of the rock glacier are due to the presence of a thick and continuous perennially frozen layer supersaturated with ice (Haeberli and Vonder Mühll, 1996). The Gran Sometta rock glacier reveals a complex dynamics linked to the heterogeneous distribution of perennially frozen debris rich in ice and thick enough (about 20-30 metres) for permafrost creep to occur. Along the white lobe (GRS-LW), the upper part of the profile, interpreted as unfrozen from the ERT results, corresponds to a sector where no movements are detected by cloud-to-cloud and image correlation algorithm. The absence of any significant movement in the upper part (sector IV) is related to the lack of permafrost in this area probably related to the development and advance of a small glacier, not heavily charged with debris, during the Little Ice Age. The unfrozen layer may be indicative of (i) degradation of former permafrost by a temperate small LIA glacier or (ii) mechanical effect of the LIA glacier that pushed the permafrost to unfavourable positions to its preservation (Delaloye and Lambiel, 2008). However, in the central and lower part of this profile, we identified the presence of two distinct frozen ground

bodies, with a thickness of around 30 m and 20 m for the upper and the lower one, respectively. An increase in surface horizontal velocity is observed in this zone. Additionally, the slower eastern part is not only gentler, but it also largely corresponds to currently degrading permafrost, where a thaw induced subsidence of up to 5 cm/y is observed.

A different situation is found for the slightly faster moving black lobe, where a continuous perennially ice-rich frozen ground body with a thickness of approximately 20 m is detected over most of the profile length (GRS-LB). The occurrence of subsurface frozen sediments, without any massive ice layer close to the surface, corresponds to the zone not covered by a glacier during the LIA (Delaloye and Lambiel, 2008). The creep behaviour of subsurface ice-rich frozen layers depends mainly on the ice content and on the size of the grains that constitute the debris material (Cicoira et al., 2021). Imposed stresses and deformations in active rock glaciers affect the microscopic structure of the ice-debris mixture involved (Haeberli and Vonder Mühll, 1996). Hence, we suggest that the different velocities recorded at the two lobes stem hereby from the heterogeneous distribution of frozen ground, as visualized by the geophysical measurements.

Borehole data (provided by the Environmental Protection Agency of Valle d'Aosta but not shown here) show that the entire active layer is freezing each winter. However, the ice-rich perennially frozen debris documented by the ERT profiles are close to thawing conditions. The investigated permafrost is undergoing a degradation phase, like probably most permafrost occurrences in the Alps and comparable mountain environments and appears to be in strong imbalance with the current climatic conditions. Overall, the structure and thermal state of frozen ground at depth, but also the topographical settings appear as the main factors explaining the current flow patterns of the Gran Sometta rock glacier. On the contrary, the high interannual variations of creep rates in

perennially frozen debris of rock glacier are likely to be related to external climatic factors rather than to local internal characteristics of the rock glacier permafrost.

2.5.5 Permafrost thermal regime

Recent studies showed that annual variations in rock glacier surface velocities can be related to GST variations. GST variations reflect, with a delay of several months, the variations of the temperature of the upper permafrost layers due to the slow propagation of annual surface thermal anomalies deeper into the permafrost (Staub et al., 2016; Delaloye et al., 2010). Several studies showed that the surface thermal signal can usually penetrate to permafrost layers located at 10-30 m depth (Staub et al., 2016; Delaloye et al., 2010). Interannual surface velocity variations have been shown to follow an exponential relation with multiannual GST forcing (Staub et al., 2016), as in the case of the Becs-de-Bosson rock glacier (in the Valais Alps) where most of the inter-annual velocity variations during one decade were related to temperature changes at 10-30 m depth. On the Dösen rock glacier (central Austria), Kellerer-Pirklbauer and Kaufmann (2012) observed that a reduction by 50% of the freezing-degree days at one meter depth causes a velocity increase by 1.5 times.

The active layer temperatures are influenced by the multi-annual mean annual air temperature (MAAT) trend. The increase in MAAT may delay the freezing of the active layer, produce early melting of spring snow, and consequently promote a rapid acceleration of creep rates (Kenner et al., 2019; Bonnaventure and Lamoureux, 2013). In addition, the relationship between snow cover and permafrost creep rates indicates a long-term delay in surface velocity caused by snow melting and water percolation into the perennially frozen material and storage of water for weeks to months favouring faster creep movement within the rock glacier with a significant time lag (Kenner et al., 2019). Kellerer-Pirklbauer

et al (2017) show that over the period 2007-2015 a significant permafrost warming inside a rock glacier body caused an acceleration of surface flow velocity over the last two decades.

The comparison with air temperature data revealed a time lag of one to more years for acceleration caused by warm air temperatures (Kellerer-Pirklbauer and Kaufmann, 2012). In contrast, strong cooling causes a slightly faster deceleration possibly related to the reduced availability of liquid water within the rock glacier. These observations show that warmer air temperature, warmer GST, and warmer permafrost temperature favour creep acceleration. Long periods of warm surface conditions cause rising permafrost temperature and accelerated creep rates in rock glacier permafrost. The snow cover and its onset in early winter have a greater influence on the heat and energy exchange at the ground surface than air temperatures whose effect is limited to the snow-free period (Staub et al., 2016; Kenner et al., 2019).

In our study, the observations over a short-term period (2014-2020) suggest that the increase in creep rates of rock glacier permafrost depends on the ground thermal regime and on the related permafrost warming rather than directly on air temperatures, and timing and duration of snow melt period. A MAGST value higher than 1.6°C is found as a recurring parameter in years when an increase in horizontal surface velocity is observed (2014-2015, 2018-2019 and 2019-2020). While the GTI does not seem to play a role on the observed rock glacier creep rate variations, GFI values seems to be related to the observed kinematic responses. Indeed, years with GFI conditions above -0.6°C are characterised by an increment of surface velocities, while lower GFI results in a decrease in surface displacements. Increase and decrease in surface velocities generally correspond to WEqT values greater than -1.4°C and lower than -1.7°C, respectively. Thus, we hypothesized that the increase in horizontal velocities of the investigated rock glacier (2014-2015, 2018-2019 and 2019-2020) can be

related to warm surface conditions. In fact, the highest measured values of MAGST (> 1.6°C), GFI (> -0.6°C), and WEqT (> -1.4°C) correspond to an acceleration phase of creep within the rock glacier permafrost. Inversely, ground cooling causes a slight deceleration of creep rates as in the period from 2015 to 2018 where the MAGST, the GFI and the WEqT are slightly lower (< 0.7°C, < -0.8°C and < -1.8°C respectively) than in the acceleration phase.

The present study illustrates that permafrost continues to exist also when local glaciers have long disappeared. Rock glaciers with their debris cover are usually more resilient and respond to climate change on relatively longer time scales than glaciers (Haeberli et al., 2006), which with their evolution are considered excellent climate change indicators. This is due to the fact that the characteristic range of permafrost thaw rates is by one to two orders of magnitude lower than present-day melt rates of glaciers. With the current warming rate (temperatures have risen by 2°C in the European Alps over the 20th century, Gobiet et al., 2014), a century will may be enough for a complete thaw of the investigated permafrost at Gran Sometta rock glacier. With positive mean annual surface temperatures and presumably accelerated future atmospheric warming, many other rock glaciers may suffer the same fate as observed on the Gran Sometta.

2.6 Conclusions

This work enabled the quantification and interpretation of the kinematics of the Gran Sometta rock glacier permafrost and its downstream movement using multi-temporal UAV acquisitions, GNSS surveys, geophysical prospections, and GST measurements. UAV acquisitions allowed the characterization of the spatial distribution of surface displacements even in inaccessible site as opposed to GNSS surveys which provide high accurate information but limited on a few selected points on the surface. The M3C2 distance calculation algorithm is a valid tool to calculate mass transport processes with complex geomorphology and it

was successfully adapted to quantify the surface normal thickness changes of the Gran Sometta rock glacier.

The interannual changes in creep rates of the rock glacier permafrost are in agreement with the trend observed in other Alpine rock glaciers. Considering 2012-2020, maximum peak surface velocities were reached in 2015, followed by a velocity decrease until 2017-2018 but the following two years (2018-2019 and 2019-2020) are marked by a gradual increase in surface velocity.

Processes of freezing and melting of the permafrost are influenced by a complex function of both rock glacier flow dynamics and ground thermal conditions. At Gran Sometta, the heterogeneous distribution of frozen ground occurrence at depth, its structure, and the topographical settings seem to be key factors explaining the observed spatial flow pattern. Annual kinematics are related to the ground thermal regime, as evinced by the MAGST, GFI and WEqT values. Increases in permafrost creep rates (in 2014-2015, 2018-2019 and 2019-2020) respond to higher MAGST values while a deceleration phase occurred with lower MAGST values as in 2015-2016, 2016-2017 and 2017-2018. Also, GFI and WEqT values higher than -0.6°C and -1.4°C, respectively, generally correspond to high surface displacement rates. The subsurface ice documented by ERT profiles is close to melting conditions and the investigated permafrost appears to be in imbalance with the current climatic conditions. The observed rates of thaw subsidence at the margins of the rock glacier active part, in the range of centimetres per year, are characteristic for ice-rich permafrost within rock glacier landforms.

3 FLOW VELOCITY VARIATIONS AND SURFACE CHANGE OF THE DESTABILISED PLATOR ROCK GLACIER (CENTRAL ITALIAN ALPS) FROM AERIAL SURVEYS

The content of this chapter is published in Remote Sensing as: Bearzot F., Garzonio R., Colombo R., Crosta G.B., Di Mauro B., Fioletti M., Morra Di Cella U., Rossini M. "Flow velocity variations and surface change of the destabilised Plator rock glacier (Central Italian Alps) from aerial surveys". Remote Sens. 2022, 14, 635. https://doi.org/10.3390.rs14030635

Abstract

Flow velocities were measured on the Plator rock glacier in the Central Italian Alps using a correlation image analysis algorithm on orthophotos acquired by drones between the years 2016 and 2020. The spatial patterns of surface creep were then compared to the Bulk Creep Factor (BCF) spatial variability to interpret the rock glacier dynamics as a function of material properties and geometry. The rock glacier showed different creep rates in the rooting zone (0.40-0.90 m/y) and in the frontal zone (> 4.0 m/y). Close to the rock glacier front, the BCF assumed the highest values, reaching values typical of rock glaciers experiencing destabilisation. Conversely, in the rooting zone the small rates corresponded to lowest BCFs, about five times smaller than in the frontal zone.

The Plator rock glacier revealed a substantial advancement from 1981 to 2020 and distinct geomorphological features typical of rock glacier exhibiting destabilising processes. Given the fast-moving phase, the advancement of both the front line and the front toe of the rock glacier, and the contrasting spatial distribution in the BCFs, the Plator could be considered a destabilised rock glacier.

3.1 Introduction

Rock glaciers are landforms that form as a result of creeping mountain permafrost (Müller et al., 2016; Haeberli et al.; 2006). In recent years, the study of rock glacier dynamics and their coupling to the changing climate system is receiving increasing attention (Hartl et al., 2016; Delaloye et al., 2010).

Since the 1990s, acceleration of rock glacier displacements has been documented in the European Alps. Thermo-hydro-mechanical coupling associated with the transitory availability of liquid water content are the main reasons rock glaciers move rapidly. A number of studies have investigated the connection between air and ground temperature and the flow dynamics of rock glaciers (Cicoira et al., 2019a; Seppi et al., 2019; Wirz et al., 2016; Staub et al., 2016), while others have integrated flow information with environmental factors like sediment supply dynamics and landform characteristics (Müller et al., 2016; Frauenfelder et al., 2008; Roer et al., 2008).

In recent decades, time series of rock glacier movement in the European Alps indicate that the acceleration in permafrost creep is strongly related to the availability of liquid water. Increased liquid water content strongly affects the movement of rock glaciers, influenced on various temporal and spatial scales by changes in air and ground temperatures (Bodin et al., 2015; Delaloye et al., 2010). Snowmelt, liquid precipitation, and subsurface water flow result in decreased cohesion between soil/ice particles and/or increased pore pressure (Cicoira et al., 2019b; Ikeda et al., 2008), creating local situations of rock glacier instability and, in specific topographic conditions, may cause natural hazards to Alpine communities (Bodin et al., 2015; Schoeneich et al., 2014). Rock glacier acceleration and destabilisation are most likely connected to the complex combination of positive air temperature anomalies and topographical conditions (Wirz et al., 2016; Staub et al., 2016; Roer et al., 2008). The environmental changes affect the processes of transport, resulting in topographical and

kinematic changes, and the existence of the ice and sediments mixture and its properties play an important role in controlling the rheology of rock glaciers (Müller et al., 2016).

Some studies of rock glacier dynamics concentrate on surface displacements and morphology changes (Bearzot et al., 2022; Kenner et al., 2014; Barsch, 1992) whereas some other on their internal structure (Buchli et al., 2018; Arenson et al., 2002; Ikeda et al., 2008) and liquid water content (Cicoira et al., 2019b), trying to understand the factors that force rock glacier responses across different temporal and spatial scales. Only a few limited studies (Cicoira et al., 2021; Buchli et al., 2018; Müller et al., 2016; Frehner et al., 2015; Arenson et al., 2002) examined the rock glacier dynamics and morphology changes using numerical modelling, physical approaches, and mathematical formulations.

Recently a new approach has been proposed for describing rock glacier dynamics (Cicoira et al., 2021). This method combines a plastic model for rock glacier thickness with an empirical creep model for ice-rich debris. The authors introduced the definition of the Bulk Creep Factor (BCF) to investigate the relationship between rock glacier thickness, surface slope and creep rates. The BCF represents the mechanical properties of the rock glacier material, and it allows to separate the geometrical and the rheological contributions to the velocity component. Therefore, the determination of the BCF allows to discriminate different rock glaciers or analyse different sectors of an individual rock glacier with respect to their rheological properties (Cicoira et al., 2021).

A previous work on the Plator rock glacier (Central Italian Alps, Fraele Valley, Lombardia, Italy) was carried out by Scotti et al., (2017) for the period 1981 until 2012 (Scotti et al., 2017). In that study, automatic tracking was used to estimate the surface displacements over 31 years of the rock glacier which was undergoing a fast-moving phase with mean velocity of 3.73 m/y and 2.97 m/y for the tongue and the front, respectively.

Here, we use repeated drone surveys to analyse the Plator kinematics and surface changes at annual resolution. Morphological modifications and kinematics were evaluated using an automatic image correlation algorithm between the years 2016 and 2020. Spatial patterns of displacements were compared to the spatial variability of the BCF. Results were then compared to those obtained in other rock glaciers in the Alps characterized by different dynamical behaviours.

The objectives of this study is: (i) to estimate the spatial and temporal distribution of the rock glacier displacement velocity, (ii) to highlight surface destabilisation features, (iii) to analyse the rock glacier surface changes and (iv) to test the BCF applicability and interpret its spatial and temporal patterns using only remote sensing data.

3.2 Study area

The Plator rock glacier is a talus-derived tongue-shaped rock glacier located in a tributary valley of the Fraele Valley in the Central Italian Alps (46°30’59.68’’N, 10°16’42.27’’E, Figure 10a). The rock glacier is surrounded by the steep Cime di Plator rock wall, consisting of dolostone of the “Plator-Cristallo formation” belonging to the Austroalpine Ortler nappe (Scotti et al., 2017; Scotti et al., 2013).

In 2020, the rock glacier extended from 2320 to 2590 m a.s.l., with a length and width of 590 m and 120-155 m respectively. The area of the rock glacier was 76850 m^2, with an average slope of 27°. The rock glacier was analysed considering three zones (Figure 10b) identified by Scotti et al. (2017). Zone #3 is located between the front line and scarp #2. Approximatively between 2440 m a.s.l. (scarp #2) and 2485 m a.s.l. (scarp #1), Zone #2 is identified. Zone #1 is the rooting zone of the rock glacier that develops from the upper limit outlined by scarp #1 to 2590 m a.s.l. The grain-size of the surface debris layer ranges from

small angular blocks (5-30 cm) in Zone #2 to large boulders (1-5 m) in Zone #3. A typical morphology of an active rock glacier with tension cracks and transverse furrows and ridges is observed in Zone #2 and Zone #3.

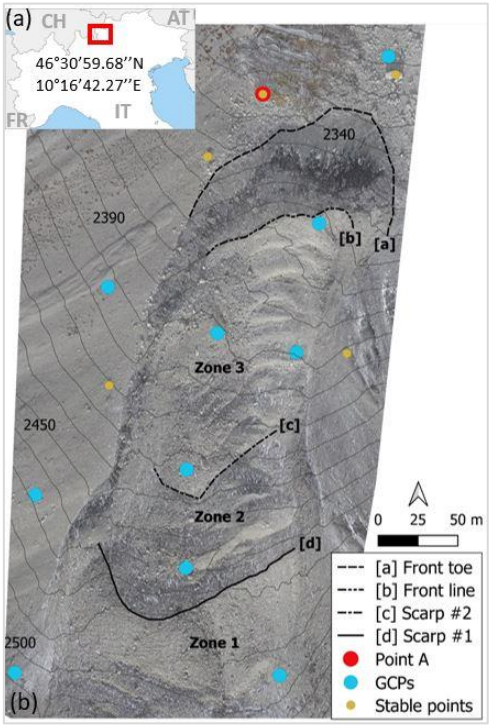

Figure 10. (a) Location of the study site in the Central Italian Alps. The coordinates of the rock glacier site are given in the WGS 84 coordinates system; (b) Orthophoto showing the three zones subdivision, the location of the two scarps [c] and [d], the front line [b] and the front toe [a], the bedrock outcrop and veener in the Point A (i.e., position of GNSS/RTK base station, 2337 m a.s.l.), Ground Control Points (GCPs) distribution and five stable points. Image refers to the year 2016.

3.3 Data and methods

3.3.1 Data acquisition

Four drone surveys were performed on 6th October 2016 with a SenseFly Ebee RTK fixed-wing drone, and on 18th July 2018, 29th July 2019, and on 4th August 2020 using a DJI Phantom 4 PRO equipped with a FC6310 RGB digital camera. Photos were shot from a mean distance of 76-82 m above ground level, 3.5 – 5.0 m/s flight speed (according to light and environmental conditions) and 80% and

75% of front and lateral overlap, respectively. Image resolution (pixels), focal length (mm) and pixel size (µm) were 4896 x 3672 pixels, 4.5 mm for 2016, 5472 x 3078 pixels, 8.8 mm and 2.53 x 2.53 µm for 2018 and 5472 x 3648 pixels, 8.8 mm and 2.41 x 2.41 µm for both 2019 and 2020. Details about the drone campaigns are reported in Table 7.

On the rock glacier area 10 ground control points (GCPs) were evenly distributed (Figure 10b) and their coordinates were measured during drone acquisitions by two GNSS receivers GEOMAX Zenith 35 PRO. The position of the markers was determined using fixed GNSS - Real Time Kinematic (RTK) measurement technique. The base station was positioned at exactly the same location for each drone flight (stable block) in front of the rock glacier (point A in Figure 10b) where its position was determined in post-processing using SPIN 3 GNSS station of BORMIO (BORM).

For the year 2012, the orthophoto provided by the regional topographic agency of Lombardia Region (Italy), with a pixel spacing of 0.5 m, was used in the analysis.

Date	Coverage area (km^2)	Ground resolution (cm/px)	Flying altitude (m above ground level)	Camera model	UAV	N° of images
06.10.2016	0.38	4.19	157	DSC-WX 220	SenseFly Ebee RTK	52
18.07.2018	0.17	2.19	81	FC6310	DJ Phantom 4 PRO	272
29.07.2019	0.18	2.17	82	FC6310	DJ Phantom 4 PRO	207
04.08.2020	0.16	1.92	71	FC6310	DJ Phantom 4 PRO	300

Table 7. Details of the four UAV surveys performed between 2016 until 2020.

3.3.2 Photogrammetric processing

The images collected during each drone survey were processed into orthophotos and Digital Surface Models (DSMs) of the rock glacier and direct surroundings using the Structure-from-Motion (SfM) workflow implemented in the commercial software Agisoft Metashape, v. 1.5.5 (Hendrickx et al., 2019; Goetz et al., 2018; Westoby et al., 2012).

The first step in the processing chain was the selection of photographs with sufficient quality. After importing the images, a sparse 3D point cloud was computed by matching coincident features using an image feature recognition algorithm. Successively, an iterative bundle adjustment algorithm was used to construct the 3D geometry and camera position from a sequence of two-dimensional images acquired from multiple viewpoints, and a sparse 3D point cloud was produced. Subsequently, GCP coordinates were imported, and their positions were manually identified within the images to optimize the spatial accuracy of the 3D point cloud. A multi-view stereo image-matching algorithm was used to increase the density of the point cloud and to convert it by interpolation into DSM and orthophoto was derived from the georeferenced image data using the available DSM. The input parameters used in the photogrammetric processing were applied equally for each of the UAV surveys. DSMs and orthophotos were exported with a ground sampling distance of 0.02 m/pix for each UAV survey.

The Root Mean Square Error (RMSE) and the reprojection error (in pix) were 0.4 cm and 1.2 pix in 2016, 2.0 cm and 0.5 pix in 2018, 3.0 cm and 0.9 pix in 2019 and 2.4 cm and 1.1 pix in 2020.

Five stable ground points outside the rock glacier were used to assess the accuracy of the drone-derived data and the relative kinematic time series. This assessment was done by matching features on stable ground, computing x, y and z shifts for each feature and then mean and standard deviation were derived.

These points were located in stable areas outside the rock glacier, i.e. on lateral talus slopes and on the bedrock outcrop and veneer (close to the Point A, see Figure 10b), to also perform a coregistration analysis of each orthophoto and the RMSE were calculated for each time interval investigated.

3.3.3 Determination of horizontal surface velocities

Horizontal surface displacements of the rock glacier were calculated over four time intervals (2012-2016, 2016-2018, 2018-2019 and 2019-2020) using the Correlation Image Analysis System - CIAS (Heid and Kääb, 2012; Kääb and Vollmer, 2000). CIAS has been already successfully used in other studies focusing on rock glacier dynamics (Vivero et al., 2021; Scotti et al., 2017; Klug et al., 2012).

CIAS compares two images acquired over the same area at different times to calculate a measure of surface horizontal displacement, using the Normalized Cross Correlation (NCC) function (Scotti et al., 2017; Debella-Gilo and Kääb, 2011; Kääb, 2002). Via block matching, the correlation algorithm searches a reference section in the image acquired at time 1 (t_1) in a sub-area of the image acquired at time 2 (t_2). The horizontal displacement between the two images was directly given by differences in the central pixel coordinates (Heid and Kääb, 2012; Kääb and Vollmer, 2000; Kääb, 2002).

For each rock glacier zone (Zones #1, #2 and #3), morphological features (e.g., blocks) were manually identified in the first orthoimage and automatically recognised from the algorithm in the second orthoimage by their size, shape, and position of each other and then used to evaluate the displacement values. To account for the diverse displacement values and the varying lengths of the periods, CIAS was run with different parameter combinations regarding the block sizes.

Since the deposition of debris at the rock glacier front toe hinders a clear delineation of the front line, this image correlation analysis was not applied. The front and the toe lines were manually digitised on each orthophoto, and their displacements were measured along the most likely rock glacier flow line at each point.

3.3.4 The Bulk Creep Factor and applicability

The Bulk Creep Factor (BCF) was calculated to investigate the factors controlling the spatial patterns of displacements and to separate the contribution of mechanical properties of the rock glacier material and geometry on the surface velocities (Cicoira et al., 2021).

The BCF is defined as the ratio between observed (C_{obs}) and modelled creep rates and can be calculated as:

$$BCF = C_{obs} \frac{(n+1)}{\dot{\gamma}c} \left(\frac{\tau_{c\theta} + \rho g H cos\alpha tan\emptyset}{\rho g sin\alpha}\right)^{n} H^{-(n+1)} \quad (1)$$

here $\dot{\gamma}c$ is the critical shear strain rate of the material, n is the flow exponent, $\tau_{c\theta}$ is the cohesion, ρ is the density of the creeping material (given by the contribution of volumetric debris ω_d and ice content ω_i and relative densities), g is the gravitational acceleration, H is the thickness of the moving rock glacier, α is the surface slope angle (assuming parallel ground and shear surface) and $\emptyset$ is the friction angle of the shear zone material.

For Alpine rock glaciers, their thickness can be estimated with a perfectly plastic model (Cicoira et al., 2021), using the following formula:

$$H = \frac{\tau}{\rho g sin\alpha} \pm 3.4 \quad (2)$$

Adopting a plastic model for the rock glacier thickness and standard values of the material parameters ($\omega_i = 0.7$, $\rho = 1500$ kg m^3, $Ø = 25°$, $\tau_{c\theta} = 10$ kPa, $n = 2.1$ and $\dot{\gamma}c = 0.06$ a^{-1}) (Cicoira et al., 2021), the formulation of the BCF can be approximated to:

$$BCF = 7.6C_{obs}sin\alpha\left(\frac{0.5}{tan\alpha} + 0.1\right)^{2.1} \quad (3)$$

For our analysis, BCF values were computed from CIAS dense point measurements and the mean BCF value for each rock glacier zone was calculated and considered representative for that individual zone. Once the BCF was estimated, it was related to the dynamics and geometry of the rock glacier, and the relationships BCF-surface creep rates, BCF-slope angle and surface creep rates-slope angle were analysed. In addition, for the last analysed period (2019-2020) maps of the spatial distribution of surface flow, slope and BCF were produced. The surface creep rate map was generated by spatial interpolation (Triangulated Irregular Network interpolation method) of the velocity points detected with CIAS to estimate values at other unknown points. Through appropriate mathematical formula (Eq. 3), this product was combined with the slope map of the year 2020 for creating the BCF map (representation of the spatial distribution of the BCF patterns over the entire portion of the rock glacier) in 2019-2020 period.

In the absence of information on the internal structure (e.g., thickness of unfrozen debris layer, thickness of frozen core, presence or absence of an unfrozen sediment layer between bedrock and frozen core and ice content) of the Plator rock glacier, the BCF was calculated using reference values of the parameters as proposed by Cicoira et al., (2021). Furthermore, we assume a perfect plastic model for rock glacier thickness. This assumption looks realistic for alpine rock glaciers according to the results presented in Cicoira et al., (2021),

but the validation of this approach should be confirmed by a more detailed dataset.

This method provides information on the zones of the rock glacier that are experiencing a probable destabilisation phase or set in conditions unfavourable to permafrost preservation. This information may be used to plan detailed field surveys and in-situ measurements for those areas of rock glaciers that are changing mostly and to verify the reliability of the results derived from the BCF analysis, which can be used to understand long-term evolution of rock glacier dynamics.

3.4 Results

3.4.1 Accuracy of CIAS estimates

Table 8 reported the horizontal residuals (RMSE xy), the mean values of the maximum correlation and of the average correlation coefficients obtained in the image correlation analysis and the mean (ME) and standard deviation (STD) of the error computed on stable points for pairs of acquisitions (Fig. 10b for the point locations). The horizontal (x and y component) and vertical (z component) accuracy was assessed to evaluate the apparent displacement of stable ground points outside the rock glacier area.

Period	RMSE xy (cm)	Mean of max corr. coeff.	Mean of average corr. coeff.	ME | STD x (cm)	ME | STD y (cm)	ME | STD z (cm)
2016-2018	0.4	0.74	0.06	0.00 | 7.07	4.00 | 8.94	12.00 | 4.47
2018-2019	9.8	0.87	0.05	0.00 | 0.00	0.00 | 10.00	-4.00 | 8.94
2019-2020	4.3	0.73	0.05	6.00 | 8.94	0.00 | 7.07	4.00 | 8.94

Table 8. Root Mean Square Error (RMSE) and the mean coefficients (maximum and average) of stable points derived from CIAS. Mean (ME) and standard deviation (STD) of the horizontal and vertical error for stable ground points.

3.4.2 Velocity field distribution

The comparison between drone-derived orthoimages using the CIAS algorithm allowed the horizontal surface displacements at a high spatial resolution to be identified. The number of traced blocks and the mean surface velocity for each zone are shown in Table 9. Results highlighted the complex morphology and heterogeneous creeping pattern of the rock glacier zones. Table 9 shows that displacements did not increase at a constant rate but fluctuated over the measuring period. In Zone #1, the rock glacier moved slowly downslope with a deceleration from 0.7 m/y to 0.4 m/y between 2016 and 2019, respectively. On the other hand, 2019-2020 was the period in which the highest velocities (on average 0.9 m/y) were observed. The surface velocity was significantly higher in Zone #2. Horizontal surface velocity decreased from 2.30 m/y (2012-2016) to 1.40 m/y (2016-2018) and then, after 2018, a gradual increase was observed with a maximum value of around 2.3 m/y reached between 2019 and 2020. Immediately downstream of scarp #2, the largest surface displacements of the entire rock glacier were recorded. Although the trend and the temporal evolution of the movements agree with those observed in Zone #2, the surface velocities in Zone #3 are about twice as fast. Following a period of reduced displacements in 2016-2018, the rock glacier entered an acceleration phase with velocities increasing from 3.50 m/y in 2016-2018 to almost 4 m/y in 2019-2020.

The downstream movement of the rock glacier caused advancement of the front line and the front toe. The rock glacier front line advanced at velocity greater than 2.5 m/y following the main rock glacier flow line. In comparison, the presence of a topographic depression associated with a bedrock outcrop and veneer (Point A, Figure 10b), caused the front toe to advance at a rate lower than the average in its western part. The front toe moved at an estimated mean velocity between 3 m/y and 3.5 m/y.

Period	N° traced blocks			Mean surface velocity (m/y)				
	Zone 1	Zone 2	Zone 3	Zone 1	Zone 2	Zone 3	Front line	Front toe
2012-2016	47	75	74	0.71	2.30	4.24	2.69	2.98
2016-2018	141	98	91	0.60	1.40	3.50	3.55	3.27
2018-2019	148	102	107	0.41	1.70	3.84	3.61	3.18
2019-2020	55	38	122	0.90	2.25	3.87	3.42	3.42

Table 9. Table showing the number of traced blocks used to estimate the surface velocities in Zones #1, #2 and #3. The last two columns refer to the surface velocity of the front line and front toe of the rock glacier. For time intervals 2012-2016 and 2016-2018, the values refer to the annual average.

3.4.3 Rock glacier morphological changes

Between 2016 and 2020, the surface morphology of the rock glacier changed markedly (Figure 11) due to its continuous advancement and to its strong spatial variations in flow velocity. Displacement rates were small in Zone #1 while the morphological changes occurred mostly in Zone #3 and at the front where the highest movement rates were found.

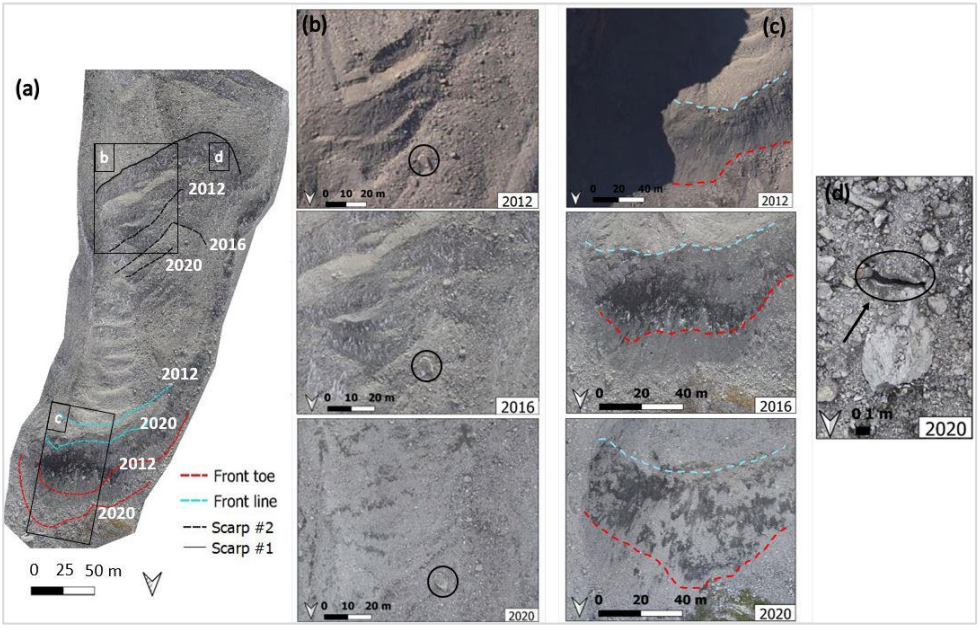

Figure 11. (a) Morphological evolution of scarp #2 (2012-2016-2020) and advancement of the front line and the front toe (2012-2020) of the rock glacier; (b) Surface morphological changes in Zone #2; (c) Morphological changes at the rock glacier front; (d) Open fissure formation in Zone #2.

The ongoing evolution of the rock glacier surface was indicated by distinct changes in its dynamics and modifications of the surface topography.

The shape of scarp #2 changed significantly (Figure 11a) over the 8-year period analysed in this study (2012-2020) and appears deep enough to be considered as an important element controlling the rock glacier destabilisation. The scarp evolved considerably from 2012 to 2016 in terms of both length and shape, cutting the entire rock glacier following the activation of the orographic left-hand side of the rock glacier. On the other hand, in 2020 the development of the scarp was like that of 2012, affecting only one side of the rock glacier. Considering the period between 2012 and 2020, it appeared particularly active and moved downstream constantly changing its morphological appearance. This also caused the separation of the rock glacier into two bodies with different kinematics.

In 2020, Zone #2 (Figure 11b) was characterized by a relative smooth and unstructured surface compared to previous years, likely due to new sediment input from the neighbouring rock walls.

The rock glacier showed extraordinary changes at the front (Figure 11c) due to the high displacement rates. Due to this, individual debris slide and gravitational movements in the form of isolated collapses randomly occurred. Caused by high velocities and the consequent advance of the rock glacier, subsidence and open fissures developed (i.e., fissure in Figure 11d) which are indicative of landform degradation and destabilisation. The fissures were mostly found in Zone #2, downstream of scarp #1, or close to scarp #2.

3.4.4 Spatial and temporal variability of the Bulk Creep Factor

Figure 12 shows the surface velocity as a function of the BCF and the surface slope angle for Zones #1, #2, and #3 in the periods 2012-2016, 2016-2018, 2018-2019 and 2019-2020. For the multiannual intervals (2012-2016 and 2016-2018),

the values of velocity, slope and BCF refer to the annual average of the given period.

The maximum calculated BCF values (up to 16) are found in Zone #3 close to the front, where the greatest surface rates are detected. The opposite situation is found in the rooting zone (i.e., Zone #1) where small rates correspond to the lowest BCF values, about five times smaller than in the frontal zone.

Zone #1 is the most gently inclined with a slope angle between 21° and 23° and shows the lowest surface velocities (< 1 m/y) resulting in the lowest BCF values, in the range 0.9-4.6. Zone #2 is characterized by surface creep velocities between 1.4 m/y and 2.5 m/y, BCF values between 2.2 and 7.7 and the highest values of surface slope angle (30°-31°). Surface slope angle of 24° and maximum values of both BCFs (17.8-18) and surface velocities (> 3.5 m/y) are representative of Zone #3.

The variability in flow velocities observed in the rock glacier zones can be explained by the BCF values (Figure 12c) but a unique relation with the surface slope angle (Figure 12b), which in turn is not directly related to the BCFs (Figure 12a), cannot be found.

According to the results, since there are no significant differences in the average slope angle between Zone #1 and Zone #3, the different surface velocities can be expressed by variations in the BCF. On the contrary, surface velocity of Zone #2 is driven by variations in both the BCFs and the slope angles.

Generally, a decrease in flow velocities corresponds to a decrease in the BCF values and vice-versa. Indeed, the velocity patterns depend by the high spatial discontinuity in the BCF between the rooting zone (Zone #1) and the lower part (Zone #3). Hence, proceeding from Zone #1 to Zone #3, the creeping process increases with the BCFs, reaching values typical of rock glaciers experiencing destabilisation behaviour. Furthermore, between 2012 and 2020, the mean BCF value representative of each zone increased progressively, with a dramatic rise

especially in the period 2018-2020 and particularly pronounced in Zone #3. This latter zone also shows much more pronounced annual variability in BCFs and in surface velocities than Zones #1 and #2.

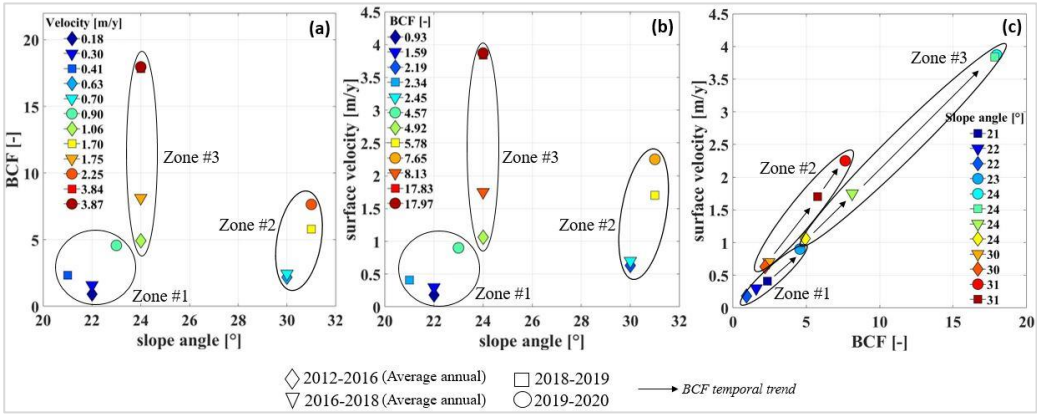

Figure 12. Representation of the relation between (a) slope angle and BCF; (b) slope angle and surface velocity and (c) BCF and surface velocity for Zones #1, #2 and #3.

In Figure 13, the spatial distribution of the surface slope angles (Figure 13a), the surface velocities (Figure 13b) and the BCF values (Figure 13c) for the most recent time interval are shown (2019-2020). The rooting zone (Zone #1) is the area where the minimum values of all these three parameters are found. Here, the mean surface velocity is lower than one metre per year, the mean BCF representative of the area is 4.6 and the average slope is 23°. The mean BCF value increases (7.7) in Zone #2 as well as the average slope (31°) and the creep rate, which reaches 2.3 m/y. A further increase in surface creep rate is seen in Zone #3, with values of almost 4 m/y, which is also associated with an increase in BCF, almost reaching a value of 18. On the contrary, the average surface slope angle (24°) is lower than that calculated for Zone #2.

The differences in the spatial patterns of surface velocity between the upper and the lower part of the rock glacier can be primarily explained by contrasting and discontinuous rheological properties (BCF) and secondarily by the slope angle differences between Zone #2 and Zones #1 and #3.

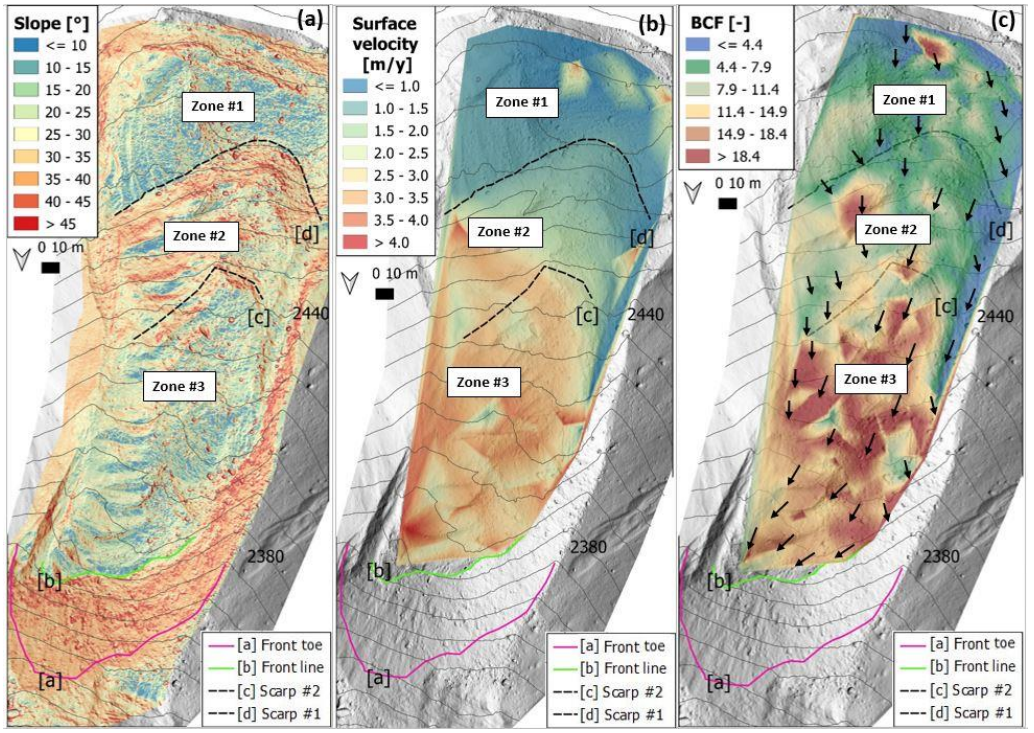

Figure 13. (a) Surface slope; (b) Spatial distribution of surface velocity; (c) Distribution of the BCFs and flow direction (arrows) of the surface creep. Period 2019-2020.

3.4.5 Vertical surface elevation changes

Vertical changes (Figure 14a) were detected by the difference of DSM (DoD) between 2016 and 2020 which showed distinct subsidence features of different magnitudes on the rock glacier surface. Figure 14b shows the mean annual vertical variations of scarps #1 and #2 between 2016 and 2020.

Negative elevation changes could indicate surface subsidence or mass loss processes, while positive changes may be due to an advancing of the rock glacier front or individual boulders moving across the rock glacier surface. Elevation changes in Zone #1 ranged from maximum values of 1.6 m to -2.4 m. Surface subsidence occurred in the rock glacier over the four-year period of measurement, particularly in the right-hand side of Zone #2 and immediately below scarp #2 where values of more than -4.0 m were reached (i.e., red colour

in Figure 14a). A major material loss in Zone #2, with negative changes of more than 4.0 m, was recorded, with a maximum peak of 5.6 m. An isolated area with positive changes was located below scarp #1, showing values between 0.4 m and 2.4 m. A slight accumulation of material was mapped in Zone #3 in the advancing ridge and furrow complexes. In these areas, the positive changes reached maximum peaks of 3.6 m, while the most intense material loss covered a range of 2.4 m and 4.4 m with peaks up to 5.6 m. Due to the advancement of the main body, only positive changes occur between the front line and the front toe with values ranging from 0.6 m to over 4.5 m. In addition, the presence of a topographic depression associated with a bedrock outcrop and veneer (Point A, Figure 10b) is causing a preferential advance of the rock glacier towards the orographic right-hand side, where the most intense positive variations (above 0.8 m/y) also occurred.

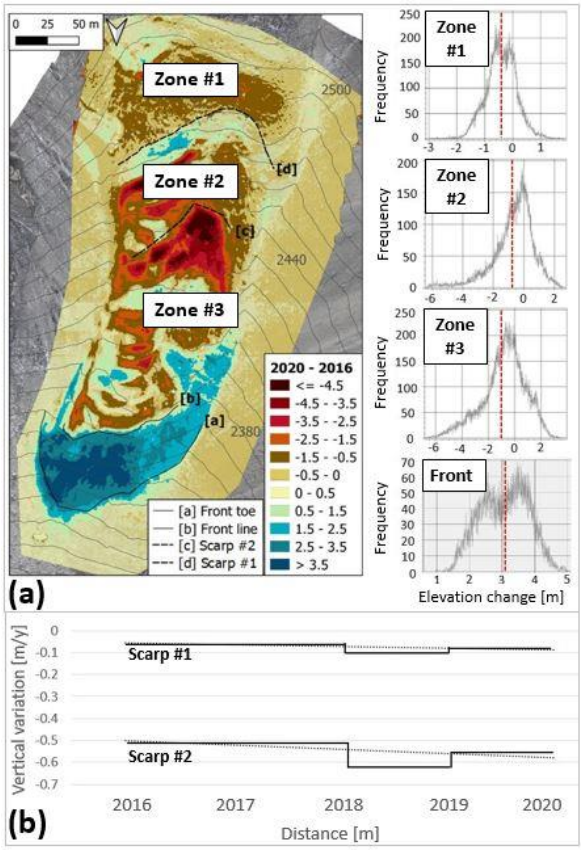

Figure 14. (a) DSM of differences (DoD) between 2016 and 2020 (left) and the associated frequency distributions of vertical changes [m] of the three zones and of the front part in the period 2016-2020 (right). The red dotted lines represent the mean difference. Please note the different axis scales for the four zones; (b) Mean annual vertical variations of scarps #1 and #2 with the respective linear regressions (black dotted lines). Period between 2016 and 2020.

3.5 Discussion

3.5.1 Evidence of suspected rock glacier destabilisation

The rock glacier destabilisation usually takes place on steep slopes as the internal shear stress increases with the slope angle (Delaloye et al., 2011). In destabilised landforms, scarps, crevasses, and fissures, her called "surface disturbances", can be formed (Marcer et al., 2019). Surface disturbances are in convex-shape bedrock surfaces where an extensive flow pattern and a thinning of the permafrost body occur (Delaloye et al., 2011).

Cases of rock glaciers experiencing destabilisation processes reported significant changes in the evolution of surface disturbances (Marcer et al., 2019). The frequency and size of these geomorphological characteristics can increase over time, creating growing discontinuities in the deformation and in the creep patterns of rock glacier and promoting additional rock glacier instability (Marcer et al., 2019). Distinct changes in surface topography have been described for several active rock glaciers in the Alps, indicating the destabilisation of these landforms (Marcer et al., 2021; Marcer et al., 2019; Buchli et al., 2018). Previous studies on destabilized rock glaciers showed that these landforms feature a wide variety of geomorphological characteristics (Roer et al., 2008; Kääb and Vollmer, 2000). Even with surface disturbances, rock glaciers can remain stable for decades (Roer et al., 2008), so the presence of these disturbances is not a sufficient condition for destabilisation to occur. Otherwise, the destabilisation process can be linked to an increase in surface disturbances as in the case of the Pierre Brune rock glacier where a crack observable since 1952, evolved to a crevasse in 1970 and further crevasses and a scarp formed after several destabilisation events (Marcer et al., 2019). In other instances, the surface perturbations on destabilised rock glaciers created a discontinuity in the flow pattern model (Scotti et al., 2017; Delaloye et al., 2008), but in two rock glaciers analysed by Schoeneich et al. (2017) and by Roer et al. (2008), high displacement rate (around 2 m/y) is not considered a necessary feature (Roer et al., 2008; Schoeneich et al., 2015). In fact, even rock glaciers that are not subject to an intense acceleration typical of destabilising phenomena and are therefore characterised by low displacements rates may still present cracks, crevasses, and scarps (Marcer et al., 2021).

The surface morphology of the Plator rock glacier is naturally shaped according to spatially variable flow patterns. The top layer of the rock glacier exhibits ridge and furrow topography attributed to compressive flow during the

rock glacier creep. Increasing flow velocity from the rooting zone towards the front and recent morphological changes in surface disturbances indicate that the strain rates increased significantly, suggesting an ongoing permafrost body split and/or thinning process, and promoting a possible destabilisation phase (Kääb et al., 2007). An example is the development of scarp #2, which was already particularly active between 2007 and 2012, as reported by Scotti et al. (2017). Since then, the scarp has shown a continuous morphological evolution over time reinforcing the belief that it could be a shear plane driving the destabilisation of the rock glacier, leading to an abrupt division of the surface velocity distributions.

Based on the classification defined by Marcer et al. (2019), the Plator rock glacier can be classified as "suspected or potential destabilized rock glacier" since the surface disturbances are clearly recognisable and evolve in time and the velocity field distribution is discontinuous with sectors moving significantly faster than others, as in the case of Zones #1 and #3.

Moreover, the downstream movement of the rock glacier is accompanied by a general subsidence of the rock glacier surface. The subsidence can be the result of permafrost degradation and the surface lowering may therefore depend on body acceleration, extensional flow, ice melting and reduced ice, consequently leading to changes in the BCF values (Cicoira et al., 2021; Müller et al., 2016; Bodin et al., 2015). As shown by the DoD map (Figure 14), the Plator is subject to a general surface subsidence and mass loss processes, particularly in Zones #2 and #3 with values occasionally reaching 1 m/y.

Between 2016 and 2020, zones of subsidence cover about 55% of the rock glacier of which about 18%, 28% and 54% in Zones #1, #2 and #3 respectively. The sector showing only material gains is the frontal area of the rock glacier (71%), due to the downstream movement of the tongue.

3.5.2 The Bulk Creep Factor interpretation

The Plator rock glacier was compared with other Alpine rock glaciers for which the BCFs, surface displacements and slope angles are available (Cicoira et al., 2021): Laurichard, Dirru, Furggwanghorn and Pierre Brune rock glaciers (Figure 15a). For the Plator rock glacier, the values referring to the period 2019-2020 were considered. The rock glaciers considered in these studies are characterised by velocity rates between 1 m/y and 6 m/y on relatively steep slopes, with maximum values of 28 degrees. The mean rock glacier altitude varies between 2450 m a.s.l. and 3600 m. a.s.l. The BCF values range between 5 (Laurichard rock glacier) and 23 (Pierre Brune rock glacier). At present most rock glaciers in the Alps are characterized by increased degrading permafrost conditions due to global warming but only rock glaciers currently experiencing destabilisation phenomena or set in conditions unfavourable to permafrost conservation are characterized by high, non-constant and discontinuous BCF values (Cicoira et al., 2021).

Despite its high BCF value, the Dirru is regarded as a rock glacier with very fast flow but not at risk of destabilisation due to almost spatially constant BCF values. The Laurichard rock glacier also shows homogeneous BCF values but is characterized by lower creep rates and slope variations. In both Dirru and Laurichard rock glaciers, there is an absence of abrupt changes in the BCF spatial variability even if the absolute BCF value is different, indicating rheological differences (material properties) and suggesting that the spatial variations in the creep rate cannot be explained by considering the slope angle only.

Both the Pierre Brune and the Plator rock glaciers can be considered as “ongoing destabilisation rock glaciers”, although with dissimilar BCF values. They both have distinct BCF patterns between the upper and the lower parts with the highest creep rates observed at the fronts in correspondence of the highest BCF values. Spatial heterogeneity of both velocities and BCF indicates

degradations conditions in the rock glacier. With the same mean BCF value of the Plator, the Furggwanghorn rock glacier is also subject to degradation, with acceleration and deepening depression in the rooting zone (Buchli et al., 2018).

For the Pierre Brune, Plator and Furggwanghorn rock glaciers, the velocity distribution could be explained by the (i) great spatial variation of the BCF, (ii) local topography and morphology (e.g. slope and thickness) and (iii) intrinsic characteristics such as the presence of ice bodies or frozen ground conditions.

On the Plator rock glacier, the heterogeneous velocity patterns between the upper (very low velocity, < 1 m/y) and the lower (high velocity, up to > 4 m/y) parts combined with high and discontinuous BCFs throughout the entire landform and the continuous development of the scarp #2 are clearly signs of ongoing destabilisation processes. The results obtained in this case study are in agreement with those of Cicoira et al., (2021) in which it is stated that rock glaciers currently involved in destabilisation processes or set in unfavourable permafrost conditions show high and discontinuous values of BCF.

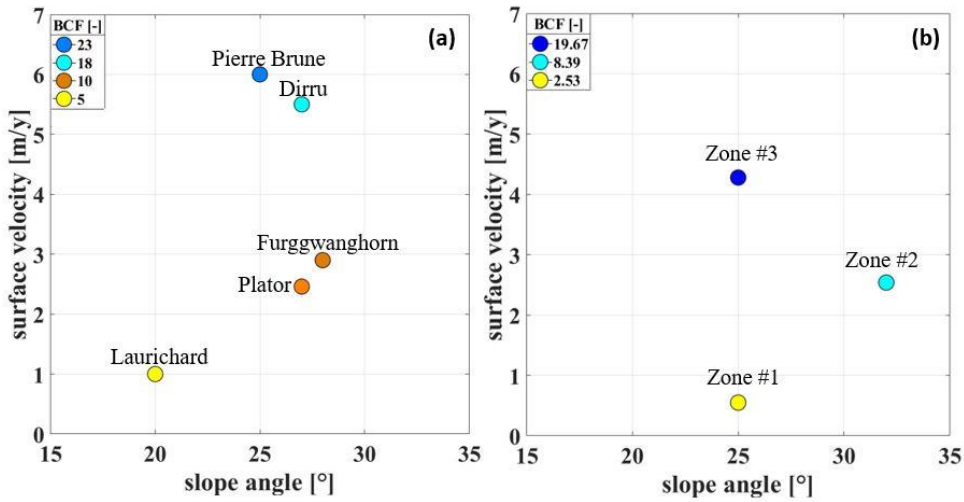

Figure 15. (a) Representation of the Plator rock glacier together with other rock glaciers (Pierre Brune, Dirru, Furggwanghorn and Laurichard). The position of the individual rock glaciers in the graph depends on the values of the relationship BCF, slope angle and surface velocity; (b) Representation of Zones #1, #2 and #3 of the Plator rock glacier considering BCF, slope angle and surface velocity in the period 2019-2020.

Considering the individual zones of the Plator (Figure 15b), Zone #1 evidenced a behaviour comparable with the Laurichard rock glacier which is described as steady-state creep (Cicoira et al., 2021). Zone #2 shows an increase of the BCF values in the years analysed suggesting an increase in the rock glacier activity. Zone #3, instead, has BCF values like those estimated for the Dirru rock glacier but differs in the BCF spatial distribution. Zone #3 is composed by a material prone to deformation (high and discontinuous BCF) and currently experiencing destabilisation processes.

The increase in the BCF is therefore a consequence of a current increase in the deformation state, probably dictated by an increase in ground temperatures, decrease in material cohesion and water content in the initial step of permafrost degradation (Cicoira et al., 2021; Kummert et al., 2017; Kääb et al., 2007). From 2012 to 2020, the BCF value representative of each Plator zone increases, according to the increase in surface velocities. The Plator rock glacier is undergoing a fast-moving phase typical of destabilized rock glaciers, with a very high surface creep rate in the front zone and a complex spatial pattern of BCF values.

3.5.3 Flow variations from 1981 to 2020 and probable causes of destabilization

The actual surface morphology of the rock glacier is the result of the evolution of the rock glacier kinematics and dynamical behaviour throughout the years. Combining the information obtained in this study with the results of Scotti et al. (2017), a time interval of 39 years (1981-2020) was covered (Figure 16a).

In the rooting zone (Zone #1), the displacement rates varied from 0.2 m/y in 1981 to 1.0 m/y in 2020. In the middle sector (Zone #2), creep rates become more relevant. In the 1981-2012 period, the Plator rock glacier moved downstream at an average horizontal velocity of 1.7 m/y while in the period 2012-2020 the

displacements were higher, reaching velocity higher than 2.2 m/y. Zone #3 reported the highest horizontal surface velocities with values gradually increasing over time. The minimum velocity was recorded in 1981 (with 2.8 m/y) and the maximum peak in 2012-2016 with 4.3 m/y. Between 2016 and 2018, the velocity dropped to 3.5 m/y but since 2018 there is a gradual and progressive increase in surface flow velocity.

The rate of advance of the front line and the front toe (Figure 16b) is related to the creep velocity of the tongue. The front toe advanced at 2.3 m/y between 1981 and 1994, increasing up to 4.1 m/y between 2007 and 2012. Between 2012 and 2016, the surface velocity decreased (2.9 m/y) but in the period 2016-2019 a fluctuating trend was observed, ending with an upturn in velocity of up to 3.5 m/y. Concerning the front line, the maximum horizontal surface velocity was recorded in 2003 (4.5 m/y), followed by an abrupt decrease in velocity until 2007 (1.3 m/y). Over the next 12 years (from 2007 to 2019) a steady and progressive increase in creep velocity was observed reaching a value of 3.6 m/y in 2019. In 2020, the velocity slightly decreased, reaching values comparable to those measured on the front toe.

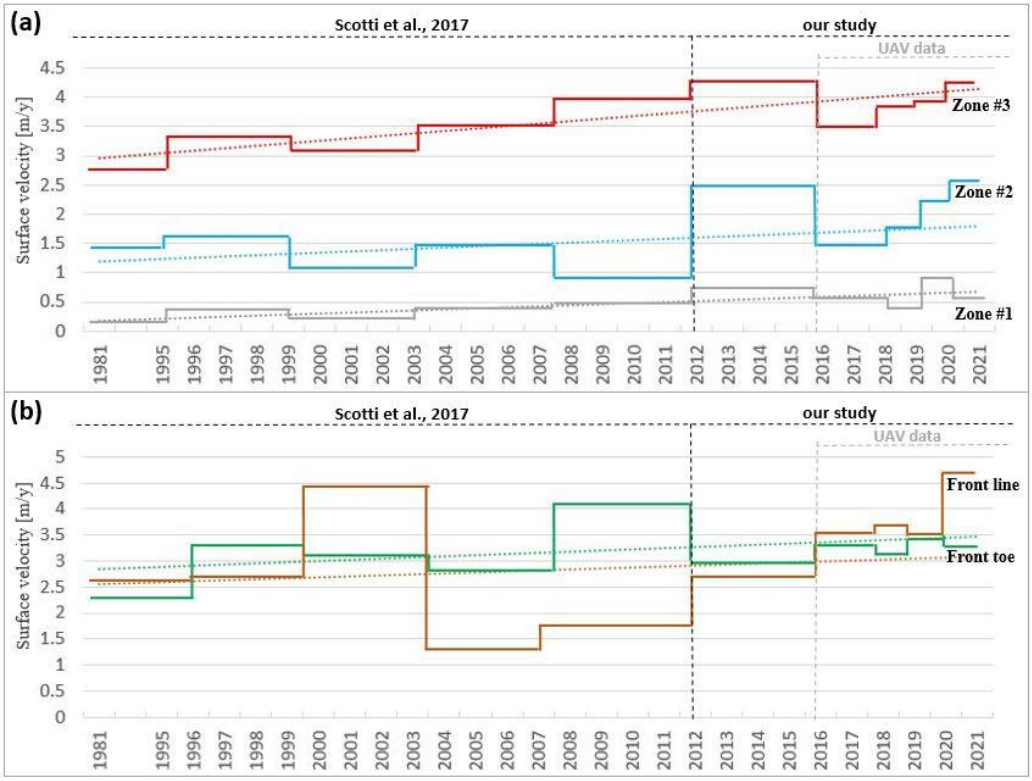

Figure 16. Horizontal surface velocities from 1981 to 2020 for: (a) Zone #1, Zone #2, and Zone #3; (b) Front line and front toe. The coloured dotted lines indicate the linear regression for each time series.

Some cases of collapse events (as the case of two rock glaciers in South Tyrol, described by Kofler et al., 20221, and the Bérard rock glacier, described by Bodin et al., 2017) and a significant acceleration of rock glaciers have been documented in the European Alps (Müller et al., 2016; Seppi et al., 2019; PERMOS, 2018; Delaloye et al., 2008) and elsewhere (Kääb et al., 2021; Eriksen et al., 2018). As documented in the Swiss Alps, for many rock glaciers a velocity peak was recorded in 2015, followed by a drop in surface creep rates in 2016-2017, due to ground surface temperature variations that reflect the variations of the temperature of the surface debris layers (PERMOS, 2018; Staub et al., 2016). Then, a continuous increase in surface velocities has been observed since 2018. This temporal course of surface creep velocity can also be observed in the Plator rock glacier and Zone #3 also shows surface velocity rates comparable to those

measured at the Bérard rock glacier (around 3.3 m/y), before its collapse in 2006 (Bodin et al., 2017). During the general acceleration phase between 2012 and 2015, the Plator showed surface velocity values higher than other rock glaciers (Vivero and Lambiel, 2021; Bodin et al., 2018) but some rock glaciers in Valais Alps are instead characterized by markedly higher velocity values, between 3 and 10 m/y (Delaloye et al., 2010). Eriksen et al. (2018), studying a rock glacier complex in northern Norway, measured velocities significantly higher than those at the Plator, reporting an increase in the average annual horizontal velocity from 3.6 m/y (2006-2014) to 4.9-9.8 m/y (2009-2016) (Eriksen et al., 2018).

Several factors need to be considered to explain the onset and development of rock glacier destabilization. The development of cracks and the destabilisation of rock glaciers tongues depend primary on the rheological properties of warming ice while the influence of liquid water in frozen material might be the major factor for permafrost close to 0°C and air temperature is an important factor controlling rock glaciers speed (Roer et al., 2008; Kääb et al., 2007). Kääb et al., (2007) demonstrated that rock glaciers characterized by ground temperature close to 0°C move usually faster than colder ones because the permafrost creep close to 0°C is more sensitive to thermal forcing compared to the colder one (Kääb et al., 2007). Within degrading permafrost, surface velocities increase, the ice content decreases, and the effect of temperature and liquid water influence deformation processes (Arenson et al., 2002). The combination of gravity-driven flow, topography (e.g., surface and bedrock slopes of the rock glaciers), and ice phase creep susceptibility may lead to an increase in deformations, changes in dynamics and possible development of rock glaciers destabilization in some cases (Marcer et al., 2021; Kenner et al., 2019; Delaloye et al., 2011; Jansen et al., 2006; Arenson et al., 2002).

On the Plator, a clear shear plane is represented by scarp #2 which could drive the destabilisation of the rock glacier, as already pointed out by Scotti et al.

(2017). This scarp appeared very active in the period analysed (2012-2020), initially affecting only the western portion of the rock glacier (in 2012) and later (2016-2018) partially developing also in east portion where deep tension cracks were mapped (Figure 11d). The scarp #2 caused the separation of the rock glacier into bodies with different kinematics.

The variations in the rock glacier kinematics can facilitate the development and the creation of surface openings (e.g., fissures) in areas subject to extensional regime, promoting possible increases in the rates of deformation. In addition to high displacement rates, the water input (from precipitation, snowmelt, thawing of the active layer or permafrost, or groundwater flow) within the system can also decrease the cohesive strength between the ice and debris particles (Kummert et al., 2017). Surface openings can promote the penetration of heat into the permafrost body, increase the permeability of the rock glacier to both surface water and external temperature, triggering positive feedbacks of rock glacier degradation (Marcer et al., 2021; Kääb et al., 2007). On the Plator rock glacier, such surface openings caused portions of pure ice to emerge which, without an adequate debris cover layer, are subject to the action of the external temperature, accelerating the degradation process.

High surface displacement rates at some rock glaciers also cause the frontal slope to steepen, increasing the shear stress on the sediment particles on the front (Kummert et al., 2017). As a consequence, gravitational movements may arise for particles not cemented with ice and beyond a certain threshold. This can be the case for the frontal part of the Plator rock glacier, where random changes in form of small collapses, individual debris slides, or gravitational movements occurred, resulting in local destabilisation phenomena over the years.

The Plator showed an acceleration trend, like many other Alpine rock glaciers, which could also have been favoured by the permafrost warming (Biskaborn et al., 2019), given the low elevation of its tongue, around 2370 m a.s.l.

Heterogeneous horizontal surface velocities between upper and lower parts of the rock glacier combined with high and contrasting BCF values and the continuous development of scarp #2 are clearly signs of starting destabilisation phenomena.

After this ongoing destabilisation process (high and heterogeneous spatial distribution of the BCF), we expect the BCF of the Plator to drift towards higher values in future years, continuing the growing trend recorded over the years investigated (2012-2020).

However, it is not possible to identify which of these factors play a key role in the destabilisation process of the Plator rock glacier. In the future, more in-depth analyses such as the installation of ground surface temperature sensors and detailed geophysical prospections will therefore be required to better understand which factors play a key role in the ongoing destabilisation process.

3.6 Conclusions

The horizontal surface velocities of the individual zones of the Plator rock glacier were investigated using image correlation analysis and successively discussed in relation to the BCF, which can be used to interpret long-term evolution of the dynamics of the rock glacier. Subsequently, based on the interconnections between BCFs, slope angles and creep rates, the rock glacier was compared with other Alpine rock glaciers. From the spatial and temporal distribution of the BCF values, and recently formed fissures, the Plator appears in an increasingly marked state of destabilisation that will tend to continue in the next years.

From 2012 to 2020, the average BCF value of different Plator zones increased due to increasing flow velocities. The high BCF values (close to 18) in the toe zone and the discontinuity of the BCF between the rooting and the frontal zone indicate that the Plator is experiencing a destabilisation phase or set in conditions unfavourable to permafrost preservation.

Like many other rock glacier in the Alps, the Plator experienced a general increase in surface velocities in the last years. On the Plator rock glacier, surface velocities steadily increased from 1981 reaching values up to 4 m/y in 2019-2020, confirming a trend already observed in the past on the same rock glacier. Increased horizontal surface velocities, development of new scarps and spatio-temporal BCFs distribution are factors suggesting an ongoing permafrost body split or thinning process.

The Plator is undergoing a fast-moving phase with a very high surface creep rate in the front zone and simultaneously shows high and complex spatial pattern of BCF values, typical of destabilised rock glaciers.

Rock glacier velocities significantly increased since the 1990s, suggesting that a warming climate may play a key role in this process. The continuous increase in displacement rates will probably lead to further changes and deformations, promoting possible future acceleration and destabilisation events.

The approach shown in this case study is a valuable method for investigating the state of rock glacier activity starting only from remote sensing data and allows to highlight rock glacier zones subject of destabilisation processes. This research can be replicated and applied to other landforms such as glaciers and landslides.

4 HYDROLOGICAL INFLUENCE OF AN ACTIVE ROCK GLACIER ON STREAM FLOW IN AN ALPINE CATCHMENT

The content of this chapter belongs to a manuscript that is currently in preparation.

4.1 Introduction

Rock glaciers are landforms consisting of an active layer (seasonal frozen debris layer which is typically a few decimetres to a few metres in thickness) covering ice-supersaturated debris (i.e., nonglacial) or pure ice (i.e., glacial). This active layer acts as a thermal filter, causing internal thermal regimes to be partially decoupled from the external micro- and meso-climates during the summer months (Jones et al., 2019) and consequently slows the melting of ground ice within the rock glaciers.

Rock glacier water storage occurs as ice, snow and water at long-term, intermediate-term and short-term timescales. Long-term storage includes ice storage below the active layer of rock glaciers on a period between multiannual and millennial timescales. The storage and release of snowmelt and active layer thaw-derived runoff on seasonal timescales constitute intermediate-term storage while short-term storage includes water diurnal drainage (Jones et al., 2019). Water discharge can hardly be measured in rock glaciers (i) with multiple and inaccessible springs (Krainer et al., 2012), (ii) without springs, i.e. the water drains within the debris (Krainer and Mostler, 2002), and (iii) with springs ending in lakes or ponds (Colombo et al., 2018c). In intact rock glaciers, the released water derives from snowpack melting, glacier ice melting, and rock glacier ice melting but also from rainfall and groundwater (Krainer and Mostler, 2002). Commonly, highest discharge rates occur during the spring/early summer

snowmelt and gradually decrease through summer and autumn while the lowest and near-zero flow rates are recorded in the winter months. During melt season, the discharge from intact rock glaciers is generally between < 1 to > 1000 L/s (Jones et al., 2019). Isotopic analyses of rock glacier springs, discharge rates and electrical conductivity (EC) sampling data are used to describe the seasonal evolution of rock glacier discharge composition (Jones et al., 2019; Colombo et al., 2018; Harrington et al., 2018; Krainer et al., 2007). Only limited studies (Miles et al., 2019; Winkler et al., 2016; Mari et al., 2013) assessed the groundwater flow and storage component of rock glaciers using artificial dye tracer tests.

Conceptual models of rock glacier hydrology suggest that the subsurface water movement occurs along two preferential flowpath types namely supra-permafrost flow and sub-permafrost flow (Giardino et al., 1992). This is consistent with the concept defined by Krainer and Mostler (2002) who identified two storage reservoirs, i.e. quickflow reservoir and baseflow reservoir which correspond to supra-permafrost flow and sub-permafrost flow, respectively. The quickflow usually occurs along a network of conduits eroded within the frozen rock glacier core whereas the baseflow indicates slow diffuse groundwater flow traveling through unfrozen, fine-grained debris at the rock glacier base. Water transiting through active rock glaciers by means of unfrozen drainage networks contributes instead to the formation of the intra-flow, i.e. intra-permafrost flow (Jones et al., 2019).

Active rock glaciers have a pronounced influence on the catchment hydrology (Hayashi, 2020) as demonstrated by Geiger et al. (2014). They showed that the rock glacier streamflow constitutes a significant proportion of total catchment runoff (15-30%), suggesting that rock glaciers act as impervious surfaces and potentially constitute hydrologically valuable long-term storage (Wagner et al., 2020; Jones et al., 2019). Harrington et al. (2018) also demonstrated that the

discharge from an inactive rock glacier spring, in the Canadian Rockies, contributed up to 50% of basin streamflow during summer baseflow periods and about 100% of basin streamflow over winter with 20% less drainage in the watershed basin.

These studies indicated the importance of understanding the internal structure of rock glaciers and how it affects groundwater storage and flow pathways. Rock glaciers need to be better understood in the light of climate change since they are climatically more resilient than glaciers (Jones et al., 2019; Rangecroft et al., 2016) and their hydrological contributions will gradually increase with the process of climate warming (Wagner et al., 2020; Jones et al., 2019). The understanding and the quantification of infiltration and recharge processes are therefore needed to forecast future changes in rock glacier runoff characteristics. Due to their influence on the runoff patterns of alpine headwaters, these landforms should therefore be considered also for ecological and water management issues (Wagner et al., 2020; Harrington et al., 2017).

The aim of this research study is to (i) quantify the rock glacier hydrological contribution on the catchment runoff and (ii) investigate the rock glacier groundwater circulation.

4.2 Study site

The study area is located on the south-western side of the central Alps, at the head of the Valtournenche Valley (Aosta Valley, Italy). Two lobes (Fig. 17), called White lobe and Black lobe, compose the main body of the Gran Sometta active rock glacier, ranging from 2630 to 2770 m a.s.l. The surface of the rock glacier consists of longitudinal ridges in the extensive central part, and a complex of transverse ridges and furrows in the compressive terminal part of the tongue. These two lobes differ in term of (i) geomorphological characteristics of the

debris cover layer, (ii) distribution of surface velocities, and (iii) internal structure (see chapter 2).

The Black lobe is composed of calcschists (65-70%), dolomitic marbles (25-30%), and metabasites with amphibolitic prevalence (5%); the lobe moves downstream at a velocity of about 1 m/y. Dolomitic marbles (60%), calcschists (25%), and metabasites with amphibolitic prevalence (15%) compose the White lobe; the lobe moves at an average annual surface velocity of 0.5 m/y.

The dynamics of this rock glacier can be explained by the heterogeneous distribution of permafrost and subsurface perennially frozen ground which is thick enough (around 20-30 metres) for permafrost creep to occur. The internal structure of the White lobe is composed by two high-resistive bodies in the central (30 m thickness) and downslope (20 m thickness) parts of the tongue which are interpreted as substantial frozen ground occurrences. These parts are overlaid by a less resistive layer representing the active layer and below by resistivity values < 5kohm-m indicating unfrozen conditions. A different internal structure is found on the Black lobe in which a continuous layer (20 m thickness) with high resistivity values (~100 kohm-m) is present under the active layer and representing a potentially slightly higher ice content (see chapter 2, subsections 2.3.3 and 2.4.1).

The head of the two rock glacier lobes is drained by two springs (one from each lobe), which discharge into the mainstream (Pousset River) of the catchment (Fig. 17a). In this catchment, a network of sampling points (Fig. 17b) was chosen to investigate the hydrological characteristics of the rock glacier, integrating data coming from geophysical prospections, analysis of discharge hydrograph of the springs, and tracing tests of artificial dyes.

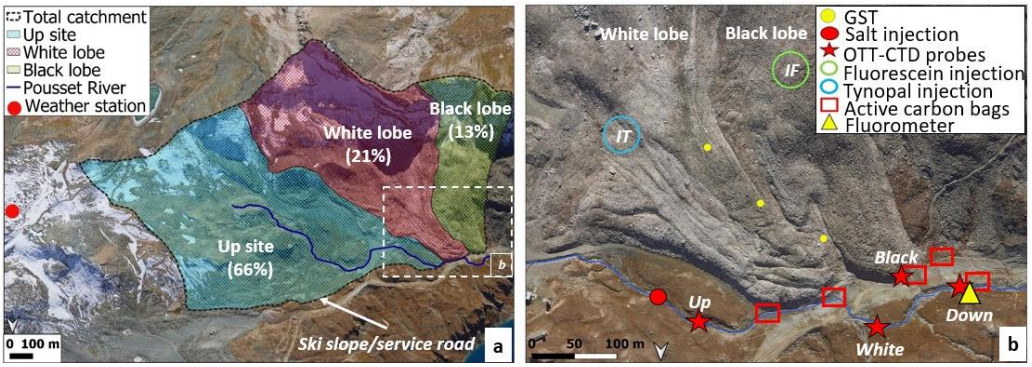

Figure 17. (a) Overview map of the study site, showing the location of the weather station Cime Bianche and the subbasin divisions with the respective contribution to the total catchment in percentage. (b) Detail view of the rock glacier sampling points: three ground surface temperature data loggers (GST in yellow dots), four probes (Up, White, Black, and Down in red stars), five active carbon fluorocaptors (in red squares), one field fluorometer (in yellow triangle), and three injections (salt in red dot, fluorescein - IF - and tynopal – IT in green and blue cycles respectively).

4.3 Data and methods

4.3.1 Meteorological data

Daily air temperature, snow depth and precipitation date were obtained from the weather station Cime Bianche, located close to the rock glacier, at 3100 m a.s.l. (Fig. 17a). The period investigated covers a period between the end of 2019 and 2021.

4.3.2 Salt injection and discharge estimation

Rock glacier discharge is an important variable to know in light of climate change. One approach to measure discharge involves injecting a chemical tracer and determining its dilution following the complete mixing into the flow. A popular tracer is a common table salt (NaCl) because (i) it is inexpensive and easily available, (ii) it can be measured directly in the field using an electrical conductivity (EC) meter, and (iii) it is non-toxic. The injection solution must have a sufficiently high salt concentration to produce an increase in EC while remaining below solubility. A salt dilution was injected at one point along the stream that favours rapid dissolution, and the resulting tracer concentration in

streamwater is measured as EC at a downstream point (Fig. 18). The mixing length was chosen to be about 20 times the average channel width (Hudson and Fraser, 2005).

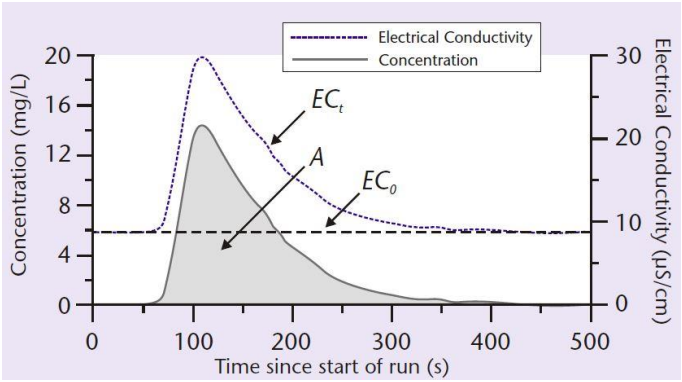

Figure 18. Salt dilution. The shaded area is the quantity of A that must be calculated. Figure: Hudson and Fraser, 2005.

Streamflow Q is calculated as: $\frac{M}{A}$ (1)

where M is the mass of salt and A is the area under the graph of concentration over time. A can be measured using:

$$A = \sum C_t \cdot t_{int} \quad (2)$$

where t_{int} is the time interval between successive data points and C_t is the concentration of injected salt at time t which is calculated through the equation 3:

$$C_t = (EC_t - EC_0) \cdot CF \quad (3)$$

where EC_t is the electrical conductivity at time t and EC_0 is the baseline conductivity. CF is the concentration factor which represents the coefficient in the near-linear relation between EC and salt concentration. However, CF is not a

constant since both stream temperature and background chemistry affect EC, thus it must be estimated every single time the tracer test is carried out.

In our study site, an injection point and three downstream measuring points were chosen (see Fig 17b for location points), following the guideline proposed by Hudson and Fraser (2005). After several tests to obtain a sufficient increase in EC, a mixture of 2 kg of NaCl in 10 litres of water was considered the right injection solution for our research purposes. The downstream points were chosen to quantify the hydrological contribution of the rock glacier on the catchment runoff, on the seasonal basis. In these selected points, probes (OTT-CTD Sensor) were installed which recorded physico-chemical parameters (e.g., EC, water level, and water temperature data) every 30 minutes and every 10 seconds only when the tracer test was performed.

The point "Up" was located downstream of the injection point and upstream of the rock glacier and quantified the water flow from the upstream catchment. The point "White" was placed in the stream downstream of the ski slope/service road and quantified the water flow given by the sum of the water leaving the White lobe and the water coming from the stream section outside the rock glacier. The third measuring point, called "Down", enclosed all the flow coming from the most upstream part, which is the result of the water coming from the two rock glacier lobes (White and Black which form RGs) and from the section of the stream upstream the rock glacier. Through the above-mentioned equations and subtraction calculations, the water flow was estimated at the three measuring points from June to October in 2019, 2020 and 2021 and the temporal trend of water supply of the rock glacier on the Pousset River was quantified. Tracer tests were carried out every two weeks. In addition to these three probes, another OTT-CTD probe (called "Black") was placed in the spring originating from the front of the Black lobe.

In order to estimate the EC contribution of both Up and RGs (and the single Black and White lobes contribution) to the site Down a "simple two-component mixing-analysis" (Penna and van Meerveld, 2019) was applied, averaging the flow values at sites White and Black to obtain a single component (RGs) and using Up as the second component.

4.3.3 Dye tracers test for storage-discharge characteristics

Two artificial tracer tests were performed to investigate the storage and flow dynamics in detail. Tynopal and fluorescein were injected on the surface of the rock glacier at the injection points IT and IF on 23rd July 2021, at 11.00 am and 11.40 am, respectively (Fig. 17b). IT was located about 2710 m a.s.l. on the White lobe whereas IF at 2735 m a.s.l. on the Black lobe. 200 g of tynopal and 50 g of fluorescein were injected at the respective IT and IF points and simultaneously rinsed using water tanks. Two methods were performed to sample the dyes passages: carbon bags with activated carbon and a field fluorometer.

Activated carbon is inserted into the carbon bags made by a perforated material allowing water to pass through them. If a dye tracer is present in the water, it will be absorbed cumulatively over the period in which the carbon bag has been immersed in water (Winkler et al., 2016) and will consequently provide the proof of the dye tracer passage in that point. In our site, five sampling points (Fig. 17b) were selected to place the activated carbons. For most of the duration of the experiment (from 16th July to 6th September 2021), two carbon bags with activated carbon were placed at each point simultaneously (Table 10). One activated carbon remained stationary throughout the experiment (A) while the second activated carbon (B) was replaced with another one (C) on the day of the dye injections (23rd July). Therefore, the activated carbon B remained in the water from 16th to 23rd of July and the activated carbon C from 23rd of July to 2nd of August.

Date	Activated carbon
16.07.2021 – 06.09.2021	A
16.07.2021 – 23.07.2021	B
23.07.2021 – 02.08.2021	C

Table 10. Sampling intervals of the carbon bags for the five monitoring points.

Unlike carbon samples analyses, which can provide purely qualitative interpretations, the use of a field fluorometer allows to quantify the amount of dye tracer passing through the downstream point (yellow triangle in figure 17b). A GGUN-FL24 fluorometer was used with a recording rate of 5 min in the week before injection (16th - 23rd July 2021), of 1 min in the week after injection (23rd July - 2nd August 2021), and of 5 min until the end of the automatic observation on 6th September 2021. The location of the field fluorometer is shown in figure 17b (yellow triangle).

The tynopal transition was not detected, while the recovered mass of fluorescein detected by the fluorometer was estimated using the QTRACER2 software which solves the equations from user-generated data input files through integration of consolidated hydraulic models (U.S. EPA, 2002). The fluorometer data were filtered to remove daytime noise, probably a consequence of solar radiation shielding on the instrument's sensor, and only night data were considered, range 8pm-6am. The recovered tracer concentration was estimated only for the week following the injection, i.e. from 23rd July to 2nd August 2021, characterized by low water turbidity.

4.4 Results

4.4.1 Weather conditions during the monitoring period

During the years of monitoring (Fig. 19a), at the weather station Cime Bianche, a mean air temperature of -2.3 °C was recorded between 2020 and 2021. In 2021 there was an early of the snowmelt (22th June) compared to 2020 (10th July). Considering the months of the campaigns, from June to early October (Figs. 19b and 19c), 2020 was warmer (mean air temperature = 4.5 °C) and drier

(total precipitation during the snow free period equal to 189 mm) than 2021 (3.1 °C; 239 mm). Table 11 reports the monthly average of air temperatures recorded at the weather station Cime Bianche during the months of field campaigns, between June and October.

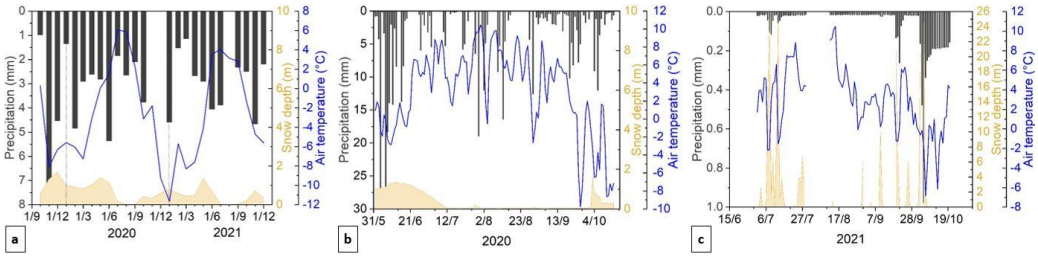

Figure 19. (a) Monthly values for precipitation (in mm, black columns), snow depth (in m, orange area) and air temperature (in °C, blue line) between the end of 2019 and 2021. Daily precipitation (in mm, black columns), snow depth (in m, orange area) and air temperature (in °C, blue line) during the months of field campaigns in 2020 (b) and 2021 (c).

Year	Mean air temperature (°C)				
	June	July	August	September	October
2020	1.5	6.1	5.9	2.2	-3.1
2021	3.6	4.0	4.9	2.8	-1.3

Table 11. Mean air temperature for June, July, August, September, and October in 2020 and 2021.

4.4.2 Discharge rates from saline injections

Two (in July and October), seven (between July and September) and nine (between July and October) saline injections were made in 2019, 2020 and 2021 respectively (Fig. 20). The maximum recorded discharge was 0,13 m^3/s in 2019, 0.14 m^3/s in 2020 and 0.16 m^3/s in 2021 at the sampling site Down, in July. From July onwards, at all three monitoring sites, flow discharges decreased to reach minimum values of 0.006 m^3/s in 2019, 0.01 m^3/s in 2020 and 0.008 m^3/s in 2021, at the Up point in October (2019) and September (in 2020 and 2021). In the years under consideration, the highest discharge rates were recorded at monitoring point Down, followed by those measured at the White point and the lowest values at the most upstream point (external to the rock glacier landform), i.e. Up.

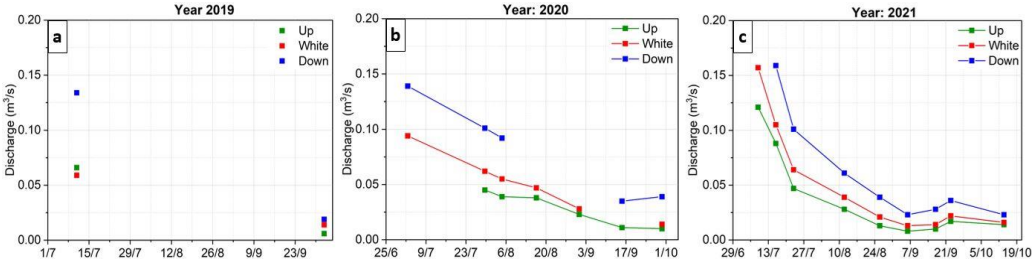

Figure 20. Discharge rates (m^3/s) estimated at the points Up, White, and Down in 2019 (a), 2020 (b) and 2021 (c) Note that there are data gaps in 2020 due to the presence of fine material in the probe sensors, which led to incorrect functioning.

The RGs (Black and White lobes) constitutes 34% of the total catchment (see Table 12 and Fig. 1a). The total relative contribution of RGs on the sampling point Down was estimated to be 62%, with a gradual increase in its contribution during the period July-October (Fig. 21a). Higher RGs contribution on the Pousset River was reached in September-October with nearly 65,4%.

The water contribution of the White lobe had a greater influence on the Pousset River in early summer (July with 40%) and decreased over the following months (Fig 21b). Even though the White lobe has a significantly larger surface than the Black lobe, it contributed less significantly than the adjacent lobe. The contribution of the stream exiting the White lobe decreased over time, contributing only 27% in the last surveyed interval. On the contrary, the water contribution of the Black lobe became more relevant during the summer season, contributing more significantly at the end of the investigated period, September-October. Considering the total period (July-October), the Black lobe contributed more (63%) than the White lobe (37%) on the Pousset River and its contribution became progressively greater over the monitoring period. In fact, the Black lobe spring had a significant contribution (72%) on the catchment streamflow during September-October.

During late August and mid-September, despite a reduced drainage of the catchment (Fig. 20), the most important contribution came from the two lobes of

the rock glacier (62%) rather than the Up component, with particular emphasis on the Black lobe (71%) compared to the White lobe (only 29%).

The volume of water released by the rock glacier lobes during the July-October campaigns was 221,000 m^3, with 157,000 m^3 coming from the Black lobe. Considering only August, the Black lobe released a volume of 59,000 m^3 out of 88,000 m^3 from the entire RGs body.

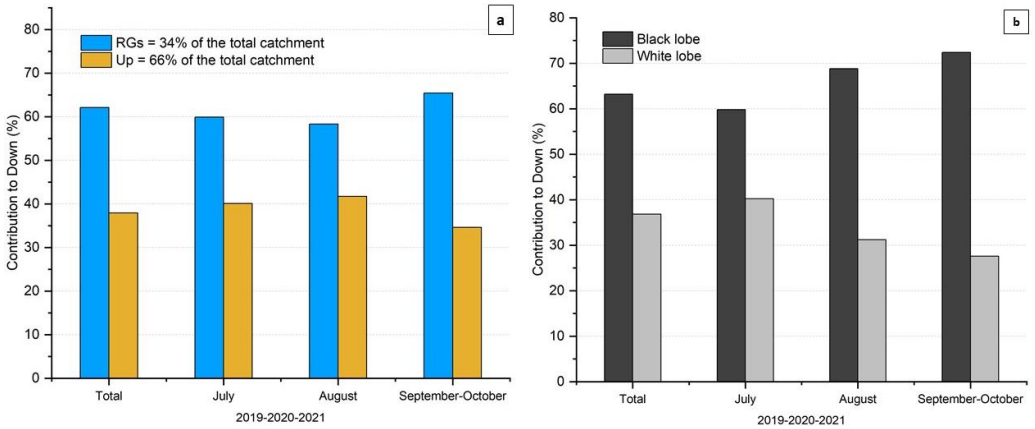

Figure 21. Monthly discharge in the cumulative period 2019-2020-2021. (a) Monthly discharge contribution (in %) at the Down point between the rock glacier (RGs = Black lobe + White lobe) and Up; (b) Monthly discharge contribution (in %) at the Down point between the Black and White lobes. Time interval investigated: Total (from July to middle October), July, August, and September-October.

Catchment	**Area (m^2)**
Total basin	1316542
Up	863608
Black lobe	173488
White lobe	279446
Contribution to the total basin (%)	
Up	66
RGs	34

Table 12. Subbasin areas (see Fig.17) and contribution to the total basin (%).

4.4.3 Temporal patterns of physico-chemical parameters

The continuous monitoring of EC and water temperature revealed contrasting patterns for the three springs (Up, White, and Down) during the study period.

Both in 2020 and 2021, higher values of EC (between about 190 and 262 µS/cm) were recorded at the point Down and lower values at the Up site (from about 130 and 196 µS/cm), in which there was no mixing with water from the rock glacier (Fig. 22 and Fig. 23). EC was generally higher at the two rock glacier lobes where the highest values were found in the Black lobe stream.

Considering EC (Fig.24), between 2019 and 2021, the relative contribution of the two rock glacier lobes (RGs) in the sampling point Down was estimated 55% throughout the summer season, with a progressive seasonal increase showing the highest values in September-October (63%). Seasonal variations showed a progressive increase in the relative contribution of the RGs on the Down site as the summer season progressed, underlying the greater importance of the contribution of the two lobes after the end of the snowmelt period. Seasonal variations were not clearly evident in the White lobe spring, while they were prominent in the Black lobe stream with general increases recorded especially during the late summer and early autumn (September-October).

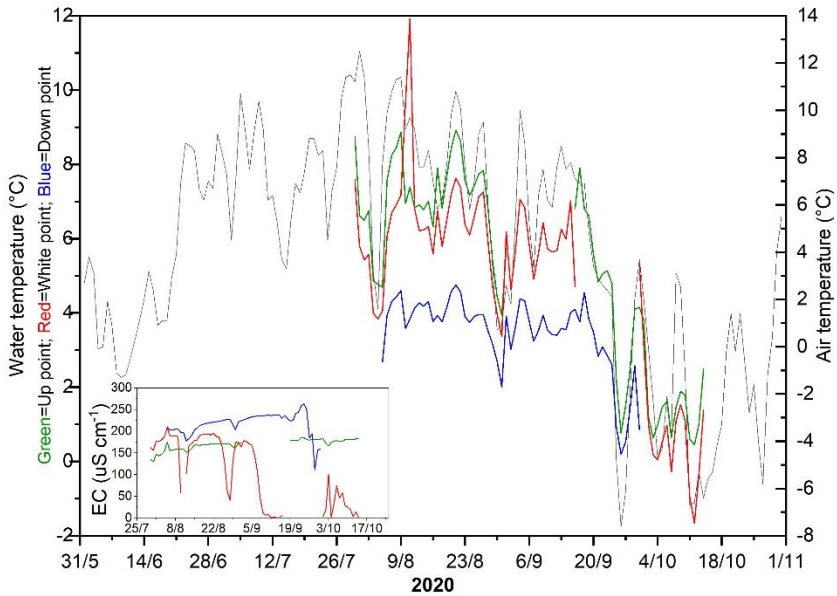

Figure 22. Daily average series of air temperature (black line) and water temperatures and Electrical Conductivity (EC, in the box) in green, red, and blue lines. Period June-October 2020.

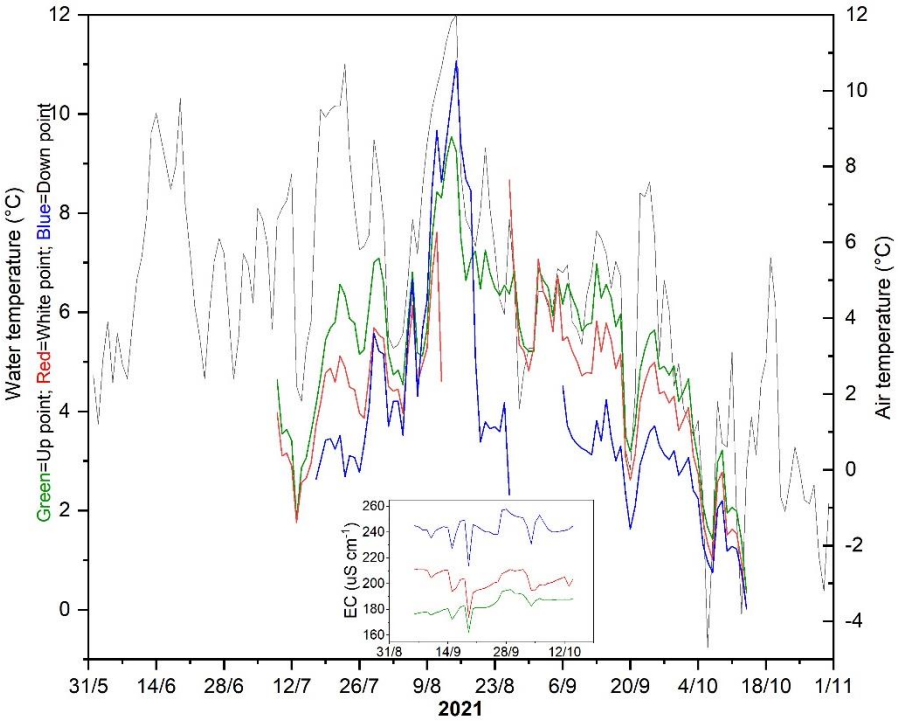

Figure 23. Daily average series of air temperature (black line) and water temperatures and Electrical Conductivity (EC, in the box) in green, red, and blue lines. Period June-October 2021.

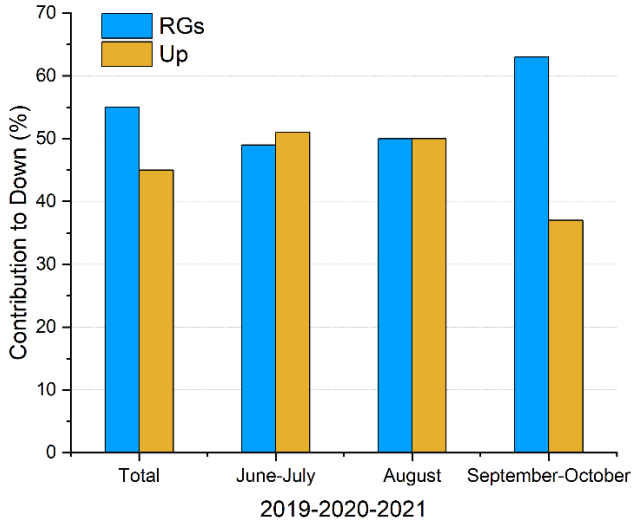

Figure 24. Electrical Conductivity contribution (in %) at the Down point between the rock glacier (RGs = Black lobe + White lobe) and Up in the cumulative period 2019-2020-2021.

The impact of the meltwater from the two lobes on the Pousset River did not only occurred in the modification of flow rates but was also evident in the modification of water temperatures and their daily variations (Figs. 22 and 23 in green, red and blue lines). The water temperature was higher at the sampling point Up than at the rock glacier springs. In general, daily minimum water temperatures were recorded during the snowmelt period and the first snow cover event. The daily water temperature fluctuations followed a common pattern with air temperature variations, with maximum values in August.

Due to the low water temperature of the two springs of the lobes (defined as RGs in Figs. 25a and 25b), the Black and White lobes showed the ability to lower the average water temperature of the Pousset River by a mean of approx. 2.8 °C, with a more important cooling effect caused by the Black lobe (Fig. 25b). The influence of the two lobes was also evident in the magnitude of the daily temperature variations, which were reduced in the meltwater of the rock glacier lobes and with a significant reduction downstream of the two lobes.

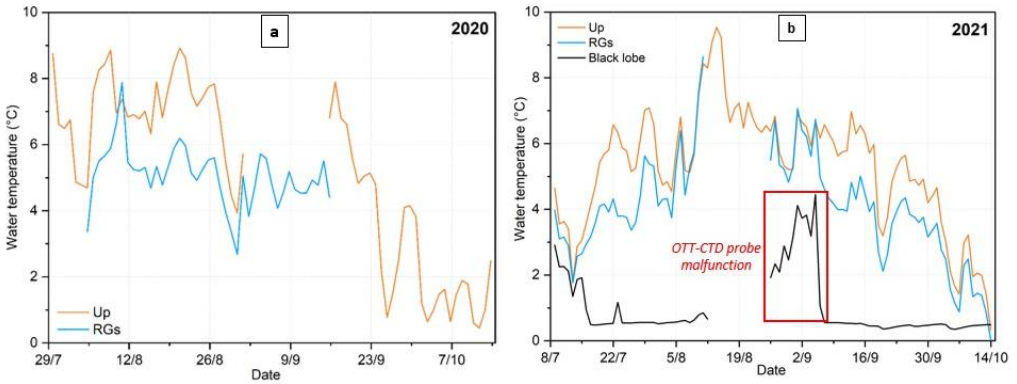

Figure 25. Mean daily water temperature between Up site and RGs (contributions of both rock glacier lobes) in 2020 (a) and (b) mean daily water temperature between Up site, RGs, and Black lobe in 2021.

4.4.4 Storage-discharge characteristics using tracers' data

One of the two dye experiments gave successful return (fluorescein), while the other one (tynopal) was not detected until the end of the automatic observation on 6th September 2021.

Tynopal was not detected at any of the carbon bag control points (Fig. 26, first row). This was evident from the very small range of concentrations (expressed in ppb - part per billion) and no clearly different values detected by the carbon bags during the monitoring period. On the other hand, fluorescein was tracked with a strong signal by two carbon bags (Fig. 26, second row). As early as the week following the injection (23rd July – 2nd August, activated carbon C), two points showed very high concentration values (3.15 ppb and 1.52 ppb), compared to the other points, testifying the effective passage of the tracer through these specific points. The highest concentration was estimated at 3.15 ppb in the carbon bag located in the stream draining the Black lobe while the second highest value (1.52 ppb) was found in the carbon bag located in the Pousset River at point Down. The other carbon bags did not detect the passage of the tracer (concentration lower than 0.6 ppb) during the period 23rd July – 2nd August. This was also confirmed by the analyses of the carbon bags kept on site throughout the campaign, i.e. from 16th July to 6th September (activated carbon A). Again, the highest fluorescein concentrations were found at the same two locations, namely at the Black lobe stream (13.92 ppb) and in the Pousset River at point Down (5.60 ppb). These carbon bags, which remained in the water for a longer time, were able to accumulate more dye than those that remained in place for a shorter time and consequently showed higher concentrations. Although qualitative, these data evidence that the tracer injected into the Black lobe at the IF point (Fig. 17b) on 23rd July 2021 only passed through these two points already in the week following the injection.

These results on the tracing of tynopal and fluorescein were confirmed by the quantitative analyses derived from the field fluorometer.

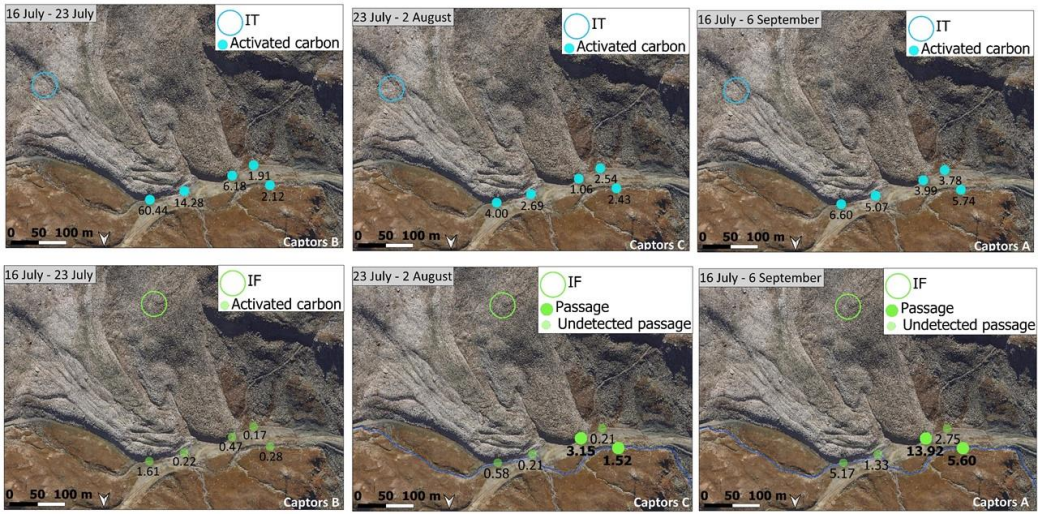

Figure 26. Carbon bags with activated carbon points and their concentration values (express in ppb - parts per billion) for tynopal (first row) and fluorescein (second row) in three intervals of time in 2021: 16th July – 23rd July (days before the injection), 23rd July – 2nd August (days after the injection) and 16th July – 6th September (total duration of the field campaign). IT = Injection point of tynopal and IF = Injection point of fluorescein.

The field fluorometer did not detect the transit of the tracer tynopal during the sampling period (23rd July – 6th September) but only the fluorescein was returned at the point Down (Fig. 27). Analysing only the night-time data (8pm-6am), the dye tracer fluorescein behaviour exhibited a double response component. A first and fast response could be observed within a couple of hours (first arrival) and, on the other hand, a larger storage component and a delayed release (second arrival). The tracer was detected for the first time 32 hours after injection, with the estimated peak (0.1 ppb) reached approximately between 25th and 27th July 2021. Since only night data were considered, the estimated 32 hours of the first arrival are likely overestimated.

The maximum change of tracer concentration occurred with a time lag of 10 days after the first arrival (red asterisk in Fig. 27). This was considered to be the beginning of the second arrival, during which the tracer concentration gradually

increased to a maximum value of 1.8 ppb on the day of field fluorometer removal. The first arrival happened in correspondence of rainy period whereas the second arrival occurred during a period of almost total absence of precipitation. Both arrivals occurred in free snow cover condition.

In the week following the injection alone, from 23rd July to 2nd August, a return rate of tracer injected of 7.16% was calculated. The distance trace, the mean tracer velocity, and a total quantity of tracer recovered were approximately 450 m, 3.40 m/hour, and 3.58 g (out of 50 g injected), respectively.

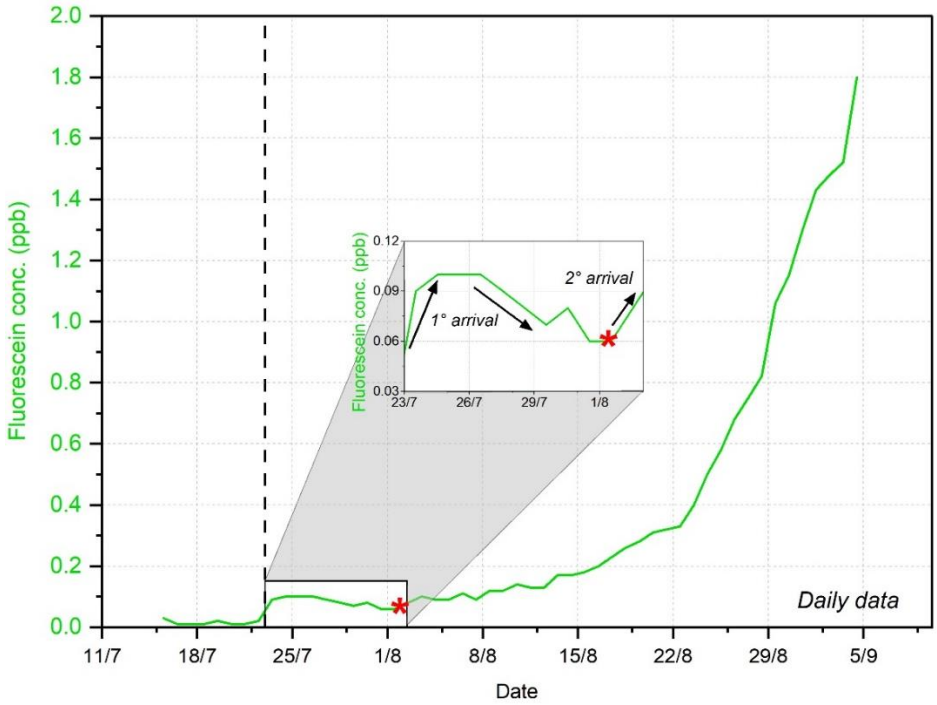

Figure 27. Return curve of fluorescein derived from night data, from 8pm to 6am. The dashed line indicates the day of the dye tracer injection (23.07.2021) and the red asterisk indicates the probable day (03.08.2021) of the beginning of the second arrival.

4.5 Discussion

4.5.1 Discharge rates and rock glacier hydrological contribution

The maximum recorded discharges of the rock glacier were observed during the snowmelt period and with the most abundant flow measurements happened at the lowermost sampling point, i.e. Down. The peak discharge of the Gran Sometta rock glacier was 0.13 m^3/s in 2019, 0.14 m^3/s in 2020 and 0.16 m^3/s in 2021 during July, mainly due to snowpack melting. As long as rock glaciers were covered with snowpack, a relevant part of the water that flowed out of these landforms was due to the snow melting process, which caused high discharges during spring and early summer (Krainer and Mostler, 2002). During August, when the winter snow was almost completely melted, discharge significantly decreased. The active rock glacier contributed 62% of catchment streamflow during the period July-October. The relative contribution of the rock glacier increased towards the end of summer season and the beginning of autumn with highest influence (65%) on the Pousset River in September-October. The minimum runoff from the rock glacier happened in correspondence of low intensity rainfall.

High hydrological differences concern the two rock glacier lobes. During the period July-October, the White lobe contributed significantly less (37%) than the Black lobe (63%) on catchment streamflow. During only September-October and considering the contribution of the Black lobe on the White lobe, the Black lobe contributed up to 73% to the Pousset River, representing a significant high proportion of total catchment runoff.

The results are consistent with other studies on rock glacier runoff, confirming that the peak discharges occur mainly during the snowmelt season (Harrington et al., 2018; Geiger et al., 2014; Krainer et al., 2007; Berger et al., 2004). The fact that the Gran Sometta active rock glacier influence on the catchment runoff was greater towards the end of the summer season and the beginning of autumn

suggests the important role of this rock glacier as a water resource, especially in those periods when the contribution of snowmelt is reduced or absent.

4.5.2 Hydrological characteristics

The water from the two rock glacier lobes affected the Pousset River not only modifying the discharge rates but also influencing its temperature.

Due to the low temperature of the water gushing from the Black and White lobes (Colombo et al., 2018; Harringhton et al., 2017; Krainer et al., 2007; Williams et al., 2006), these two lobes showed the ability to lower the average water temperature of the main stream by ca. 2.8 °C, with a more important cooling effect caused by the Black lobe. The influence of the two lobes was also evident with regard to the amplitude of daily thermal variations, which was generally reduced in the water of the RGs (Colombo et al., 2018; Carturan et al., 2016; Krainer et al., 2007; Harris et al., 1994), with a significant reduction downstream of the two lobes and a greater influence shown by the Black lobe. The most intense daily fluctuations were detected during the snowmelt period (Brighenti et al., 2021) with late evening minima and mid-day maxima. Water temperatures suggest the existence of internal ice and/or permafrost supplying the springs (Millar et al., 2013). The low water temperature of the Black lobe spring, near 0 °C, suggests that the water flow is in direct contact or in proximity to ice or permafrost within the rock matrices (Millar et al., 2013; Berger et al., 2004; Scapozza et al., 2009; Haeberli et al., 1975).

Groundwater flows (mixture of snowmelt, precipitation and ice melt) passing through the sediment and fractured bedrock below frozen core of rock glaciers can be recognised by EC values. In general, EC and discharge of alpine rock glaciers are inversely correlated (Wagner et al., 2021; Krainer et al., 2007). At the beginning of the melt season, low discharge rates correspond to high EC values. When almost all winter snow is disappeared, EC values increase

continuously until the end of the melt season, thereafter, as the discharge flow increases, the EC values tend to decrease rapidly.

EC is generally higher in the Black and White lobes than in the Up site, with the highest values found in the Black lobe. Seasonal variations at Black lobe are evident, with general increase recorded especially during the late summer and early autumn (September-October). Seasonal increase in EC and major ion concentrations in the meltwater of the lobes are attributed to the progressive reduction of the snow contribution (low in solutes) and an increase in the contribution of meltwater from internal ice and groundwater, enriched with solutes (Krainer et al., 2007; Williams et al., 2006).

The relative EC contribution of the two lobes on the Down sampling point is estimated to be 55% throughout the summer season, with a progressive seasonal increase showing the highest values in September-October (63%). This represents an important factor in determining the chemical characteristics of the waters influenced by the input of meltwater from the two investigated lobes.

The seasonal variations show a progressive increase in the relative contribution of RGs on Down site as the summer season progresses, underlying a greater importance of the contribution of the two lobes after the end of the snow melt period.

4.5.3 Groundwater flow and storage mechanisms

The results of the analyses of the carbon bags with activated carbon and field fluorometer data evidencing the return period of the two dye tracers (tynopal and fluorescein) confirmed the extreme diversity of water circulation of the two rock glacier lobes and their hydrological differences.

On the White lobe, tynopal was injected at the IT point (Fig. 17b) on 23rd July 2021, which was never detected until 6th September 2021. In accordance with the ERT data (chapter 2, Fig. 2), the injection point was located at a thick unfrozen

zone therefore it is not excluded that a part of the dye tracer infiltrated to great depth into the debris body and circulated under the permafrost zones slowly. This increased its storage capacity and could explain a slow residence time of the dye tracer (Rogger et al., 2017). Since this area was subject to the presence of a small glacier during the Little Ice Age, it is possible that the glacial erosion formed hummocks and depressions. The non-response of the tynopal on this rock glacier lobe could be related to (i) the presence of these bedrock depressions that would create "fill-spill" or "fill-spill-drain" types of mechanisms (Harrington et al., 2018) that allow the slow drainage of groundwater stored, and (ii) unfrozen layers responsible for groundwater storage and retarded runoff (Wagner et al., 2021).

Due to a different internal structure, it is likely that the White lobe is characterized by a prevalence of deeper groundwater flow due to major areas of unfrozen layers while in the Black lobe two flowpaths prevail: a shallower groundwater flow (on the surface of the permafrost table and above the perennially frozen debris rich in ice) and an intra-permafrost flow.

The fluorescein injected into the Black lobe at point IF (Fig. 17b) was tracked by both the activated carbons and the field fluorometer (Figs. 26 and 27) which showed the first detection of the tracer 32 hours after the injection only (note that only night data were considered so it is possible that the first detection time is overestimated). The discharge behaviour exhibited primarily a fast response (first arrival) and secondarily a delayed flow component (second arrival). The first arrival was presumably associated with the water circulation into the active layer and above the table of perennially frozen debris rich in ice and occurred in the shallow permafrost free deposits. The second arrival was attributed to a higher storage component due to the water transiting more slowly through deeper layers of perennially frozen debris (Jones et al., 2019; Winkler et al., 2016; Tenthorey, 1992). Based on discharge measurements, in the first week after the injection the return rate of tracer, i.e. first arrival, was 7.16%. The remaining percentage of

dye infiltrated from the active unfrozen layer and penetrated the underlying zone, reinforcing the idea of an intra-permafrost flow circulation of the second arrival. The tracer mass recovered is in line with that found in other case studies dealing with the rock glacier circulation with artificial dye tracers. It should be noted that in such studies the monitoring period was much shorter (hours or a couple of days) than in our case study (almost two months) and very few involved active rock glaciers but rather debris-covered glaciers (Miles et al., 2019; Fyffe et al., 2019). An example of a tracer test performed on an active rock glacier is that carried out by Mari et al. (2013) on the active Tsavolire rock glacier, in Vallon de Réchy (Switzerland) that injecting 1 kg of eosin tracer estimated a return rate of 10% with a maximum peak after 11 hours.

4.6 Conclusions

The analysis highlights the hydrogeological importance of the rock glacier as a complex groundwater body with important storage and buffer capabilities.

The result of the analyses clearly shows the capacity of the Gran Sometta rock glacier to influence not only the hydro-chemical characteristics of the water of its sources, but also those of the runoff catchment within which its meltwater is collected. The fact that the rock glacier contribution is greater towards the end of the summer season and the beginning of the autumn season suggests the important role of this debris body as a water resource, especially in those periods when the contribution of snowpack melt is reduced or absent.

In addition, the electrical conductivity shows seasonal variations, being lowest in early summer due to the high amount of quickflow derived from snowpack melt, and successively increasing towards early autumn due to the reduction of the snow contribution and an increase in meltwater contribution from internal ice and groundwater.

The low temperature of the water discharged from the two rock glacier lobes, close to 0 °C, suggests that the water flow is in direct contact or in proximity to ground ice or permafrost within the rock glacier. The rock glacier springs show the ability to lower the average temperature of water of the main stream by ca. 2.8 °C.

Permafrost bodies within rock glaciers might disappear in the future, thereby potentially increasing the groundwater storage capacity of rock glaciers. The hydrological relevance of rock glaciers to runoff in Alpine catchments will gain in importance and need to be understood also for the maintenance of ecological diversity as climate change progresses.

5 CONCLUSIONS

5.1 Conclusions and main findings

The main objectives of this Ph.D. are to investigate the morphological changes and the surface velocities of two rock glaciers at different time scales and prove insight into the relationship between some meteorological forcing, thermal state of permafrost and water input on rock glacier dynamics. Considering the warming climate, understanding rock glaciers destabilization evidences and their increasing contribution to the quantity and quality of surface water of a catchment is significant. The processes affecting rock glaciers kinematic behaviour, which is rapidly changing under the changing climate, their internal structure, and their hydrological significance in mountain catchments are investigated with different methods and combining different types of data.

Results have shown that high resolution datasets composed by multitemporal DSMs and orthoimages, and high-dense point clouds are powerful tools for investigating with high detail the geomorphic changes of rock glaciers. As these permafrost-related landforms are often located in impervious environments, UAV-based surveys are certainly a valuable tool to investigate the temporal evolution of these landforms. As demonstrated in the thesis, the use of UAV products over traditional GNSS techniques has a double advantage. Drone-base data allow both to reach otherwise inaccessible or dangerous areas and to investigate elevation changes and surface displacements of a rock glacier with comparable accuracy of GNSS measurements. UAV products can also be used for preliminary analyses on the study of the destabilisation state of rock glaciers, identifying sectors or areas at a greater risk of collapse and consequently allowing targeted interventions to be planned to minimise the natural hazards that could be triggered as a result. In fact, the destabilisation phase of a rock glacier can assess

using only drone-base derived products to define the Bulk Creep Factor (BCF), which can be applied and extended over large areas. The BCF is a dimensionless factor which allows to separate the two contributions of the surface velocity from material properties and geometry of a rock glacier. The proposed approach only requires remote sensing data on creep velocities and surface slope angle, both which can be derived operationally from UAV-based surveys.

By combining drone products and in-situ investigations, the rock glacier dynamics and the effects of the hydrological mechanism on its short-term velocity changes can be assessed. Rock glaciers chemically and physically influence the water that passes through them, affecting the water quality of rivers and water body located downstream with strongly consequences on ecological and water management issues. For these reasons, hydrological studies on rock glacier such as discharge rates, salt and dye injections, which are seldom methods applied on rock glaciers due to their complexity, need to be further investigated in the next years in view of warming climate conditions.

To achieve these goals, 3D approaches and point-cloud comparisons were computed to map the temporal and spatial distribution of velocity patterns of the Gran Sometta rock glacier. Successively, ground surface temperature and meteorological variables were investigated to set the degradation phase of permafrost within the rock glacier (Chapter 2). An image correlation algorithm was instead used to create maps of horizontal surface velocities of the Plator rock glacier, which were then interpreted using the spatial BCF variability to define long-term rock glacier dynamics in terms of destabilisation state (Chapter 3). The seasonal hydrological influence of an active rock glacier on the mainstream of an Alpine periglacial catchment was presented in Chapter 4.

These results could be potentially extended to other rock glaciers with similar characteristics and size, which are common in many mountain ranges. The main outcomes of each chapter are summarised below.

Chapter 2: KINEMATICS OF AN ALPINE ROCK GLACIER FROM MULTI-TEMPORAL UAV SURVEYS AND GNSS DATA

The interannual variations in surface velocities of the Gran Sometta rock glacier were quantified. They are in line with the trend observed in other Alpine rock glaciers i.e., maximum peak of surface velocity in 2015, followed by a decreasing phase until 2017-2018 and then a gradual increase in surface velocity until 2021.

The observed rates of thaw subsidence at the margins of the landform, in the range of centimetres per year, are characteristic for ice-rich rock glaciers. The heterogeneous distribution of frozen ground at depth, its structure, and the topographical settings seem to be key factors explaining the observed spatial flow pattern. MAGST, GFI and WEqT values are directly related to the annual kinematics of the rock glacier. Increases in permafrost creep rates (in 2014-2015, 2018-2019 and 2019-2020) respond to higher MAGST values while a deceleration phase occurred with lower MAGST values as in 2015-2016, 2016-2017 and 2017-2018. In addition, GFI and WEqT values higher than -0.6°C and -1.4°C, respectively, generally correspond to high surface displacement rates.

The investigated permafrost appears to be in imbalance with the current climatic conditions and the subsurface ice, documented by the ERT profiles, is close to melting conditions.

Chapter 3: FLOW VELOCITY VARIATIONS AND SURFACE CHANGE OF THE DESTABILISED PLATOR ROCK GLACIER (CENTRAL ITALIAN ALPS) FROM AERIAL SURVEYS

Chapter 3 aimed at mapping the temporal-spatial distribution of the surface velocities of the rock glacier using an image correlation algorithm. Successively, the horizontal surface velocities over time are discussed in relation to the spatial and temporal BCF variability as a measure of the rheological properties of rock glaciers, which are used to interpret long-term evolution of the dynamics of the landform.

On the Plator rock glacier, the heterogeneous velocity patterns between the upper (very low velocity, < 1 m/y) and the lower (high velocity, up to > 4 m/y) parts combined with high and discontinuous BCFs throughout the entire landform and the continuous development of the scarp #2 are clearly signs of ongoing destabilisation processes. During the investigated period (from 2012 until 2020), the indicative mean BCF values of each zone of the rock glacier increased due to increasing flow velocities. The highest BCFs (>16) found in the toe zone and the discontinuous spatio-temporal distribution of the BCFs throughout the rock glacier indicate that the Plator is experiencing a destabilisation phase.

Chapter 4: HYDROLOGICAL INFLUENCE OF AN ACTIVE ROCK GLACIER ON STREAM FLOW IN AN ALPINE CATCHMENT

Chapter 4 aimed to understand the hydrological influence of an intact rock glacier in a stream flow of an Alpine periglacial catchment.

The rock glacier analysed contains hydrologically valuable perennially frozen layers which, under future climate warming conditions, could affect the mountain hydrology, increasing the flow of the main stream (Pousset River) draining the area.

The released water derives from snowpack and rock glacier ice melting, with contributions from rainfall and groundwater. Discharge rates, EC data, water temperature, and artificial dye tracers are successfully used to describe the seasonal evolution of the discharge and asses the influence of the Gran Sometta rock glacier on the Pousset River. The analysis highlighted the hydrological relevance of the rock glacier on water storage capabilities. Despite covering only 34% of the total catchment area, the relative hydrological contribution of the rock glacier on the Pousset River reached 65% in September-October, suggesting the important role of the rock glacier as a water storage, especially in those periods when the contribution of snow melt is reduced or absent. Using the EC into a simple two-component mixing model, it was possible to estimate the hydrochemical contribution of the rock glacier on the stream. The rock glacier contribution is lowest in early summer (48%) due to the high amount of quickflow derived from snowmelt, and successively increases towards early autumn (63%) due to the reduction of the snow contribution and the increase in meltwater contribution from internal ice and groundwater. The cold water discharge of the rock glacier suggests that the water flows is in direct contact with ground ice or permafrost, and has the ability to lower the average stream water temperature by ca. 2.8 °C.

5.2 Perspectives and future research

Based on the results obtained from this research, other study paths can be considered to increase our knowledge of rock glacier dynamics such as:

- Develop 3D models accounting for complex transient effects;
- Connect thermo-hydro-mechanical parameters and their interaction with the creep behaviour of rock glaciers;
- Validate the spatial BCF variability results with detailed field surveys and in-situ measurements;
- Investigate the possibility to set destabilisation state of rock glaciers only from remote sensing products and the rheological properties of rock glaciers material on larger scale;
- Increase our understanding about the effect of the relationship between dynamics, geometric changes and hydrology of rock glaciers and meteorological forcing at longer time scales;
- Create a unique dataset collecting several information on surface velocity, hydrological component, GST, and geophysical prospections on several study sites.
- Since a no comprehensive rock glacier inventory on a global scale has been completed so far, it is necessary to update the exist knowledge about rock glaciers around the world into a unique rock glaciers inventory.
- Rock glacier inventories are required to also understand the hydrological significance of these landforms, especially considering the considerable impact that future climate warming will have on long-term freshwater resources.

Bibliography

Anthony, K.M.W., Anthony, P., Grosse, G., Chanton, J., 2012. Geologic methane seeps along boundaries of Arctic permafrost thaw and melting glaciers. Nature Geoscience, 5(6), 419.426.

Arenson, L., Kääb, A., O'Sullivan, A., 2016. Detection and analysis of ground deformation in permafrost environments. Permafrost and Periglacial Processes, 27, 339-351.

Arenson, L., Hoelzle, M., Springman, S., 2002. Borehole deformation measurements and internal structure of some rock glaciers in Switzerland. Permafrost and Periglacial Processes, 13(2), 117-135. Doi: 10.1002/ppp.414.

Barsch, D., 1992. Permafrost creep and rock glaciers. Permafrost and Periglacial Processes, 3.3, 175-188. Doi: 10.1002/ppp.3430030303.

Bauer, A., Paar, G., Kaufmann, V., 2003. Terrestrial laser scanning for rock glacier monitoring. Permafrost, Phillips, Springman & Arenson (Eds).

Bearzot, F., Garzonio, R., Di Mauro, B., Colombo, R., Cremonese, E., Crosta, G.B., Delaloye, R., Hauck, C., Morra Di Cella, U., Pogliotti, P., Frattini, P., Rossini, M., 2022. Kinematics of an Alpine rock glacier from multi-temporal UAV surveys and GNSS data. Geomorphology, 2022. Doi: 10.1016/j.geomorph.2022.108116.

Bennet, M.R., 2001. The morphology, structural evolution and significance of push moraines. Earth Science Reviews, 53, 197-236.

Berthling, I., 2011. Beyond confusion: Rock glaciers as cryo-conditioned landforms. Geomorphology, 131(3-4), 98-106.

Biskaborn, B.K., Smith, S.L., Noetzli, J., Matthes, H., Vieira, G., Streletskiy, D.A. et al., 2019. Permafrost is warming at a global scale. Nat. Commun., 10 (264). Doi: 10.1038/s41467-018-08240-4.

Bodin, X., Thibert, E., Sanchez, O., Rabatel, A., Jaillet, S., 2018. Multi-annual kinematics of an active rock glacier quantified from very high-resolution DEMs: an application-case in the French Alps. Remote Sensing, 10, 547. Doi: 10.3390/rs10040547.

Bodin, X., Krysiecki, J.M., Schoeneich, P., Le Roux, O., Lorier, L., Echelard, T. et al., 2017. The 2006 collapse of the Bérard rock glacier (Southern French Alps): Permafrost and Periglacial Processes, 209-223. https://doi.org/10.1002/ppp.1887.

Bodin, X., Schoeneich, P., Deline, P., Rayanel, L., Magnin, F., Krysiecki, J.M., Echelard, T., 2015. Mountain permafrost and associated geomorphological processes: recent changes in the French Alps. J. Alp. Res., 103. Doi: 10.4000/rga.2885.

Boeckli, L., Brenning, A., Gruber, S., Noetzli, J., 2012. Permafrost distribution in the European Alps: calculation and evaluation of an index map and summary statistics. The Cryosphere, 6, 807-820.

Bollmann, E., Klug, C., Sailer, R., Stötter, J., 2012. Quantifying rock glacier creep using airborne laser scanning: a case study from two rock glaciers in the Austrian Alps. Tenth International Conference on Permafrost (Salekhard, Russia), volume 1. Doi: 10.13140/RG.2.1.3249.5202.

Bonnaventure, P.P., Lamoureux, S.F., 2013. The active layer: A conceptual review of monitoring, modelling techniques and changes in a warming climate. Prog. Phys. Geogr., 37, 352-376. Doi: 10.1177/0309133313478314.

Bosson, J.B., Lambiel, C., 2016. Internal structure and current evolution of very small debris-covered glacier system located in alpine permafrost environments. Front. Earth Sci., 4(39).

Brighenti, S., Hotaling, S., Finn, D.S., Fountain, A.G., Hayashi, M., Herbst, D., Saros, J.E., Tronstad, L.M., Millar, C.I. et al., 2021. Rock glaciers and related cold rocky landforms: Overlooked climate refugia for mountain biodiversity. Global Change Biology, 27(8), 1504-1517. https://doi.org/10.1111/gcb.15510.

Buchli, T., Kos, A., Limpach, P., Merz, K., Zhou, X., Springman, S.M., 2018. Kinematic investigations on the Furggwanghorn rock glacier, Switzerland. Permafrost and Periglacial Processes, 29, 3-20. Doi: 10.1002/ppp.1968.

Buchli, T., Merz, K., Zhou, X., Kinzelbach, W., Springman, S.M., 2013. Characterization and monitoring of the Furggwanghorn rock glacier, Turtmann Valley, Switzerland: results from 2010 to 2012. Vadose Zone Journal, 12. Doi: 10.2136/vzj2012.0067.

Chadburn, S., Burke, E., Cox, P., Friedlingstein, P., Hugelius, C., Westermann, S., 2017. An observation-based constraint on permafrost loss as a function of global warming. Nature Climate Change, 7, 340-344.

Cicoira, A., Marcer, M., Gärtner-Roer, I., Bodin, X., Arenson, L., Vieli, A., 2021. A general theory of rock glacier creep based on in-situ and remote sensing observations. Permafrost and Periglacial Processes, 32, 139-153. Doi: 10.1002/ppp.2090.

Cicoira, A., Beutel, J., Faillettaz, J., Gärtner-Roer, I., Vieli, A., 2019a. Resolving the influence of temperature forcing through heat conduction on rock glacier dynamics: a numerical modelling approach. The Cryosphere, 13, 927-942. https://doi.org/10.5194/tc-13.927-2019.

Cicoira, A., Beutel, J., Faillettaz, J., Vieli, A., 2019b. Water controls the seasonal rhythm of rock glacier flow. Earth and Planetary Science Letters, 528. https://doi.org/10.1016/j.epsl.2019.115844.

Clapuyt, F., Vanacker, V., Van Oost, K., 2016. Reproducibility of UAV-based earth topography reconstructions based on Stucture-from-Motion algorithms. Geomorphology, 260, 4-15.

Clark, D.H., Steig, E.G., Potter Jr, N., Fitzpatrick, J., Updike, A.B., Clark, M.G., 1996. Old ice in rock glaciers may provide long-term climate records. Eos, 77, 217-222.

Colomina, I., Molina, P., 2014. Unmanned aerial systems for photogrammetry and remote sensing: A review. ISPRS Journal of Photogrammetry and Remote Sensing, 92, 79-97.

Corte, A.E., 1976. The hydrological significance of rock glaciers. J. Glaciol., 17, 157-158.

Cremonese, E., Gruber, S., Phillips, M., Pogliotti, P., Boeckli, L., Noetzli, J., Suter, C., Bodin, X., Crepaz, A., Kellerer-Pirklbauer, A., Lang, K., Letey, S., Mair, V., Morra Di Cella, U., Ravanel, I., Scapozza, C., Seppi, R., Zischg, A., 2011. Brief communication: "An inventory of permafrost evidence for the European Alps". The Cryosphere, 5, 651-657. Doi: 10.5194/tc-5-651-2011.

Cusicanqui, D., Rabatel, A., Vincent, C., Bodin, X., Thibert, E., Francou, B., 2021. Interpretation of volume and flux changes of the Laurichard rock glacier between 1952 and 2019, French Alps. J. Geophys. Res. Earth Surf., 126. Doi: 10.1029/2021JF006161.

Dall'Asta, E., Forlani, G., Roncella, R., Santise, M., Diotri, F., Morra di Cella, U., 2017. Unmanned aerial systems and DSM matching for rock glacier monitoring. ISPRS Journal of Photogrammetry and Remote Sensing, 127, 102-114. http://dx.doi.org/10.1016/j.isprsjprs.2016.10.003.

Debella-Gilo, M., Kääb, A., 2011. Sub-pixel precision image matching for measuring surface displacements on mass movements using normalized cross-correlation. Remote Sensing of Environment, 115, 130-142.

Delaloye, R., Barboux, C., Morard, S., Abbet, D., Gruber, V., 2013. Rapidly moving rock glaciers in Mattertal. In: Graf C (ed) Mattertal - ein Tal in Bewegung. Publikation zur Jahrestagung der Schweizerischen Geomorphologischen Gesellschaft, St. Niklaus, pp 21–31.

Delaloye, R., Morard, S., Barboux, C., Abbet, D., Gruber, V., Riedo, M., Gachet, S., 2011. Rapidly moving rock glacier in Mattertal. In Jahrestagung Der Schweizerischen Geomorphologischen Gesellschaft, St. Niklaus, Switzerland, 29 June-1 July 2011, 21-31.

Delaloye, R., Lambiel, C., Gärtner-Roer, I., 2010. Overview of rock glacier kinematics research in the Swiss Alps. Geographica Helvetica, 65, pp 135-145. Doi: 10.5194/gh-65-135-2010.

Delaloye, R., Lambiel, C., 2008. Typology of vertical electrical soundings for permafrost/ground ice investigation in the forefields of small alpine glaciers. In: Hauck, C., Kneisel, C. (eds), Applied Geophysics in Periglacial Environments, Cambridge University Press, 101-108.

Delaloye, R., Perruchoud, E., Avian, M., Kaufmann, V., Bodin, X., Hausmann, H., Ikeda, A., Kääb, A., Kellerer-Pirklbauer, A., Krainer, K., Lambiel, C., Mihailovic, D., Staub, B., Roer, I., Thibert, E., 2008. Recent interannual variations of rock glacier creep in the European Alps. In: Kane, D.L., Hinkel, K.M. (Eds.). 9th International Conference on Permafrost Fairbanks, Alaska, 343-348.

Dusik, J.M., Leopold, M., Heckmann, T., Haas, F., Hilger, L., Morche, D., Neugirg, F., Becht, M., 2015. Influence of glacier advance on the development of the multipart Riffeltal rock glacier, Central Austrian Alps. Earth Surf. Process. Landforms, 40, 965-980. Doi: 10.1002/esp.3695.

Duvillard, P.A., Ravanel, L., Marcer, M., Schoeneich, P., 2019. Recent evolution of damage to infrastructure on permafrost in the French Alps. Regional Environmental Change, 19, 1281-1293.

Endrizzi, S., Gruber, S., Dall'Amico, M., Rigon, R., 2014. GEOtop 2.0: simulating the combined energy and water balance at and below the land surface accounting for soil freezing, snow cover and terrain effects. Geoscientific Model Development, 7(6), 2831-2857.

Eriksen, H.Ø., Rouyet, L., Lauknes, T.R., Berthlig, I., Isaksen, K., Hindberg, H., Larsen, Y., Corner, G.D., 2018. Recent acceleration of a rock glacier complex, Ádjet, Norwey, Documented by 62 years of remote sensing observations. Geophysical Research Letters, 45, 8314-8323. https://doi.org/10.1029/2018GL077605.

Etzelmüller, B., Guglielmin, M., Hauck, C., Hilbich, C., Hoelzle, M., Isaksen, K., Noetzli, J., Oliva, M., Ramos, M., 2020. Twenty years of European mountain permafrost dynamics – the PACE legacy. Environmental Research Letters, 15, 104070. https://doi.org/10.1088/1748-9326/abae9d.

Fahnestock, M.A., Scambos, T.A., Bindschadler, R.A., 1992. Semi-automated ice velocity determination from satellite imagery. Eos, 73, 493.

Fey, C., Krainer, K., 2020. Analyses of UAV and GNSS based flow velocity variations of the rock glacier Lazaun (Ötztal Alps, South Tyrol, Italy). Geomorphology, 365. https://doi.org/10.1016/j.geomorph.2020.107261.

Fey, C., Rutzinger, M., Wichmann, V., Prager, C., Bremer, M., Zangerl, C., 2015. Deriving 3D displacement vectors from multi-temporal airborne laser scanning data for landslide activity analyses. GIScience & Remote Sensing, 52 (4), 437-461. Doi: 10.1080/15481603.1045278.

Fonstad, M.A., Dietrich, J.T., Courville, B.C., Jensen, J.L., Carbonneau, P.E., 2013. Topographic structure from motion: a new development in photogrammetric measurement. Earth Surface Processes and Landforms, 38(4), 421-430.

Frauenfelder, R., Schneider, B., Kääb, A., 2008. Using dynamic modeling to simulate the distribution of rock glaciers. Geomorphology, 93, 130-143. Doi: 10.1016/j.geomorph.2006.12.023.

Frauenfelder, R., Kääb, A., 2000. Towards a paleoclimatic model of rock-glacier formation in the Swiss Alps. Annals of Glaciology, 31, 281-286. Doi: 10.3189/172756400781820264.

Frehner, M., Ling, A.H.M., Gärtner-Roer, I., 2015. Furrow-and-ridge morphology on rock glaciers explained by gravity-driven buckle folding: a case

study from the Murtèl rock glacier (Switzerland). Permafrost and Periglacial Processes, 26, 57-66. Doi: 10.1002/ppp.1831.

Gobiet, A., Kotlarski, S., Beniston, M., Heinrich, G., Rajczak, J., Stoffel, M., 2014. 21st century climate change in the European Alps-A review. Science of the Total Environment, 493, 1138-1151. http://dx.doi.org/10.1016/j.scitotenv.2013.07.050.

Goetz, J., Brenning, A., Marcer, M., Bodin, X., 2018. Modeling the precision of structure-from-motion multi-view stereo digital elevation models from repeated close-range aerial surveys. Remote Sensing of Environment, 210, 208-216. https://doi.org/10.1016/j.rse.2018.03.013.

Haberkorn, A., Kenner, R., Noetzli, J., Phillips, M., 2021. Changes in ground temperature and dynamics in mountain permafrost in the Swiss Alps. Front. Earth Sci., 9, 626686. Doi: 10.3389/feart.2021.626686.

Haeberli, W., Schaub, Y., Huggel, C., 2017. Increasing risks related to landslides from degrading permafrost into new lakes in de-glaciating mountain ranges. Geomorphology, 293, 405-417.

Haeberli, W., Noetzli, J., Arenson, L., Delaloye, R., Gärtner-Roer, I., Gruber, S., Isaksen, K., Kneisel, C., Krautblatter, M., Phillips, M., 2010. Mountain permafrost: development and challenges of a young research field. Journal of Glaciology, 56 (200), 1043-1058. Doi: 10.3189/002214311796406121.

Haeberli, W., Hallet, B., Arenson, L., Elconin, R., Humlum, O., Kääb, A., Kaufmann, V., Ladanyi, B., Matsuoka, N., Springman, S., Vonder Mühll, D., 2006. Permafrost creep and rock glacier dynamics. Permafrost and Periglacial Processes, 17/3, 189-241. Doi: 10.1002/ppp561.

Haeberli, W., Kääb, A., Wagner, S., Mühll, D.V., Geissler, P., Haas, J.N., Glatzel-Mattheier, H., Wagenbach, D., 1999. Pollen analysis and 14C age of moss remains in a permafrost core recovered from the active rock glacier Murtél-Corvatsch, Swiss Alps: geomorphological and glaciological implications. Journal of Glaciology, 45, 1-8.

Haeberli, W., Beniston, M., 1998. Climate change and its impacts on glaciers and permafrost in the Alps. Ambio, 27, 258-265.

Haeberli, W., Vonder Mühll, D., 1996. On the characteristics and possible origins of ice in rock glacier permafrost. Zeitschrift für Geomorphologie N.F., 104, 43-57.

Haeberli, W., 1985. Creep of mountain permafrost: internal structure and flow of alpine rock galciers. Mitteilingen der Versuchsanstalt für Wasserbau. Hydrologie und Glaziologie an der Eidgenössischen Technischen Hochschule Zürich, 77, 142 pp.

Haeberli, W., 1979. Holocene push-moraines in Alpine permafrost. Geografiska Annaler, 61A, 43-48. Doi: 10.2307/520513.

Harris, C., Mühll, D.V., Isaksen, K., Haeberli, W., Sollid, J.L., King, L., Holmlund, P., Dramis, F., Guglielmin, M., Palacios, D., 2003. Warming permafrost in European mountains. Global and Planetary Change, 39, 215-225.

Hartl, L., Fischer, A., Stocker-Waldhuber, M., Abermann, J., 2016. Recent speed-up of an alpine rock glacier: an updated chronology of the kinematics of Outer Hochebenkar rock glacier based on geodetic measurements. Geografiska Annaler: Series A, Physical Geography, 98, 129-141. https://doi.org/10.1111/geoa.12127.

Hausmann, H., Krainer, K., Brückl, E., Ullrich, C., 2012. Internal structure, ice content and dynamics of Ölgrube and Kaiserberg rock glaciers (Ötztal Alps, Austria) determinated from geophysical surveys. Austrian J. Earth Sci., 105, 12-31.

Heid, T., Kääb, A., 2012. Evaluation of existing image matching methods for deriving glacier surface displacements globally from optical satellite imagery. Remote Sensing of Environment, 118, 339-355.

Hendrickx, H., Vivero, S., De Cock, L., De Wit, B., De Maeyer, P., Lambiel, C., Delaloye, R., Nyssen, J., Frankl, A., 2019. The reproducibility of SfM algorithms to produce detailed Digital Surface Models: an example of PhotoScan applied to a high-alpine rock glacier. Remote Sensing Letters, 10(1), 11-20. Doi: 10.1080/2150704X.2018.1519641.

Humlum, O., 1998. The climatic significance of rock glaciers. Permafrost and Periglacial Processes, 9, 375-395.

Ikeda, A., Matsuoka, N., Kaab, A., 2008. Fast deformation of perennially frozen debris in a warm rock glacier in the Swiss Alps: An effect of liquid water. J. Geophys. Res., 113(F1). https://doi.org/10.1029/2007JF000859.

IPA – IPA Action Group Rock glacier inventories and kinematics, 2020. Baseline concepts towards standard guidelines for inventorying rock glaciers, v. 4.1, 1-12.

James, M.R., Robson, S., 2014. Mitigating systematic error in topographic models derived from UAV and ground-based images networks. Earth Surf. Process. Landforms, 39, 1413-1420. Doi: 10.1002/esp.3609.

Jansen, F., Hergarten, S., 2006. Rock glacier dynamics: stick-slip motion coupled to hydrology. Geophys Res Lett., 33(10), L105205. Doi: 10.1029/2006GL026134.

Jones, D.B., Harrison, S., Anderson, K., Whalley, W.B., 2019. Rock glaciers and mountain hydrology. A review. Earth-Science Reviews, 193, 66-90. https://doi.org/10.1016/j.earscirev.2019.04.001.

Jones, D.B., Harrison, S., Anderson, K., Betts, R.A., 2018. Mountain rock glaciers contain globally significant water stores. Scientific Reports, 8, 2834. Doi: 10.1038/s41598-018-21244-w.

Kääb, A., Strozzi, T., Bolch, T., Caduff, R., Trefall, H., Stoffel, M., Kokarev, A., 2021. Inventory and changes of rock glacier creep speeds in Ile Alatau and

Kungöy Ala-Too, northern Tien Shan, since the 1950s. The Cryosphere, 15, 927-949. https://doi.org/10.5194/tc-15-927-2021.

Kääb, A., Frauenfelder, R., Roer, I., 2007. On the response of rockglacier creep to surface temperature increase. Global Planet. Change, 56, 172-187. Doi: 10.1016/j.geoplacha.2006.07.005.

Kääb, A., Girod, L., Berthling, I., 2014. Surface kinematics of periglacial sorted circles using structure-from-motion technology. Remote Sensing of Environment, 94(4), 463-474.

Kääb, A., 2002. Monitoring high-mountain terrain deformation from repeated air- and spaceborne optical data: examples using digital aerial imagery and ASTER data. ISPRS Journal of Photogrammetry & Remote Sensing, 57, 39-52.

Kääb, A., Vollmer, M., 2000. Surface geometry, thickness changes and flow on creeping mountain permafrost: automatic extraction by Digital Image Analysis. Permafrost and Periglacial Processes, 11, 315-326.

Kaufmann, V., Seier, G., Sulzer, W., Wecht, M., Liu, Q., Lauk, G., Maurer, M., 2018. Rock glacier monitoring using aerial photographs: conventional vs. UAV-based mapping – a comparative study. The International Archives of the Photogrammetry, Remote Sensing and Spatial Information Sciences, Volume XLII-1.

Kaufmann, V., Ladstädter, R., 2003. Quantitative analysis of rock glacier creep by means of digital photogrammetry using multi-temporal aerial photographs:

two case studies in the Austrian Alps. In: Arenson,S. (Ed.), 8th International Conference on Permafrost.

Kellerer-Pirklbauer, A., Delaloye, R., Lambiel, C., 2018. Interannual variability of rock glacier flow velocities in the European Alps. 5th European Conference on Permafrost. Edytem: Chamonix Mont-Blanc, 396-397.

Kellerer-Pirklbauer, A., Lieb, G.K., Kaufmann, V., 2017. The Dösen rock glacier in central Austria: a key site for multidisciplinary long-term rock glacier monitoring in the Eastern Alps. Austrian Journal of Earth Sciences, 110/2. Doi: 10.17738/ajes.2017.0013.

Kellerer-Pirklbauer, A., Kaufmann, V., 2012. About the relationship between rock glacier velocity and climate parameters in central Austria. Austrian Journal of Earth Sciences, 105/2, 94-112.

Kenner, R., Bühler, Y., Delaloye, R., Ginzler, C., Phillips, M., 2014. Monitoring of high alpine mass movements combining laser scanning with digital airborne photogrammetry. Geomorphology, 206, 492-504. Doi: 10.1016/j.geomorph.2013.10.020.

Kenner, R., Phillips, M., Beutel, J., Hiller, M., Limpach, P., Pointner, E., Volken, M., 2017. Factors controlling velocity variations at short-term, seasonal and multiyear time scales, Ritigraben rock glacier, Western Swiss Alps. Permafrost Periglac., 28, 675-684.

Kenner, R., Pruessner, L., Beutel, J., Limpach, P., Phillips, M., 2019. How rock glacier hydrology, deformation velocities and ground temperatures interact: examples from the Swiss Alps. Permafrost and Periglacial Processes, 31(1), 3-14. https://doi.org/10.1002/ppp.2023.

Klug, C., Bollmann, E., Sailer, R., Stötter, J., 2012. Monitoring of permafrost creep on two rock glaciers in the Austrian Eastern Alps: combination of aerophotogrammetry and airborne laser scanning. In 10th International Conference of Permafrost, Salekhard, Russia, 2012, Vol. 1, 215-220. Doi: 10.13140/RG.2.1.1807.7284.

Kneisel, C., Kääb, A., 2007. Mountain permafrost dynamics within a recently exposed glacier forefield inferred by a combined geomorphological, geophysical and photogrammetrical approach. Earth Surface Processes and Landforms, 32(12), 1797-1810. Doi: 10.1002/esp.1488.

Kofler, C., Mair, V., Gruber, S., Todisco, M.C., Nettleton, I., Steger, S., Zebisch, M., Schneiderbauer, S., Comiti, F., 2021. When do rock glacier fronts fail? Insights from two case studies in South Tyrol (Italian Alps). Earth Surface Processes and Landforms, 46(7), 1311-1327. https://doi.org/10.1002/esp.5099.

Kofler, C., Steger, S., Mair, V., Zabisch, M., Comiti, F., Schneiderbauer, S., 2020. An inventory-driven rock glacier status model (intact vs. relict) for South Tyrol, Eastern Italian Alps. Geomorphology, 350. https://doi.org/10.1016/j.geomorph.2019.106887.

Krainer, K., Bressen, D., Dietre, B., Haas, J., Hajdas, I., Lang, K., Mair, V., Nickus, U., Reidl, D., Thies, H., Tonidanel, D., 2015. A 10,300 year-old permafrost core from the active rock glacier Lazaun, southern Öutztal Alps (South Tyrol, northern Italy). Quaternary Research, 83, 324-335.

Krainer, K., Mostler, W., Spötl, C., 2007. Discharge from active rock glaciers, Austrian Alps: A stable isotope approach. Austrian Journal of Earth Sciences, 100, 102-112.

Krainer, K., Mostler, W., 2006. Flow velocities of active rock glaciers in the Austrian Alps. Geogr. Ann., 88, 267-280.

Kummert, M., Delaloye, R., 2018. Mapping and quantifying sediment transfer between the front of rapidly moving rock glaciers and torrential gullies. Geomorphology, 309, 60-76.

Kummert, M., Delaloye, R., Braillard, L., 2017. Erosion and sediment transfer processes at the front of rapidly moving rock glaciers: systematic observations with automatic cameras in the western Swiss Alps. Permafrost and Periglacial Processes, 1-17. Doi: 10.1002/ppp.1960.

Lague, D., Brodu, N., Leroux, J., 2013. Accurate 3D comparison of complex topography with terrestrial laser scanner: application to the Rangitikei canyon (N-Z). ISPRS J. Photogramm. Remote Sens., 82, 10–26.

Lambiel, C., Delaloye, R., 2004. Contribution of real-time kinematic GPS in the study of creeping mountain permafrost: examples from the Western Swiss Alps. Permafr. Periglac. Process., 15(3), 229-241.

Loke, M.H., 2020. RES2DINV ver. 4.10 Rapid 2-D Resistivity and IP Inversion using the Least-Square Method, User Manual.

Lucieer, A., De Jong, S.M., Turner, D., 2014. Mapping landslide displacements using Structure from Motion (SfM) and image correlation of multi-temporal UAV photography. Progress in Physical Geography, 38(1), 97-116. Doi: 10.1177/0309133313515293.

Marcer, M., Cicoira, A., Cusicanqui, D., Bodin, X., Echelad, T., Obregon, R., Schoeneich, P., 2021. Rock glaciers throughout the French Alps acceleration and destabilised since 1990 as air temperatures increased. Communications earth & environment, 2(81). https://doi.org/10.1038/s43247-021-00150-6.

Marcer, M., Serrano, C., Brenning, A., Bodin, X., Goetz, J., Schoeneich, P., 2019. Evaluating the destabilization susceptibility of active rock glaciers in the French Alps. The Cryosphere, 13, 141-155. https://doi.org/10.5194/tc-13-141-2019.

Martin, H.E., Whalley, W.B., 1987. Rock glaciers. Part 1: Rock glacier morphology, classification, and distribution. Progress in Physical Geography, 11, 260-282. Doi: 10.1177/030913338701100205.

Millar, C.I., Westfall, R.D., Delany, D.I., 2013. Thermal and hydrologic attributes of rock glaciers and periglacial talus landforms: Sierra Nevada, California, USA. Quat. Int., 310, 169-180.

Mollaret, C., Hilbich, C., Pellet, C., Flores-Orozco, A., Delaloye, R., Hauck, C., 2019. Mountain permafrost degradation documented through a network of permanent electrical resistivity tomography sites. The Cryosphere, 13, 2557-2578. https://doi.org/10.5194/tc-13-2557-2019.

Müller, J., Vieli, A., Gärtner-Roer, I., 2016. Rock glaciers on the run – understanding rock glacier landform evolution and recent changes from numerical flow modelling. The Cryosphere, 10, 2865-2886. Doi: 10.5194/tc-10-2865-2016.

Nex, F., Remondino, F., 2014. UAV for 3D mapping applications: a review. Applied Geomatics, 6(1), 1-15.

Penna, D., van Meerveld, H.J., 2019. Spatial variability in the isotopic composition of water in small catchments and its effect on hydrograph separation. Wiley Interdisciplinary Reviews Water, 6(5). https://doi.org/10.1002/wat2.1367.

PermaNET, 2011. Guide lines for monitoring GST – Ground surface temperature. Permafrost Monitoring Network, V. 3 by P. Schoeneich.

PermaNET, 2011. Guide lines for monitoring BTS – Bottom temperature of snow cover. Permafrost Monitoring Network, V. 2 by P. Schoeneich.

PERMOS, 2019. Permafrost in Switzerland 2014/2015 to 2017/2018. Noetzli, J., Pellet, C., Staub, B. (Eds.), Glaciological Report (Permafrost), 16-19 of the Cryospheric Commission of the Swiss Academy of Sciences, 104 pp. Doi: 10.13093/permos-rep-2019-16-19.

PERMOS, 2016. Permafrost in Switzerland 2010/2011 to 2013/2014. Noetzli, J., Luethi, R., Staub, B. (Eds.), Glaciological Report (Permafrost), 12-15 of the Cryospheric Commission of the Swiss Academy of Sciences, 85 (2016).

Piermattei, L., Carturan, L., De Blasi, F., Tarolli, P., Dalla Fontana, G., Vettore, A., Pfeifer, N., 2016. Suitability of ground-based SfM-MVS for monitoring glacial and periglacial processes. Earth Surf. Dynam., 4, 425-443.

Rangecroft, S., Suggitt, A.J., Anderson, K., Harrison, S., 2016. Future climate warming and changes to mountain permafrost in the Bolivian Andes. Climatic Change, 137, 231-243.

Reynard, E., Delaloye, R., Baron, L., Chapellier, D., Devaud, G., Lambiel, C., Marescot, L., Monnet, R., 2003. Glacier/permafrost relationship in recently deglaciated forefields of small glaciers, Penninic Alps, Valais, Western Switzerland. Proceedings of the 8th International Conference on Permafrost, Zurich 2003, Vol. 1, 947-952.

Rock, G., Ries, J.B., Udelhoven, T., 2011. Sensitivity analysis of UAV-photogrammetry for creating Digital Elevation Models (DEM). In Proceedings

of Conference on Unmanned Aerial Vehicle in Geomatics, 14-16 September 2011, Zürich, Switzerland, 2011, 1-5.

Roer, I., Haeberli, W., Avian, M., Kaufmann, V., Delaloye, R., Lambiel, C., Kääb, A., 2008. Observations and considerations on destabilizing active rock glaciers in the European Alps. In 9th International Conference on Permafrost, Fairbanks, Alaska, 29 June-3 July 2008, 1505-1510.

Rossini, M., Di Mauro, B., Garzonio, R., Baccolo, G., Cavallini, G., Mattavelli, M., De Amicis, M. and Colombo, R., 2018. Rapid melting dynamics of an alpine glacier with repeated UAV photogrammetry. Geomorphology, 304, pp.159-172. Doi: 10.1016/j.geomorph.2017.12.039.

Sanz-Ablanedo, E., Chandler, J.H., Ballesteros-Pérez, P., Rodriguez-Pérez, J.R., 2020. Reducing systematic dome errors in digital elevation models through better UAV flight design. Earth Surf. Process. Landforms, 45, 2134-2147. Doi: 10.1002/esp.4871.

Scapozza, C., Colombo, L., Domenici, M., Lepori, F., Pera, S., Pozzoni, M., Rioggi, S., Bruder, A., 2017. Lago Nero – an example of mountain lake monitoring in a changing Alpine cryosphere. Report on National ICP IM activities in Switzerland, Annex I. reports of the Finnish Environment Institute, 24, 43-49.

Schoeneich, P., Ribeyre, C., Marcer, M., Bodin, X., Brenguier, O., 2015. Etude géomorphologique et géophysique du glacier rocheux du Col du Lou suite à la

lave torrentielle du 14 août 2015. Technical report, Universitéof Grenoble-Alpes, Grenoble, France, 42 pp.

Schoeneich, P., Bodin, X., Echelard, T., Kaufmann, V., Kellerer-Pirklbauer, A., Krysiecki, J.M., Lieb, G.K., 2014. Velocity changes of rock glaciers and induced hazards. Engineering Geology for Society and Territory, 1, 223-227.

Schuur, E.A.G., et al., 2015. Climate change and the permafrost carbon feedback. Nature, 520, 171-179.

Schuur, E.A.G., Bockheim, J., Canadell, J.G., Euskirchen, E., Field, C.B., Goryachkin, S.V., Hagemann, S., Kuhry, P., Lafleur, P.M., Lee, H., Mazhitova, G., Nelson, F.E., Rinke, A., Romanovsky, V.E., Shiklomanov, N., Tarnocai, C., Venevsky, S., Vogel, J.G., Zimov, S.A., 2008. Vulnerability of permafrost carbon to climate change: Implications for the Global Carbon Cycle. BioScience, 58(8), 701.

Scotti, R., Crosta, G.B., Villa, A., 2017. Destabilization of creeping permafrost: the Plator rock glacier case study (central Italian Alps). Permafrost and Periglacial Processes, 28, 224-236. Doi: 10.1002/ppp.1917.

Scotti, R., Brardinoni, F., Alberti, S., Frattini, P., Crosta, G.B., 2013. A regional inventory of rock glaciers and protalus ramparts in the central Italian Alps. Geomorphology, 186, 136-149. Doi: 10.1016/j.geomorph.2012.12.028.

Seppi, R., Carturan, L., Carton, A., Zanoner, T., Zumiani, M., Cazorzi, F., Bertone, A., Baroni, C., Salvatore, M.C., 2019. Decoupled kinematics of two

neighbouring permafrost creeping landforms in the Eastern Italian Alps. Earth Surf. Process. Landforms, 44, 2703-2719. Doi: 10.1002/esp.4698.

Staub, B., Lambiel, C., Delaloye, R., 2016. Rock glacier creep as a thermally-driven phenomenon: A decade of inter-annual observations from the Swiss Alps. XI International Conference on Permafrost, Postdam, Germany, 20-24 June 2016, 96-97.

Steger, C., Kotlarski, S., Jonas, T., Schaer, C., 2012. Alpine snow cover in a changing climate: a regional climate model perspective. Climate Dynamics, 41(3-4), 735-754.

Thies, H., Nickus, U., Tolotti, M., Tessadry, R., Krainer, K., 2013. Evidence of rock glacier melt impacts on water chemistry and diatoms in high mountain streams. Cold Regions Science and Technology, 96, 77-85.

Vivero, S., Bodin, X., Farías-Barahona, D., MacDonell, S., Schaffer, N., Robson, B.A., Lambiel, C., 2021. Combination of aerial, satellite, and UAV photogrammetry for quantifying rock glacier kinematics in the dry Andes of Chile (30°C) since 1950s. Remote Sensing, 2, 784015. Doi: 10.3389/frsen.2021.784015.

Vivero, S., Lambiel, C., 2021. Rock glacier deformation using Unmanned Aerial Vehicle (AUV) with RTK GNSS capability. EGU General Assembly 2021, online, 19-30 April 2021. EGU21-14844. https://doi.org/10.5194/egusphere-egu21-14844.

Vivero, S., Lambiel, C., 2019. Monitoring the crisis of a rock glacier with repeated UAV surveys. Geogr. Helv., 74, 59-69. https://doi.org/10.5194/gh-74-59-2019.

Wagner, T., Brodazc, A., Krainer, K., Winkler, G., 2020. Active rock glaciers as shallow groundwater reservoirs, Austrian Alps. Grundwasser, 25/3. https://doi.org/10.17738/ajes.2016.0006.

Wahrhaftig, C., Cox, A., 1959. Rock glaciers in the Alaska Range. Bulletin of the Geological Society of America, 70(4), 383-436.

Westoby, M.J., Brasington, J., Glasser, N.F., Hambrey, M.J., Reynolds, J.M., 2012. «Structure-from-Motion» photogrammetry: a low-cost, effective tool for geosciences applications. Geomorphology, 179, 300-314. Doi: 10.1016/j.geomorph.2012.08.021.

Wigmore, O., Mark, B., 2017. Monitoring tropical debris-covered glacier dynamics from high-resolution unmanned aerial vehicle photogrammetry, Cordillera Blanca, Peru. The Cryosphere, 11, 2463-2480. https://doi.org/10.5194/tc-11-2463-2017.

Williams, M.W., Knauf, M., Caine, N., Liu, F., Verplanck, P.L., 2006. Geochemistry and source waters of rock glacier outflow Colorado Front Range. Permafrost and Periglacial Processes, 17, 13-33.

Wirz, V., Gruber, S., Purves, R.S., Beutel, J., Gärtner-Roer, I., Gubler, S., Vieli, A., 2016b. Short-term velocity variations at three rock glaciers and their

relationship with meteorological conditions. Earth Surface Dynamics, 4, 103-123. Doi: 10.5194/esurf-4-103-2016.

Zahs, V., Hämmerle, M., Anders, K., Hecht, S., Sailer, R., Rutzinger, M.G., Williams. J., Höfle. B., 2019. Multi-temporal 3D point cloud-based quantification and analysis of geomorphological activity at an alpine rock glacier using airborne and terrestrial LiDAR. Permafrost and Periglac. Process., 30, 222-238. https://doi.org/10.1002/ppp.2004.